NASA/TM–20210014010

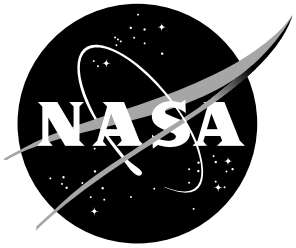

Investigation of High Incidence Angle Propeller Aerodynamics for Subscale eVTOL Aircraft

Benjamin M. Simmons and David B. Hatke
Langley Research Center, Hampton, Virginia

May 2021

NASA STI Program Report Series

Since its founding, NASA has been dedicated to the advancement of aeronautics and space science. The NASA scientific and technical information (STI) program plays a key part in helping NASA maintain this important role.

The NASA STI program operates under the auspices of the Agency Chief Information Officer. It collects, organizes, provides for archiving, and disseminates NASA's STI. The NASA STI program provides access to the NTRS Registered and its public interface, the NASA Technical Reports Server, thus providing one of the largest collections of aeronautical and space science STI in the world. Results are published in both non-NASA channels and by NASA in the NASA STI Report Series, which includes the following report types:

- TECHNICAL PUBLICATION. Reports of completed research or a major significant phase of research that present the results of NASA Programs and include extensive data or theoretical analysis. Includes compilations of significant scientific and technical data and information deemed to be of continuing reference value. NASA counterpart of peer-reviewed formal professional papers but has less stringent limitations on manuscript length and extent of graphic presentations.
- TECHNICAL MEMORANDUM. Scientific and technical findings that are preliminary or of specialized interest, e.g., quick release reports, working papers, and bibliographies that contain minimal annotation. Does not contain extensive analysis.
- CONTRACTOR REPORT. Scientific and technical findings by NASA-sponsored contractors and grantees.
- CONFERENCE PUBLICATION. Collected papers from scientific and technical conferences, symposia, seminars, or other meetings sponsored or co-sponsored by NASA.
- SPECIAL PUBLICATION. Scientific, technical, or historical information from NASA programs, projects, and missions, often concerned with subjects having substantial public interest.
- TECHNICAL TRANSLATION. English-language translations of foreign scientific and technical material pertinent to NASA's mission.

Specialized services also include organizing and publishing research results, distributing specialized research announcements and feeds, providing information desk and personal search support, and enabling data exchange services.

For more information about the NASA STI program, see the following:

- Access the NASA STI program home page at http://www.sti.nasa.gov
- Help desk contact information:

https://www.sti.nasa.gov/sti-contact-form/ and select the "General" help request type.

NASA/TM–20210014010

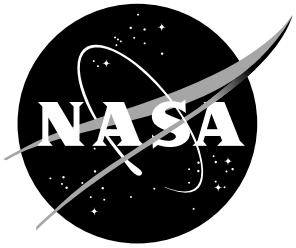

Investigation of High Incidence Angle Propeller Aerodynamics for Subscale eVTOL Aircraft

Benjamin M. Simmons and David B. Hatke
Langley Research Center, Hampton, Virginia

National Aeronautics and
Space Administration

Langley Research Center
Hampton, Virginia 23681-2199

May 2021

Available from:

NASA STI Program / Mail Stop 148
NASA Langley Research Center
Hampton, VA 23681-2199
Fax: 757-864-6500

Abstract

Propellers used for electric vertical takeoff and landing (eVTOL) aircraft propulsion systems experience a wide range of aerodynamic conditions, including significant incidence angles relative to oncoming airflow. Propellers in oblique flow exhibit deviations in thrust and torque oriented along their axis of rotation, as well as significant off-axis forces and moments. Although important for understanding eVTOL aircraft aerodynamics, sparse experimental data exist for propellers operating at incidence. This report describes an experimental wind tunnel study of isolated propeller aerodynamics across a wide range of flight conditions expected to be experienced by the LA-8 tandem tilt-wing, eVTOL aircraft. The experimental data obtained from the study are graphically presented and a discussion of observed aerodynamic phenomena is compared to theoretical expectations and past experimental work. The content of this report is intended to provide guidance to future propeller testing efforts and describe pertinent propeller aerodynamic behavior expected to be experienced by eVTOL vehicles.

Contents

List of Figures

List of Tables

Nomenclature

c	propeller chord at 75% blade length, ft
C_{T_x}, C_{T_y}, C_{T_z}	propeller force coefficients
C_{Q_x}, C_{Q_y}, C_{Q_z}	propeller moment coefficients
D	propeller diameter, ft
i_p	propeller incidence angle, rad or deg
J	advance ratio
J_x	normal advance ratio
J_z	tangential advance ratio
M_{tip}	propeller tip Mach number
n	propeller and motor rotational speed, revolutions/s
Q_x, Q_y, Q_z	propeller moments, ft-lbf
$\bar{q}$	freestream dynamic pressure, lbf/ft^2
Re	propeller blade Reynolds number
T_x, T_y, T_z	propeller forces, lbf
V_p	propeller blade linear speed at 75% blade length, ft/s
V_∞	freestream velocity, ft/s
η_p	propulsive efficiency
μ	air dynamic viscosity, lbf-s/ft^2
ρ	air density, slug/ft^3

Acronyms

CCW	counterclockwise
COTS	commercial off-the-shelf
CW	clockwise
DEP	distributed electric propulsion
DFT	discrete Fourier transform
ESC	electronic speed control
eVTOL	electric vertical takeoff and landing
LA-8	Langley Aerodrome No. 8
PWM	pulse width modulation
RPM	revolutions per minute
UAM	Urban Air Mobility
VRS	vortex ring state
VTOL	vertical takeoff and landing

1 Introduction

Urban Air Mobility (UAM) is currently drawing significant interest in the aerospace industry as a future transportation method being enabled by recent advances in electric vertical takeoff and landing (eVTOL) vehicle technology. In addition to vertical takeoff and landing (VTOL) capabilities, many eVTOL aircraft designs strive for efficient cruise flight, which requires a vehicle configuration that is a hybrid between fixed-wing and rotary-wing aircraft. NASA has initiated multiple efforts to develop conceptual and tangible eVTOL vehicles to better understand their flight characteristics and develop technology enabling mainstream integration of this new type of aircraft [1–4]. A common design attribute of eVTOL vehicles is distributed electric propulsion (DEP) with multiple propellers spread across the airframe. Since eVTOL vehicles experience a wide variety of flight conditions spanning hover, transition, and forward flight, their propellers experience aerodynamic conditions that significantly differ from conventional propeller operation. Propeller aerodynamics are conventionally defined in an axial airflow condition where data tables or a functional representation of axial thrust and torque coefficients are sufficient to model the propeller aerodynamics. However, at high incidence angles, off-axis propulsive forces and moments become significant, and axial thrust and torque deviates from its nominal axial airflow value.

The motivation of this work is to investigate and characterize the propeller aerodynamics for the Langley Aerodrome No. 8 (LA-8) aircraft, ultimately to develop a high-fidelity simulation of the aircraft. The LA-8 aircraft, pictured in Figure 1, is a subscale, tandem tilt-wing, DEP, VTOL configuration consisting of four propellers mounted to each wing [4]. The aircraft design leads to significant aerodynamic contributions from the airframe, propulsors, and airframe-propulsion interactions. The LA-8 is designed to be used as both a wind tunnel and flight testbed for advancing eVTOL technology. This work describes the wind tunnel testing effort used to characterize the isolated propulsion unit (including the propeller, electric motor, and electronic speed control), and is complimented by other NASA research pertaining to the LA-8 aircraft [4–12]. The data presented in this report have been used to facilitate development of a high-fidelity LA-8 propulsion system model [10], which aided development of an aerodynamic model for the LA-8 aircraft [11]. The isolated propeller data have also been used to inform LA-8 computational studies [12], and select data points have been validated in independent wind tunnel testing [13]. While the information in this report is presented in the context of the LA-8 vehicle, the objective is to generically characterize high incidence angle propeller aerodynamics and provide the reader physical understanding of the dominant propeller aerodynamic phenomena present for eVTOL vehicles.

This report is organized as follows: Section 2 presents pertinent background on propeller aerodynamics theory and previous research for propellers operating at high incidence angles. Section 3 describes the experimental design and setup for wind tunnel testing. Section 4 presents experimental results with accompanying discussion highlighting important data characteristics. Overall conclusions are summarized in Section 5. Figures displaying the experimental data are shown in Appendix A to maintain brevity in the report body.

2 Background

This section provides a theoretical background on axial propeller aerodynamics and propeller aerodynamics at incidence. Past experimental work characterizing propellers operating at high incidence angles is also summarized. Understanding of this background information aids interpretation of the results presented in Section 4.

(a) LA-8 front view (b) LA-8 rear view

Figure 1. LA-8 mounted in the NASA Langley 12-Foot Low-Speed Tunnel.

2.1 Axial Propeller Aerodynamics

Propeller aerodynamics are well-defined and well-researched for nominal operating conditions in axial flow where aerodynamic predictions can be made analytically and/or experimentally. Theoretical techniques include momentum theory, blade element methods, and vortex theories [14]. Experimental techniques typically consist of developing data tables or functional representations from wind tunnel data. For propellers in airflow normal to the propeller disk, the propeller only produces a net thrust force and a net aerodynamic torque acting along the axis of rotation [15]. The individual propeller blades can be thought of as rotating wings which each produce a lift force perpendicular to the relative flow direction and a drag force parallel to the relative flow direction [16]. The summed lift forces produced by the propeller blades is the propeller thrust T_x. The summed drag forces results in a net moment about the propeller shaft opposite to the direction of rotation, which is the propeller aerodynamic torque Q_x.

Propeller data are generally presented as a representation of thrust coefficient C_{T_x} and torque coefficient C_{Q_x} (or equivalently by power coefficient $C_P = 2\pi C_{Q_x}$ where $P = 2\pi n Q_x$). The thrust and torque coefficients are defined as

$$C_{T_x} = \frac{T_x}{\rho n^2 D^4} \tag{1}$$

$$C_{Q_x} = \frac{Q_x}{\rho n^2 D^5} \tag{2}$$

where n is the propeller rotational speed in revolutions per second, ρ is the air density, and D is the propeller diameter. The thrust and torque coefficients can be shown through dimensional analysis to be a function of advance ratio J, propeller blade Reynolds number Re, and propeller tip Mach number M_{tip} for a given propeller design [15, 17]. Because propeller similitude relations to scale propeller aerodynamics are limited [18], due to differences in boundary layer characteristics [19], propellers must be tested at full-scale to properly capture the advance ratio, Reynolds number, and Mach number effects.

Advance ratio J, which relates to the linear distance traveled by the propeller in one revolution, is defined as

$$J = \frac{V_\infty}{nD} \tag{3}$$

where V_∞ is the freestream velocity and other variables follow their earlier definition. Advance ratio generally has the largest effect on propeller aerodynamics, and thus, thrust and torque coefficient representations are commonly expressed as only a function of advance ratio. Representing propeller aerodynamics only as a function of advance ratio requires that airflow is parallel to the propeller axis of rotation as well as the assumptions that viscous and compressibility effects are negligible [15].

Reynolds number is a dimensionless quantity which corresponds to the ratio of inertial to viscous forces acting on a lifting body. For full-scale aircraft propellers, the propeller blade Reynolds number effects are minimal and can generally be neglected. For subscale propellers, the Reynolds number is lower, indicating that the viscous forces become more important. This effect manifests as a thicker boundary layer, which is more likely to result in flow separated from the propeller surface [19] and results in propeller performance degrading at lower Reynolds number [20, 21]. The equation used herein for the propeller blade Reynolds number Re follows the definition given in Reference [21],

$$Re = \frac{\rho V_p c}{\mu} \tag{4}$$

where ρ is the air density, c is the propeller chord at 75% blade length, μ is the dynamic viscosity, and $V_p = 0.75\pi nD$ is the propeller blade linear speed at 75% blade length.

Mach number is the ratio of flow speed to the speed of sound, which physically represents the ratio of inertial forces to forces related to compressibility of the fluid [19]. For subscale aircraft, the propeller tip Mach number generally remains low enough ($M_{tip} < 0.3$) such that compressibility effects can be ignored, which is the approach taken in this report.

Propulsive efficiency η_p is defined as the ratio of usable output power P_{out} to supplied power P_{in} [16]. Usable output power is defined as $P_{out} = T_x V_\infty$ and power input is defined as $P_{in} = 2\pi n Q_x$, therefore, propulsive efficiency can be expressed as:

$$\eta_p = \frac{T_x V_\infty}{2\pi n Q_x} \tag{5}$$

For a propeller in forward flight, propulsive efficiency can be expressed using thrust coefficient, torque coefficients, and advance ratio as:

$$\eta_p = \frac{\left(C_{T_x}\rho n^2 D^4\right) V_\infty}{2\pi n \left(C_{Q_x}\rho n^2 D^5\right)} = \frac{C_{T_x} J}{2\pi C_{Q_x}} \tag{6}$$

2.2 Theoretical Propeller Aerodynamics at Nonzero Incidence Angle

When the airflow relative to a propeller is not parallel to the axis of rotation, the propeller will produce auxiliary forces and moments other than the axial thrust and torque [15]. In this condition, periodic variation in propeller blade local angle of attack results in a non-uniform load distribution on the propeller disk. Thus, in a general case of arbitrary flow direction relative to the propeller disk, propeller forces and moments will also be dependent on the angle between the freestream velocity and propeller axis of rotation, in addition to advance ratio, propeller blade Reynolds number, tip Mach number, and the propeller design. This angle between the freestream airflow and propeller rotation axis is referred to in this work as the *propeller incidence angle*, i_p, shown in Figure 2. The value of i_p is zero when airflow is normal to the propeller disk, opposing the direction of axial thrust.

One additional auxiliary force and one additional auxiliary moment is predicted theoretically from the periodic lift and drag imbalance on the individual propeller blades [15, 16]. To explain these phenomena, it is useful to consider a common example of a front mounted propeller on an airplane

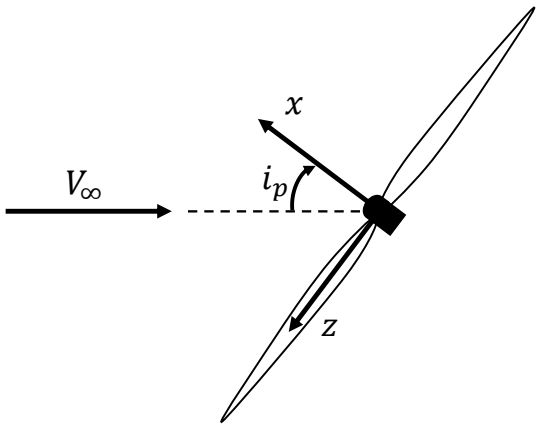

Figure 2. Propeller incidence angle definition and coordinate system.

in level, forward flight at positive angle of attack, where it is assumed that the propeller axis of rotation coincides with the x body-axis of the airplane. The propeller blades moving downward will produce more lift than the propeller blades moving upward because the downward moving blade is experiencing a higher angle of attack and relative airspeed. Consequently, the net center of thrust force is offset from the propeller axis of rotation, favoring the side of downward blade movement. When the net thrust force is transferred to the center of the propeller, a net yawing moment is observed acting to rotate the downward moving propeller blades into the oncoming airflow. This effect is often referred to as the p-factor. The individual propeller blade drag forces are also larger on the side of downward movement, again due to the greater relative angle of attack and airspeed, resulting in a net normal force directed upward for the current example. Thus, a propeller on an airplane at positive angle of attack will produce a normal force and a yawing moment in addition to the conventional axial thrust and torque. Following similar reasoning, the example propeller in sideslip will instead produce pitching moment and side force as the auxiliary force and moment.

An analytical treatment of airplane propeller aerodynamics at low angle of attack presented in Reference [16] agrees with the qualitative conclusions obtained from the preceding example. For a propeller operating at a small nonzero angle of attack and zero sideslip, the normal force and yawing moment are shown to be linearly proportional to the propeller incidence angle; pitching moment and side force coefficients are theoretically zero. It is also shown that for low incidence angle conditions, small perturbations in incidence angle have no effect on axial thrust and torque. Aerodynamic trends observed in experimental testing may differ from analytical predictions, as will be considered in Section 2.3 and Section 4.

The propeller side force T_y, normal force T_z, pitching moment Q_y, and yawing moment Q_z can be non-dimensionalized in a manner similar to the thrust T_x and torque Q_x [16]. The propeller normal force coefficient C_{T_z}, side force coefficient C_{T_y}, pitching moment coefficient C_{Q_y}, and yawing moment coefficients C_{Q_z}, are defined as:

$$C_{T_y} = \frac{T_y}{\rho n^2 D^4},\ C_{T_z} = \frac{T_z}{\rho n^2 D^4},\ C_{Q_y} = \frac{Q_y}{\rho n^2 D^5},\ C_{Q_z} = \frac{Q_z}{\rho n^2 D^5} \tag{7}$$

The propeller force and moment sign convention used in this work follows the right-handed propeller coordinate system shown in Figure 2, where the y-axis is pointed into the page.

2.3 Previous Experimental Research

Many previous studies have employed methods for theoretical and computational prediction of propeller aerodynamics at incidence [16, 22–29]; however, experimental techniques provide the most accuracy in revealing the highly complex and nonlinear behavior of propeller aerodynamics at incidence. Interest in vertical/short takeoff and landing (V/STOL) vehicles in the 1950's initiated several experiments studying propellers operating at incidence. Reference [30] tested a four bladed 1/3 full-scale propeller from 0° to 180° of incidence while also varying flow speed, propeller rotational speed, and propeller blade angle. Reference [31] conducted a similar study for three different full-scale 3-bladed propellers, varying flow speed, propeller rotational speed, blade angle, and propeller incidence angle between 0° and 85° degrees. The three different propeller variants, including different blade shape and a flapping propeller, were tested and exhibited similar force and moment deviations with incidence angle and the component of advance ratio normal to the propeller disk. A significant finding was that the axial thrust and torque coefficients were nearly constant and off-axis force and moment coefficients showed a roughly linear increase over a significant range of incidence angles when plotted against the normal component of advance ratio at a constant blade pitch angle. The angle of incidence where these trends were no longer followed occurred at lower incidence as the normal advance ratio increased. Reference [32] studied the high incidence angle aerodynamics of isolated propellers as well as propeller-wing interactions up to 90° of incidence, noting aerodynamic differences due to the presence of the wing.

References [30, 31] made use of an alternative advance ratio J_x describing the flow normal to the propeller disk,

$$J_x = \frac{V_\infty \cos i_p}{nD} \tag{8}$$

which was found to be more appropriate for describing propellers at incidence. Rotorcraft utilize a similar representation of advance ratio components [19, 33], from which a complementary definition of tangential advance ratio J_z can also be postulated:

$$J_z = \frac{V_\infty \sin i_p}{nD} \tag{9}$$

The normal and tangential representation of advance ratio was used in a previous propeller modeling effort that developed lookup tables for propulsive forces and moments for a quadrotor vehicle [34]. Propeller aerodynamic effects from advance ratio and incidence angle were also found to be best characterized by J_x and J_z for developing polynomial aerodynamic models for propellers at incidence [10].

The increased interest in efficient jet propulsion subsequent to References [30–32] resulted in propeller aerodynamics research becoming dormant for several decades, until recently when increased interest in electrically-powered unmanned aerial vehicles, distributed electric propulsion, and eVTOL designs arose in the aerospace community. Reference [35], performed wind tunnel testing of a 9-inch diameter, 5-inch pitch propeller at incidence angles ranging from 0° to 180° in 30-degree increments and flow speeds up to 29.5 ft/s. The off-axis side and normal forces at high incidence angles were found to be small compared to the axial thrust force generated by the propeller. Normal force magnitude was found to be less than axial thrust but still significant at nonzero incidence angles. Side force was found to be negligible for all incidence angles. The off-axis pitching and yawing moments were found to be comparable in magnitude to the aerodynamic torque along the axis of rotation at high incidence angles. Notably, this pitching moment result is not predicted by the propeller theory described in Reference [16] showing the limitations of the analytical treatment of propellers at incidence. The significant pitching moment at high incidence

angles can be attributed to non-uniform airflow through the front and rear portions of the propeller relative to the airflow, which leads to a tendency for the propeller to pitch upward at near 90° incidence angles [35]. This work also presented frequency domain analyses which showed a large peak in the plot of the measured forces and moments frequency spectrum in accordance with the measured rotational speed of the propeller suggesting an alternative technique to measure propeller rotational speed.

Reference [36] followed this work by testing the same 9-inch diameter, 5-inch pitch propeller and performing additional testing on multiple 3D printed propeller blades with different pitch angles at incidence angles ranging from 0° to 90° and flow speeds up to 32.8 ft/s. The measured propeller force and moment coefficients showed reasonable agreement between the testing efforts and trends between the propellers. Reference [37] also performed similar experiments for several subscale propellers at incidence angles ranging from 0° to 180° in 15° increments and flow speeds up to 49.2 ft/s.

Reynolds number effects associated with subscale propellers are also relevant to consider for subscale vehicles [20, 21, 38, 39]. Operation at low propeller blade Reynolds number (approximately 100,000 or lower) degrades propeller performance due to an increasing dominance of viscous effect. This results in decreased propeller blade lift production and an increase in propeller blade drag, which lowers efficiency and decreases thrust coefficient for otherwise identical conditions. Consequently, it is important to consider propeller blade Reynolds number as an additional factor to describe subscale propeller aerodynamics.

3 Wind Tunnel Experimentation

The isolated propeller wind tunnel testing for this study was performed in the NASA Langley Research Center 12-Foot Low-Speed Tunnel.[1] The facility is an atmospheric pressure tunnel with a 12-foot width and height octagonal cross-section and 15-foot test section length. Dynamic pressures are obtainable up to $\bar{q} = 7$ psf, which corresponds to a flow velocity of approximately 77 ft/s at standard sea level conditions. The air is pulled through the tunnel by a 6-blade, 15.8-ft diameter fan. The test section turbulence level is approximately 0.6% for the longitudinal center-line-flow. A schematic of the wind tunnel is shown in Figure 3. The remainder of this section describes the LA-8 propellers, experiment setup, testing methodology, and data collection procedures. Additional isolated propeller specific testing considerations are also highlighted.

3.1 LA-8 Propellers

The propellers tested in this study were 16-inch diameter, 8-inch pitch, fixed-pitch, folding three-bladed clockwise (CW) and counterclockwise (CCW) rotating propellers used on the LA-8 aircraft. The CW rotating propellers, as viewed from behind the aircraft, are available commercial off-the-shelf (COTS). Since the manufacturer only produced propellers for CW rotation and folding propellers of CW and CCW rotation of the desired size were not available from a suitable propeller manufacturer, a CCW propeller was custom developed to mirror the CW propeller geometry and performance. While the custom propellers were intended to exactly mirror the COTS propellers, slight differences in the propeller characteristics were noted through physical examination. The CCW custom propeller blades had a slightly smaller chord, span, and mass compared to the CW COTS propeller blades. Also, the shape and thickness of the CCW custom propellers was slightly

[1] Information available online at https://researchdirectorate.larc.nasa.gov/12-foot-low-speed-tunnel-12-ft-lst/ [accessed March 2021]

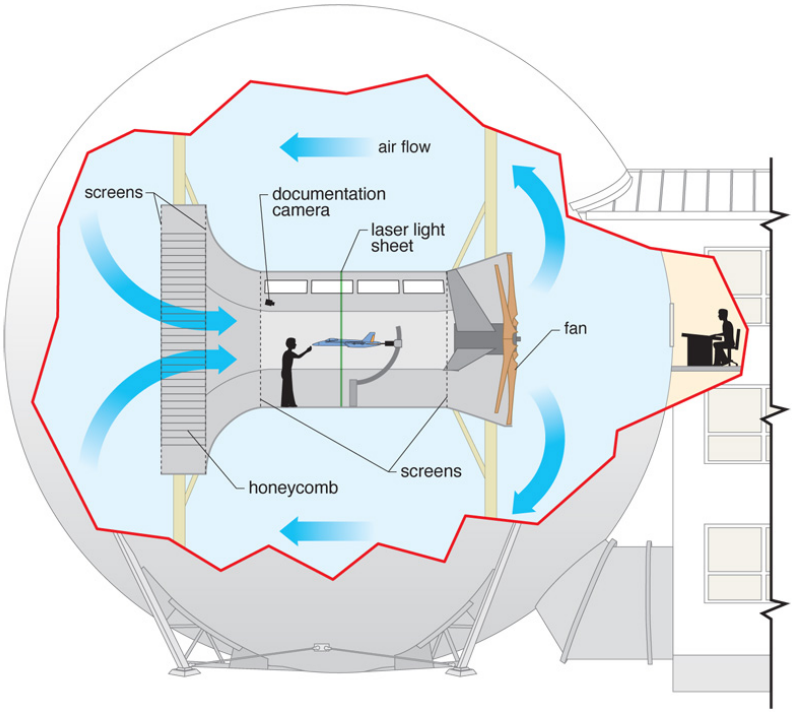

Figure 3. Schematic of the NASA Langley Research Center 12-Foot Low-Speed Tunnel.

different, particularly around the propeller tip, and the surface finish of the CCW custom propellers was noted to have a rougher texture compared to the CW COTS propeller. Additionally, the differences in custom propeller characteristics were found to be inconsistent throughout the production run so custom propellers with nearly identical mass were selected for testing to reduce vibrations. A photograph comparing the CW COTS and CCW custom propeller blade planforms is shown in Figure 4. Visually, the mirroring of the propellers appears to be very similar. Figure 5 shows additional photographs of the propeller blade shape, and the assembled three-bladed propeller.

Figure 4. Comparison of the custom CCW rotating (upper) and COTS CW rotating (lower) propeller blade planforms, as viewed from the bottom.

3.2 Experiment Setup

The six force and moment components were acquired during wind tunnel testing using a strain gauge balance with measurement range and accuracy given in Table 1 and Table 2, respectively. The balance was attached to the sting to allow the balance and propulsion system to rotate from 0° to 180° relative to the oncoming airflow without having to modify the balance or propulsion system

(a) Propeller blade (top and side view)

(b) Assembled three bladed propeller (front view)

Figure 5. Experimental CCW rotating propeller.

orientation. The balance was protected from the aerodynamic forces and thermal effects from the airflow with a fairing, as depicted in Figure 6. The balance fairing was determined to be beneficial in previous isolated propeller testing to obtain reliable results [34]. Gaps between the fairing and motor were covered with aluminum tape to further inhibit any air from moving over the sensitive strain gauges of the balance. The balance fairing was mounted to the sting such that it imparted no forces into the recorded data.

Table 1. Measurement range of the strain gauge balance used for wind tunnel testing

	x	y	z	Units
Force	±50	±60	±100	lbf
Moment	±176	±480	±540	in-lbf

Table 2. Measurement accuracy of the strain gauge balance used for wind tunnel testing (95% confidence interval expressed as a percentage of maximum loading)

	x	y	z
Force	0.05%	0.07%	0.04%
Moment	0.11%	0.04%	0.03%

The propellers were powered by a 450 KV electric motor and 100-amp electronic speed control (ESC). The ESC was powered with 29 volts at 32 amps using wiring running along the model sting. The ESC was provided input pulse width modulation (PWM) signals by a microcontroller to set the desired motor rotational speed, which is equivalent to the propeller rotational speed. The measured motor rotational speed in revolutions per minute (RPM) from the ESC was extracted using a Teensy35 microcontroller. Both input PWM signal and measured RPM were linked to the control room via an Arduino Mega and recorded by the data acquisition system. In previous LA-8 wind tunnel entries with the same motor, it was observed that the motor RPM for the same input commands and flow conditions changed over time due to thermal effects. It was determined that the motor temperature reached an approximate steady state after running for 10 minutes at a PWM command of 1550 μs. Therefore, before each run, the motors were warmed up by running

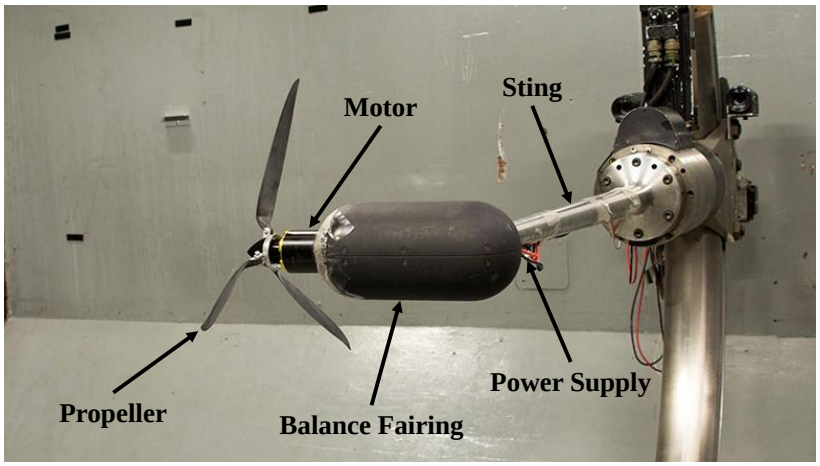

Figure 6. LA-8 propeller installation on the wind tunnel sting.

them at a PWM command of 1550 μs for 10 minutes to reduce transient thermal effects while collecting data. This step is important because of the open-loop nature of the control system used and proved to be useful in previous testing.

3.3 Testing Methodology and Experimental Design

The propeller wind tunnel experiment was designed to cover a majority of the operational envelope of the LA-8 aircraft and match the propeller flight conditions experienced in a previous LA-8 powered-airframe wind tunnel entry used to develop an aerodynamic model of the aircraft [7, 11]. Static wind-tunnel testing for each propeller variant was conducted in a one-factor-at-a-time manner directly commanding dynamic pressure $\bar{q}$, motor PWM command, and incidence angle i_p. Testing was performed at dynamic pressure settings ranging from 0 to 6 psf, which corresponds to a freestream airspeed from 0 to 71 ft/s at standard sea level conditions. Testing at the tunnel limit of 7 psf was avoided due to tunnel heating issues and because the LA-8 powered-airframe wind tunnel testing was only performed up to 5 psf [7]. The tunnel dynamic pressure settings were chosen to vary the flow velocity in a roughly linear manner because airspeed has a larger effect on propeller aerodynamics due to the strong dependence on advance ratio (cf. Equation (3)). Freestream velocity is related to dynamic pressure by $V_\infty = \sqrt{2\bar{q}/\rho}$, therefore, finer increments of dynamic pressure were selected at lower dynamic pressure test points.

Incidence angle was varied from 0° to 180° for dynamic pressures up to 1.5 psf to capture the thrust decrease and thrust fluctuations seen when approaching a vortex ring state (VRS) [40]. The incidence angle increments between points was chosen to be 10° for $0° \leq i_p \leq 60°$, 5° for $65° \leq i_p \leq 115°$, and 10° for $120° \leq i_p \leq 180°$. Finer increments were tested near 90° of incidence because of the expected and observed higher sensitivity of changes in forces and moments when the flow is nearly parallel to the propeller disk. Incidence angle was varied between 0° and 90° at a dynamic pressure setting of 2.5 psf in 10° increments for $0° \leq i_p \leq 60°$ and 5° increments for $65° \leq i_p \leq 90°$. Incidence angle was varied between 0° and 60° in 5° increments at dynamic pressure settings of 3.5 psf and above. The motor PWM command inputs were varied evenly at five different settings between 1350 μs to 1600 μs for all dynamic pressure settings and incidence angles, which translates to a propeller rotational speed range of approximately 1500 RPM to 6000 RPM. The test matrix is summarized in Table 3 and is shown graphically in Figure 7.

Table 3. Propeller wind tunnel test matrix

$\bar{q}$ [lbf/ft^2]	V_∞ [ft/s]	PWM Command [μs]	i_p [deg]
0	0.0	[1350, 1413, 1475, 1538, 1600]	[0:10:60, 65:5:115, 120:10:180]
0.25	14.5	[1350, 1413, 1475, 1538, 1600]	[0:10:60, 65:5:115, 120:10:180]
0.5	20.5	[1350, 1413, 1475, 1538, 1600]	[0:10:60, 65:5:115, 120:10:180]
1	29.0	[1350, 1413, 1475, 1538, 1600]	[0:10:60, 65:5:115, 120:10:180]
1.5	35.5	[1350, 1413, 1475, 1538, 1600]	[0:10:60, 65:5:115, 120:10:180]
2.5	45.9	[1350, 1413, 1475, 1538, 1600]	[0:10:60, 65:5:90]
3.5	54.3	[1350, 1413, 1475, 1538, 1600]	[0:5:60]
4.5	61.5	[1350, 1413, 1475, 1538, 1600]	[0:5:60]
6	71.0	[1350, 1413, 1475, 1538, 1600]	[0:5:60]

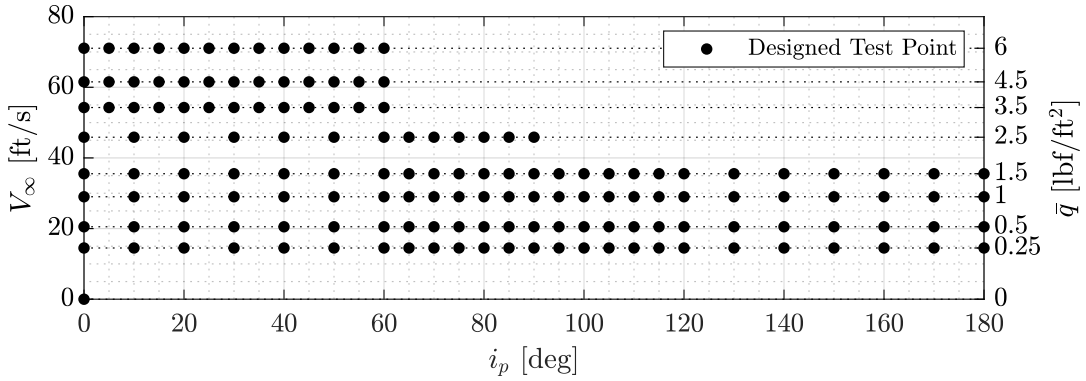

Figure 7. Graphical representation of the designed propeller wind tunnel test points for freestream velocity and incidence angle (all five motor PWM commands are tested at each point).

3.4 Test Execution and Data Collection

The propeller test conditions were established by commanding different values of tunnel dynamic pressure, motor PWM signal, and incidence angle. Each individual wind tunnel run was executed by sweeping incidence angle while holding a constant dynamic pressure setting and motor PWM command throughout the run. This procedure is reflected in the multi-exposure image of a test run depicted in Figure 8a. The propeller coordinate system and incidence angle measurement is depicted in Figure 8b.

Five seconds of contiguous data were recorded for each test point to allow sufficient averaging of dynamic data, particularly nearing thrust fluctuations associated with a VRS. A sample rate of 2,500 Hz was selected to allow frequency domain analysis of the data with a maximum frequency well above the propeller rotation rate (the Nyquist frequency is 1,250 Hz or 75,000 RPM). A sixth-order Butterworth anti-alias filter with a cutoff frequency of 1,000 Hz was applied before sampling the data. While the test point conditions were specified using dynamic pressure and motor PWM command, these settings were used to indirectly sweep variables more pertinent to propeller aerodynamics: freestream airspeed V_∞ and propeller rotational speed n. These latter quantities were then further reduced to calculate propeller advance ratio(s) (Equations (3), (8), and (9)) and propeller blade Reynolds number (Equation (4)). Changes in dynamic pressure change the flow velocity, which drives changes in propeller advance ratio. Changes in motor PWM command change the propeller rotational speed, which has the primary effect of changing the

(a) Multi-exposure image of a wind tunnel run (b) Propeller test coordinate system

Figure 8. LA-8 propeller mounted in the NASA Langley 12-Foot Low-Speed Tunnel.

propeller blade Reynolds number, but also contributes to changes in the propeller advance ratio. A plot of the tested values of normal advance ratio J_x and tangential advance ratio J_z for the CW rotating propeller is shown in Figure 9. A plot showing the range of propeller rotational speed and propeller blade Reynolds number covered by the testing is shown in Figure 10. The figures show data corresponding to the CW rotating propeller, but the conditions experienced by the CCW propeller are similar.

In addition to the nominal static test matrix, several repeat and validation-specific runs were made to ensure data quality and allow testing of the model predictive capability. Validation runs were taken with different motor PWM commands and dynamic pressure settings within the ranges tested. Furthermore, several continuous data collection runs containing variable amplitude motor step inputs were made at multiple dynamic pressure settings with $0° \leq i_p \leq 60°$ to aid characterization of the motor dynamics.

3.5 Additional Isolated Propeller Testing Considerations

A phenomenon that has been noted in several past tests of propellers in the NASA Langley 12-Foot Low-Speed Tunnel is balance zero shifting for long runs. There are multiple suspected causes including airflow over the balance, temperature changes, violent vibrations, and electrical interference, which are far less prevalent in conventional aircraft model wind tunnel tests. The balance fairing discussed in Section 3.2 appeared to mitigate a large amount of the zero shifting phenomenon, however, shortening the run time and taking a new zero before each run appeared to further reduce data corruption from zero shifting. Even with these precautions, the test personnel needed to remain vigilant for sporadic runs corrupted with large amounts of measurement errors which were required to be re-tested.

One notable approach found to be critical to ensuring quality data collection was a *modeling-while-testing* approach, which comprised of fitting polynomial models to the data during the test using similar techniques to those described in Reference [10]. After sufficient data were collected to enable preliminary model development, modeling residuals were analyzed and outlying residuals were flagged for inspection. Outlying residuals were generally found to occur in clusters linked to a specific wind tunnel run. When this was the case, the wind tunnel run was re-tested. Most of the time, the new data would then agree more with the expectations from the model, which suggested to include the new run for modeling and to discard the suspect run. This procedure was imperative

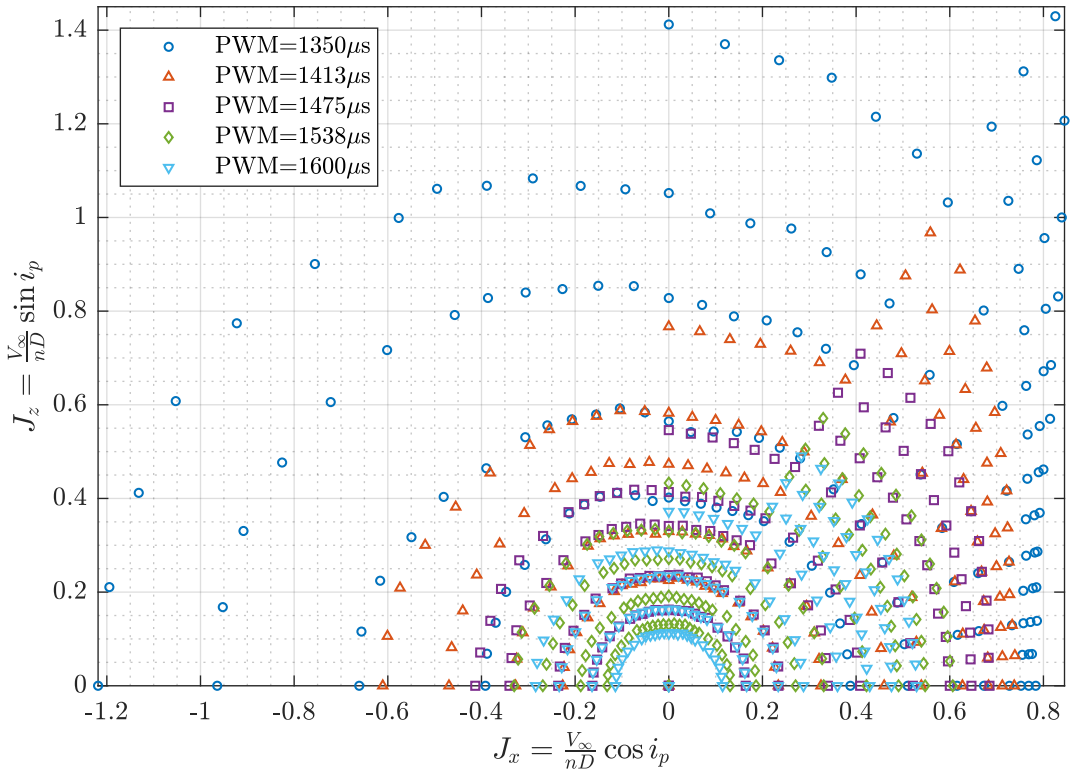

Figure 9. Tested range of normal and tangential advance ratio.

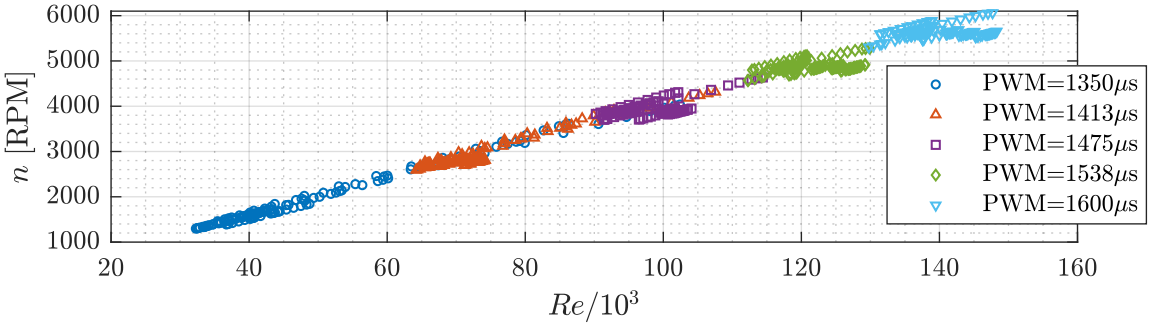

Figure 10. Tested range of propeller rotational speed and propeller blade Reynolds number.

to ensure all data used for subsequent model development was high quality.

The RPM measurement provided by the motor-ESC setup was validated by analyzing the frequency spectrum of the vibrations experienced by the balance. A large spike in the magnitude of the frequency response corresponding to the measured RPM was noted at all test conditions and the accuracy of the RPM measurement was well within the resolution of the discrete Fourier transform (DFT) technique for the given sampling time and sampling rate. Additional analysis was performed using a Fourier transform technique which leverages time-domain cubic interpolation and the chirp z-transform to produce a high accurate spectrum with arbitrary frequency resolution [41, 42]. The calculations were carried out using codes available in the System IDentification Programs for

AirCraft (SIDPAC) software toolbox.[2] Using the latter high-accuracy Fourier transform technique, most residuals between measured RPM and the peak of the frequency spectrum spike were within approximately ±5 RPM or approximately 0.2% difference, confirming the accuracy and precision of the RPM measurement from the ESC. In theory, the frequency domain analysis could be used as a replacement to an RPM measurement, however, structural responses in the tunnel make this approach difficult to use exclusively because of interference observed at certain frequencies. A sample frequency domain analysis depicting this strategy will be shown in Section 4.

4 Results and Discussion

Figures showing the collected propeller wind tunnel test data for the CW and CCW rotating propellers are given in Appendix A. The figures are described in this section and important observations are highlighted. Recall from Section 2, the aerodynamics for a given propeller design in axial airflow are primarily dependent on advance ratio J, propeller blade Reynolds number Re, and tip Mach number M_{tip}. Incidence angle i_p becomes another factor for describing propeller aerodynamics at nonzero incidence. For the experimental propellers in this work, advance ratio and angle of incidence effects were expected to be the main contributing factors to the propeller aerodynamics. The propellers also operate at low propeller blade Reynolds number (approximately 40,000 to 140,000), which was expected to be a smaller, but still significant factor. Since the testing was performed at subsonic, nearly incompressible propeller tip conditions, tip Mach number effects were not studied. Advance ratio, incidence angle, and propeller blade Reynolds number effects are examined in the subsequent figures.

It is worth noting a few test-specific data presentation subtleties. The off-axis force and moments measurements (T_y, T_z, Q_y, Q_z) and their corresponding dimensionless values were shifted such that they were zero in axial flow ($i_p = 0°$) for each run (recall incidence angle was swept from 0° up to a maximum value specified for each run). In theory, at zero incidence, propellers should only produce an axial thrust force and aerodynamic torque about the axis of rotation. Small offsets were noted in the data, particularly for the lower magnitude non-axial forces and moments, which could be attributed to sting interactions, slight misalignment of measurement hardware, flow angularity, or other small measurement errors. For equivalent test conditions, the off-axis forces and moments values at zero incidence were inconsistent; the curve shapes against incidence angle for each run appeared to be preserved, but a small constant offset was observed in repeat runs at the same test conditions. Also of note is that many plot traces are separated by commanded motor PWM signal. A more aerodynamically representative choice would be to separate by propeller rotational speed n; however, data were not collected with propeller speed feedback. Since the PWM command was fixed for incidence angle sweeps, the propeller speed varied slightly as a function of incidence angle. This is because propeller speed is also a function of freestream conditions in addition to PWM command. However, PWM command on a per test condition basis is still a good metric to characterize changes in propeller rotational speed or changes in propeller blade Reynolds number, and can be interpreted as such.

Figures 11-12 show the measured propeller rotational speed n variation with freestream airspeed V_∞ and the component of freestream airspeed normal to the propeller disk $V_\infty \cos i_p$ for the CW and CCW rotating propellers. The plots are separated by incidence angles ranging from 0° to 90° and 90° to 180°. The figures show different propeller speed behavior for $0° \leq i_p \leq 90°$ and $90° \leq i_p \leq 180°$, resulting from the oncoming airflow either resisting or favoring propeller motion. Between 0° and 90° of incidence, the output rotational speed appeared to have a strong dependence

[2]Information available online at https://software.nasa.gov/software/LAR-16100-1 [accessed March 2021]

on motor PWM command, freestream velocity V_∞, and incidence angle i_p. The normal component of freestream velocity relative to the propeller $V_\infty \cos i_p$ appears to well characterize the V_∞ and i_p dependent variation in a single variable. Between 90° and 180° of incidence, freestream velocity and incidence angle appeared to have a much smaller effect on output propeller rotational speed; propeller speed appears to be mainly dependent on only the motor PWM command. The overall propeller speed values for a particular PWM command appears to be slightly higher for the CCW rotating propeller compared to the CW rotating propeller.

Figure 13 presents the acquired data at the static condition ($\bar{q} = 0$ psf). The plots show motor PWM command, propeller blade Reynolds number Re, thrust T_x, torque Q_x, thrust coefficient C_{T_x}, and torque coefficient C_{Q_x} plotted against measured propeller rotational speed n. Note that the axial torque coefficient C_{Q_x} and axial torque Q_x are shown as absolute quantities to allow better comparison between CW and CCW propeller performance—the axial torque for the CW rotating propeller is always negative. The thrust and torque increased with increasing propeller rotational speed, with a steeper increase at higher propeller speed. The thrust and torque coefficients show a slight overall increase with increasing propeller rotational speed, suggesting the presence of Reynolds number effects. If Reynolds number effects were not present, the thrust and torque coefficient traces would, in theory, remain a constant value against RPM. The thrust and torque for the CW rotating propeller are greater than the CCW rotating propeller, with a larger difference at higher propeller speeds.

Figures 14-21 show the dimensional propeller forces and moments as a function of propeller incidence angle i_p. Each plot shows the data for the CW and CCW rotating propellers at each of the five tested motor PWM command settings in μs, where each legend entry corresponds to a specific wind tunnel run composed of an incidence angle sweep. The propeller speed n and freestream airspeed V_∞ are also included to illustrate the similarity of test conditions. Plots are separated by the dynamic pressure $\bar{q}$ (or equivalently standard sea level freestream velocity V_{SSL}) test condition. Figures 22-29 show equivalent plots to Figures 14-21 only instead showing the propeller force and moment coefficients. Note that the absolute value of axial torque Q_x and torque coefficient C_{Q_x} is again shown to facilitate improved visual comparison of CW and CCW rotating propellers. Notable observations from these figures are summarized as follows:

- The axial thrust T_x plots at each dynamic pressure setting show that the thrust gradually increases as incidence angle increases before leveling off at about 60° of incidence. Beyond 60° of incidence the axial thrust variation becomes more nonlinear with incidence angle. Axial thrust is also observed to decrease overall at higher dynamic pressure settings at low incidence angles.

- The measured axial thrust T_x and axial torque Q_x of the CW rotating propeller is observed to be significantly larger than that of the CCW propeller for equivalent motor PWM commands, particularly at low freestream airspeed and higher motor PWM settings. This is compounded by noting that the RPM is always greater for the CCW rotating propeller for equivalent motor command. This difference can be attributed to the aforementioned geometric differences due to different manufacturing processes for each propeller (see Section 3.1). The individual propeller blades for the CW rotating propeller produce more lift and more drag compared to the CCW rotating propeller (see Section 2.1).

- The propeller side force T_y is negligible in theory and was observed in other similar studies to be insignificant [30, 31, 35]. However, the T_y traces as a function of incidence angle appear to have deterministic trends. Since the tested propellers were folding propellers, the propellers were able to flap through the incidence angle sweeps, similar to the passive flapping of heli-

copter rotors in forward flight. Thus, the observed side force may be attributed to cyclic blade flapping. Opposite contributions to side force from the CW and CCW propeller also provided evidence that there is a perceptible side force phenomena occurring in the data. Although, inexplicable changes in certain traces of T_y reflect the measurement limitations because of the low magnitude of the side force relative to the axial thrust. Side force contributions may be insignificant for many applications.

- Normal force T_z is observed to generally become increasingly negative for incidence angles between 0° and approximately 90° for both propeller orientations, as theory would suggest. At high freestream velocity, the normal force is invariant with propeller orientation and propeller rotational speed at low incidence angles ($i_p < 30°$). Since normal force is directed in the same direction for both propeller orientations, the effect of counter-rotating propellers is additive and will have a significant effect on vehicle dynamics.

- Propeller pitching moment Q_y initially increases positively at higher PWM settings for both the CW and CCW propellers as incidence angle is swept. This differs from theoretical predictions of no pitching moment produced at shallow incidence angles, but agrees with aforementioned experimental results from other studies. Pitching moment in some cases at a high PWM setting increases then shows a large decrease near 90° of incidence then increases again before tapering off at 180° degrees of incidence (cf. Figures 16-17). The peak pitching moment typically does not occur at $i_p = 90°$. Since the pitching moment is generally the same sign for both propeller orientations, the effect of counter-rotating propellers is additive and will have a significant effect on vehicle dynamics.

- Propeller yawing moment Q_z is observed to initially increase positively for the CCW rotating propeller and negatively for the CW rotating propellers from zero incidence, as theoretical predictions would suggest. The yawing moment magnitude for the CCW rotating propeller appears to generally be greater than CW rotating propeller at otherwise equivalent test points for $i_p \leq 90°$. The yawing moment magnitude is close to that of the axial torque at high incidence angles, particularly at high propeller rotational speeds and for the CCW propeller.

- All off-axis propeller forces and moments (T_y, T_z, Q_y, and Q_z) appear to have significant magnitude at incidence. While most of these components are generally significant for all propellers operating at incidence, some of these effects in this study can be partially attributed to blade flapping due to the folding propeller design, which places a component of the nominal blade lift and drag forces outside of the plane normal to the axis of rotation.

- Vortex ring state (VRS) like phenomena are observed in Figure 16-17 as decreases in axial thrust in descent, or high incidence (i_p near 180°), conditions. This also coincides directly with large thrust fluctuations visible in continuous data time histories and blade flapping fluctuations seen in video camera footage of the test points. The specific test points where VRS-like phenomena were noted for both propeller orientations were:

  - $\bar{q} = 1.0$ psf, $i_p = 160°$ to 180°, and PWM = 1538 μs ($n \approx 4950$ RPM)
  - $\bar{q} = 1.0$ psf, $i_p = 150°$ to 160°, and PWM = 1600 μs ($n \approx 5700$ RPM)
  - $\bar{q} = 1.5$ psf, $i_p = 160°$ to 180°, and PWM = 1600 μs ($n \approx 5700$ RPM)

  The advance ratio where this VRS-like phenomena occurs is between $0.23 \leq J \leq 0.28$ in descent. A sample plot of the frequency spectrum of a data point with VRS-like phenomena is shown in Figure 65, which is described later in this section.

- The larger magnitude axial thrust and torque (both mean value and dynamic fluctuations) drive the choice of the wind tunnel balance load limits and resolution. Consequently, lower magnitude off-axis force and moment measurements will have a lower signal-to-noise ratio relative to axial measurements, which should be considered when making observations from the collected data.

Figures 30-36 show the propeller force and moment coefficients plotted against advance ratio J for the CW rotating propeller. Each figure corresponds to a specific incidence angle. The plots also show dynamic pressure $\bar{q}$ and propeller blade Reynolds number Re. Additionally, the plots at $i_p = 0°$ show freestream velocity V_∞, propeller rotational speed n in RPM, axial thrust T_x, and axial torque Q_x (C_{T_y}, C_{T_z}, C_{Q_y}, and C_{T_z} are zero at $i_p = 0°$). The specific incidence angles shown are $i_p = [0°, 30°, 60°, 90°, 120°, 150°, 180°]$. The equivalent plots for the CCW rotating propeller are shown in Figures 37-43. Since incidence angle is held constant, and advance ratio is plotted on the horizontal axis, overall trends in otherwise-equivalent data points for different PWM settings can be interpreted as propeller blade Reynolds number Re effects. Key observations from these figures are summarized as follows:

- The axial thrust coefficient C_{T_x} has a strong dependence on advance ratio at each incidence angle condition. At the lower incidence angle conditions ($i_p \leq 60°$), the thrust coefficient decreases as advance ratio increases. At the higher incidence angle conditions ($i_p \geq 90°$), the thrust coefficient is first level or slightly decreases, then increases as advance ratio increases. At high incidence angles approaching a descent condition ($i_p \geq 150°$), a sharp valley is observed near $0.23 \leq J \leq 0.28$ reflecting an approach to VRS. Thrust coefficient degradation with Re is apparent at lower incidence angles ($i_p \leq 60°$) for the lower two PWM settings (1350 μs and 1413 μs) where Re is less than 100,000. For higher PWM settings where Re is greater than 100,000 and higher incidence angles ($i_p \geq 90°$), Reynolds number effects are not as evident in the data.

- The axial torque coefficient C_{Q_x} decreases in absolute magnitude as advance ratio increases for low incidence angles near $i_p = 0°$ and increases in absolute magnitude as advance ratio increases for high incidence angles. The transition between these two trends occurs near $i_p = 60°$, where the data trends are somewhat ill-defined. Re effects for C_{Q_x} can be seen in the data at lower PWM settings, particularly at lower incidence angle conditions.

- The normal force coefficient C_{T_z} is generally negative and increases relatively linearly in absolute magnitude as advance ratio increases for $i_p \leq 90°$. Re-based trends for C_{T_z} are observed in the plots where $i_p = 30°$, but are less apparent at other incidence angles.

- The side force coefficient C_{T_y} is generally observed to have a smaller magnitude compared to C_{T_x} and C_{T_z} in each plot. However, there still appears to be deterministic attributes in the data where trends for the CW and CCW rotating propellers are opposite, as would be expected. Rough Re-based trends are observed for C_{T_y} at lower nonzero incidence angles. For incidence angles $i_p \leq 90°$ there is an apparent sign change in C_{T_y} as advance ratio increases.

- The pitching moment coefficient C_{Q_y} is generally positive for $i_p \leq 120°$, except for several data points typically associated with lower PWM settings. Re-based trends are noted in the data for $i_p \leq 90°$.

- The yawing moment coefficient C_{Q_z} increases in absolute magnitude as advance ratio increases for $i_p \leq 90°$; C_{Q_z} for the CW rotating propeller is generally negative and C_{Q_z} for the CCW

rotating propeller is generally positive for $i_p \leq 90°$. The yawing moment for the CW and CCW rotating propellers appear to both become positive for high incidence angles approaching $i_p = 180°$, which is potentially caused by sting interaction (all nonzero off-axis force and moment coefficients at $i_p = 180°$ are also likely caused partially by sting interactions). Rough Re attributed trends in C_{Q_z} are observed for $i_p \leq 90°$.

Figures 44-52 show the dimensionless forces and moment coefficients for the CW rotating propeller against conventional advance ratio J (Equation (3)), normal advance ratio J_x (Equation (8)), and tangential advance ratio J_z (Equation (9)). The plots are broken up by range of incidence angle from 0° to 60°, 70° to 110°, and 120° to 180° where each legend entry corresponds to a specific incidence angle. Either J, J_x, or J_z is shown on the horizontal axis for each plot. Figure 53 shows the forces and moment coefficients for the CW rotating propeller against both J_x and J_z in a 3D plot. The plots only show data for the highest three PWM commands (1475 μs, 1538 μs, and 1600 μs) to display data at higher propeller blade Reynolds number such that Re effects are less prominent. Figures 54-63 show equivalent plots for the CCW rotating propeller. Plotting the data against J_x and J_z is highlighted because these variables were important to identifying propeller aerodynamic models in connected research [10]. The key takeaways from these figures are summarized as follows:

- Axial thrust coefficient C_{T_x} and torque coefficient C_{Q_x} variation are well characterized by J_x at low incidence angles, as can be seen in Figure 45 and Figure 55. Similar observations were made in previous research [31]. Both J_x and J_z are useful for describing C_{T_x} and C_{Q_x} variation at higher incidence angles.

- The normal force coefficient C_{T_z} variation is well described by J_z at low incidence angles, as can be seen in Figure 46 and Figure 56. The yawing moment coefficient C_{Q_z} is also reasonably well characterized by J_z at low incidence angles. Both J_x and J_z is useful for describing C_{T_z} and C_{Q_z} variation at higher incidence angles as well as side force coefficient C_{T_y} and pitching moment coefficient C_{Q_y} at all incidence angles.

- These figures (particularly the 3D plots shown in Figure 53 and Figure 63) show that all the propeller force and moment coefficients variations are well described using both J_x and J_z, absent of significant propeller blade Reynolds number effect. The relationship of force and moment coefficients to J_x and J_z is also highly nonlinear across J_x–J_z space, which also reflects that propeller aerodynamics are highly dependent on advance ratio J and incidence angle i_p. From Figure 53 and Figure 63, it can be seen that a response surface could be fit through the data points to develop an aerodynamic model describing the aerodynamics for the LA-8 vehicle across its large flight envelope. A similar approach, which also considered propeller blade Reynolds number effects, was taken to develop propeller aerodynamic models for the LA-8 aircraft [10].

Figure 64 shows the propeller propulsive efficiency η_p against advance ratio at zero incidence angle with different PWM command settings shown in the legend. The plots show that the propellers are generally less efficient at the lower two PWM settings (1350 μs and 1413 μs) as a result of lower propeller blade Reynolds number operation decreasing performance. The plots also show that the CW rotating propeller has a higher propulsive efficiency compared to the CCW rotating propeller. Both propellers have a peak efficiency at around $J = 0.55$.

Figure 65 shows the time histories and power spectrum for individual data points for the CW rotating propeller at a dynamic pressure of 1.5 psf and a PWM command of 1600 μs. One test point is at $i_p = 0°$ representing a forward flight or ascent condition. The other test point is at $i_p = 180°$

representing a descent condition where VRS-like characteristics were noted in testing. The time history plots for the two test points show the raw measured axial thrust T_x signal subtracted from its mean value $T_{x_{ave}}$, and the data signal smoothed using a global optimal Fourier smoother [41, 43] with a cutoff frequency of 15 Hz. The time history plot for the data point at $i_p = 0°$ shows a nearly constant smoothed signal with high frequency vibrations apparent in the raw measured signal with peaks at approximately ±2 lbf. The smoothed measurement time history for the data point at $i_p = 180°$ varies with the time with the non-attenuated low frequency content varying up to approximately 2 lbf. Higher amplitude low frequency content is also seen in the raw measured signal peaking at roughly ±12 lbf. The corresponding frequency domain plots show the power spectrum calculated using three methods: a high accuracy Fourier transform technique (FINT) [41, 42] (discussed above in Section 3.5), the discrete Fourier transform (DFT), and Welch's method.[3] The measured RPM provided by the ESC is also shown on the plot. The power spectrum for the data point at $i_p = 0°$ shows that the power of the vibrations is concentrated at higher frequencies. The largest peak occurs at the propeller rotation speed frequency, as was discussed previously in Section 3.5 and as was shown in Reference [35]. The power spectrum for the data point at $i_p = 180°$ shows overall greater power magnitude across the frequency range compared to the data point at $i_p = 0°$. The power for the $i_p = 180°$ data point is particularly high at low frequencies (less than 20 Hz) and between 200 Hz to 300 Hz. The amplitude of the low frequency vibrations present in the $i_p = 180°$ data point are up to two orders of magnitude higher than the amplitude of the low frequency vibrations present in the $i_p = 0°$ data point.

5 Conclusions

This report described a wind tunnel study performed to characterize propeller aerodynamics for subscale eVTOL vehicles. Specifically, an isolated propeller wind tunnel test was conducted over the expected flight envelope for the LA-8 aircraft using propellers from the aircraft. Both the clockwise and counterclockwise rotating propellers were tested to characterize their performance differences. Observations from this research effort are summarized as follows:

- Propeller aerodynamics have a strong, nonlinear dependence on incidence angle, resulting in significant off-axis force and moment components in addition to axial thrust and torque performance changes when operating at high incidence angles. While certain aerodynamic phenomena are predicted by theoretical analyses, experimental testing provides the most accuracy for characterizing the complex and nonlinear nature of propeller aerodynamics at incidence.

- The force and moment coefficients for the propellers investigated in this study appear to be mainly dependent on the advance ratio J, propeller blade Reynolds number Re, and propeller incidence angle i_p. The use of the normal component of advance ratio $J_x = J \cos i_p$ and the tangential component of advance ratio $J_z = J \sin i_p$ suggest an alternate formulation to advance ratio J and incidence angle i_p that could be used for aerodynamic database development.

- Propellers operating at low Reynolds number (approximately less than 100,000) will experience performance degradation, including differences in the propeller force and moment coefficient values at incidence.

[3] Welch's method calculations were performed using the `pwelch.m` function available in the MATLAB® Signal Processing Toolbox.

- Since eVTOL vehicle aerodynamics are highly dependent on propulsive effects, accurate propulsion characterization is essential for understanding vehicle aerodynamics and developing aerodynamic databases used for high-fidelity simulator development.
- Different manufacturing practices for propeller production can significantly change performance characteristics. Manufacturing techniques for different propeller orientations should be identical to the largest extent possible to avoid propulsive asymmetries.

This report documented several testing techniques that could be useful for future isolated propeller tests for eVTOL vehicles and provides progress in a new area of aerodynamic research supporting introductions of a future UAM transportation system. Future eVTOL propulsion testing studies are anticipated to further refine testing strategies and understand phenomena occurring for propellers operating at incidence.

Acknowledgments

This research was funded by the NASA Aeronautics Research Mission Directorate (ARMD) Transformational Tools and Technologies (TTT) project. Testing support was provided by Earl Harris, Ronald Busan, Sue Grafton, and Wes O'Neal. Photography support was provided by Lee Pollard. LA-8 hardware support was provided by David North, Gregory Howland, Steven Geuther, and Robert McSwain. Propeller wind tunnel testing advice and lessons learned obtained from John Foster were crucial to the success of this research effort. Additionally, discussions with Paul Rothhaar, Ronald Busan, Patrick Murphy, Barton Bacon, and Kasey Ackerman about their experience with the GL-10 aircraft assisted this effort.

References

1. Silva, C., Johnson, W., Antcliff, K. R., and Patterson, M. D., "VTOL Urban Air Mobility Concept Vehicles for Technology Development," *2018 Aviation Technology, Integration, and Operations Conference*, AIAA Paper 2018-3847, Jun. 2018. https://doi.org/10.2514/6.2018-3847.

2. Antcliff, K. R., Whiteside, S. K. S., Kohlman, L. W., and Silva, C., "Baseline Assumptions and Future Research Areas for Urban Air Mobility Vehicles," *AIAA SciTech 2019 Forum*, AIAA Paper 2019-0528, Jan. 2019. https://doi.org/10.2514/6.2019-0528.

3. Rothhaar, P. M., Murphy, P. C., Bacon, B. J., Gregory, I. M., Grauer, J. A., Busan, R. C., and Croom, M. A., "NASA Langley Distributed Propulsion VTOL TiltWing Aircraft Testing, Modeling, Simulation, Control, and Flight Test Development," *14th AIAA Aviation Technology, Integration, and Operations Conference*, AIAA Paper 2014-2999, Jun. 2014. https://doi.org/10.2514/6.2014-2999.

4. North, D. D., Howland, G., and Busan, R. C., "Design and Fabrication of the LA-8 Distributed Electric Propulsion VTOL Testbed," *AIAA SciTech 2021 Forum*, AIAA Paper 2021-1188, Jan. 2021. https://doi.org/10.2514/6.2021-1188.

5. Geuther, S. C., North, D. D., and Busan, R. C., "Investigation of a Tandem Tilt-wing VTOL Aircraft in the NASA Langley 12-Foot Low-Speed Tunnel," NASA TM-2020-5003178, Jun. 2020.

6. McSwain, R. G., Geuther, S. C., Howland, G., Patterson, M. D., Whiteside, S. K., and North, D. D., "An Experimental Approach to a Rapid Propulsion and Aeronautics Concepts Testbed," NASA TM-2020-220437, Jan. 2020.

7. Busan, R. C., Murphy, P. C., Hatke, D. B., and Simmons, B. M., "Wind Tunnel Testing Techniques for a Tandem Tilt-Wing, Distributed Electric Propulsion VTOL Aircraft," *AIAA SciTech 2021 Forum*, AIAA Paper 2021-1189, Jan. 2021. https://doi.org/10.2514/6.2021-1189.

8. Murphy, P. C., Simmons, B. M., Hatke, D. B., and Busan, R. C., "Rapid Aero Modeling for Urban Air Mobility Aircraft in Wind-Tunnel Tests," *AIAA SciTech 2021 Forum*, AIAA Paper 2021-1644, Jan. 2021. https://doi.org/10.2514/6.2021-1644.

9. Cook, J., and Gregory, I., "A Robust Uniform Control Approach for VTOL Aircraft," *VFS Autonomous VTOL Technical Meeting and Electric VTOL Symposium*, Jan. 2021.

10. Simmons, B. M., "System Identification for Propellers at High Incidence Angles," *AIAA SciTech 2021 Forum*, AIAA Paper 2021-1190, Jan. 2021. https://doi.org/10.2514/6.2021-1190.

11. Simmons, B. M., and Murphy, P. C., "Wind Tunnel-Based Aerodynamic Model Identification for a Tilt-Wing, Distributed Electric Propulsion Aircraft," *AIAA SciTech 2021 Forum*, AIAA Paper 2021-1298, Jan. 2021. https://doi.org/10.2514/6.2021-1298.

12. Geuther, S. C., and Fei, X., "LA-8 Computational Analysis and Validation Studies Using FlightStream," *AIAA SciTech 2021 Forum*, AIAA Paper 2021-1191, Jan. 2021. https://doi.org/10.2514/6.2021-1191.

13. Stratton, M., and Landman, D., "Wind Tunnel Test and Empirical Modeling of Tilt-Rotor Performance for eVTOL Applications," *AIAA SciTech 2021 Forum*, AIAA Paper 2021-0834, Jan. 2021. https://doi.org/10.2514/6.2021-0834.

14. McCormick, B. W., *Aerodynamics, Aeronautics, and Flight Mechanics*, 2nd ed., John Wiley & Sons, New York, NY, 1995.

15. Dommasch, D. O., *Elements of Propeller and Helicopter Aerodynamics*, Pitman Publishing Corporation, 1953.

16. Phillips, W. F., *Mechanics of Flight*, 2nd ed., John Wiley & Sons, Hoboken, NJ, 2010.

17. Greitzer, E. M., Spakovszky, Z. S., and Waitz, I. A., "Thermodynamics and Propulsion," *Lecture Notes, Massachusetts Institute of Technology*, 2006. URL http://web.mit.edu/16.unified/www/FALL/thermodynamics/notes/node86.html, accessed March 2021.

18. Singleton, J. D., and Yeager, W. T., "Important Scaling Parameters for Testing Model-Scale Helicopter Rotors," *Journal of Aircraft*, Vol. 37, No. 3, 2000, pp. 396–402. https://doi.org/10.2514/2.2639.

19. Leishman, J. G., *Principles of Helicopter Aerodynamics*, 2nd ed., Cambridge University Press, Cambridge, UK, 2016.

20. Brandt, J., and Selig, M., "Propeller Performance Data at Low Reynolds Numbers," *49th AIAA Aerospace Sciences Meeting including the New Horizons Forum and Aerospace Exposition*, AIAA Paper 2011-1255, Jan. 2011. https://doi.org/10.2514/6.2011-1255.

21. Deters, R. W., Ananda, G. K., and Selig, M. S., "Reynolds Number Effects on the Performance of Small-Scale Propellers," *32nd AIAA Applied Aerodynamics Conference*, AIAA Paper 2014-2151, Jun. 2014. https://doi.org/10.2514/6.2014-2151.

22. Ribner, H. S., "Propellers in Yaw," NACA TR-820, 1945.

23. Ribner, H. S., "Formulas for Propellers in Yaw and Charts of the Side-Force Derivative," NACA TR-819, 1945.

24. Crigler, J. L., and Gilman Jr., J., "Calculation of Aerodynamic Forces on a Propeller in Pitch or Yaw," NACA TN-2585, Jan. 1952.

25. De Young, J., "Propeller at High Incidence," *Journal of Aircraft*, Vol. 2, No. 3, 1965, pp. 241–250. https://doi.org/10.2514/3.43646.

26. Smith, H. R., "Engineering Models of Aircraft Propellers at Incidence," Ph.D. thesis, University of Glasgow, Jan. 2015.

27. McCormick, B. W., Aljabri, A. S., Jumper, S. J., and Martinovic, Z. N., "The Analysis of Propellers Including Interaction Effects," NASA CR-158111, 1979.

28. Theys, B., Dimitriadis, G., Hendrick, P., and De Schutter, J., "Experimental and Numerical Study of Micro-Aerial-Vehicle Propeller Performance in Oblique Flow," *Journal of Aircraft*, Vol. 54, No. 3, 2017, pp. 1076–1084. https://doi.org/10.2514/1.C033618.

29. Leng, Y., Yoo, H., Jardin, T., Bronz, M., and Moschetta, J.-M., "Aerodynamic Modeling of Propeller Forces and Moments at High Angle of Incidence," *AIAA SciTech 2019 Forum*, AIAA Paper 2019-1332, Jan. 2019. https://doi.org/10.2514/6.2019-1332.

30. McLemore, H. C., and Cannon, M. D., "Aerodynamic Investigation of a Four-Blade Propeller Operating through an Angle-of-Attack Range from 0° to 180°," NACA TN-3228, Jun. 1954.

31. Yaggy, P. F., and Rogallo, V. L., "A Wind-Tunnel Investigation of Three Propellers Through an Angle-of-Attack Range from 0° to 85°," NASA TN D-318, May 1960.

32. Kuhn, R. E., and Draper, J. W., "Investigation of the Aerodynamic Characteristics of a Model Wing-Propeller Combination and of the Wing and Propeller Separately at Angles of Attack up to 90°," NACA TR-1263, 1956.

33. Johnson, W., *Rotorcraft Aeromechanics*, Cambridge University Press, 2013.

34. Foster, J. V., and Hartman, D. C., "High-Fidelity Multi-Rotor Unmanned Aircraft System (UAS) Simulation Development for Trajectory Prediction Under Off-Nominal Flight Dynamics," *17th AIAA Aviation Technology, Integration, and Operations Conference*, AIAA Paper 2017-3271, Jun. 2017. https://doi.org/10.2514/6.2017-3271.

35. Theys, B., Dimitriadis, G., Andrianne, T., Hendrick, P., and De Schutter, J., "Wind Tunnel Testing of a VTOL MAV Propeller in Tilted Operating Mode," *2014 International Conference on Unmanned Aircraft Systems (ICUAS)*, May 2014, pp. 1064–1072. https://doi.org/10.1109/ICUAS.2014.6842358.

36. Leng, Y., Jardin, T., Bronz, M., and Moschetta, J.-M., "Experimental Analysis of Propeller Forces and Moments at High Angle of Incidence," *AIAA SciTech 2019 Forum*, AIAA Paper 2019-1331, Jan. 2019. https://doi.org/10.2514/6.2019-1331.

37. Bronz, M., and Karaman, S., "Preliminary Experimental Investigation of Small Scale Propellers at High Incidence Angle," *2018 AIAA Aerospace Sciences Meeting*, AIAA Paper 2018-1268, Jan. 2018. https://doi.org/10.2514/6.2018-1268.

38. Ol, M., Zeune, C., and Logan, M., "Analytical – Experimental Comparison for Small Electric Unmanned Air Vehicle Propellers," *26th AIAA Applied Aerodynamics Conference*, AIAA Paper 2008-7345, Aug. 2008. https://doi.org/10.2514/6.2008-7345.

39. Merchant, M. P., and Miller, L. S., "Propeller Performance Measurement for Low Reynolds Number UAV Applications," *44th AIAA Aerospace Sciences Meeting and Exhibit*, AIAA Paper 2006-1127, Jan. 2006. https://doi.org/10.2514/6.2006-1127.

40. Johnson, W., "Model for Vortex Ring State Influence on Rotorcraft Flight Dynamics," NASA TP-2005-213477, Dec. 2005.

41. Morelli, E. A., and Klein, V., *Aircraft System Identification: Theory and Practice*, 2nd ed., Sunflyte Enterprises, Williamsburg, VA, 2016.

42. Morelli, E. A., "High Accuracy Evaluation of the Finite Fourier Transform Using Sampled Data," NASA TM-110340, Jun. 1997.

43. Morelli, E. A., "Estimating Noise Characteristics from Flight Test Data using Optimal Fourier Smoothing," *Journal of Aircraft*, Vol. 32, No. 4, 1995, pp. 689–695. https://doi.org/10.2514/3.46778.

Appendix A

Additional Figures

This appendix contains additional figures to accompany the discussion of isolated propeller wind tunnel test results in Section 4.

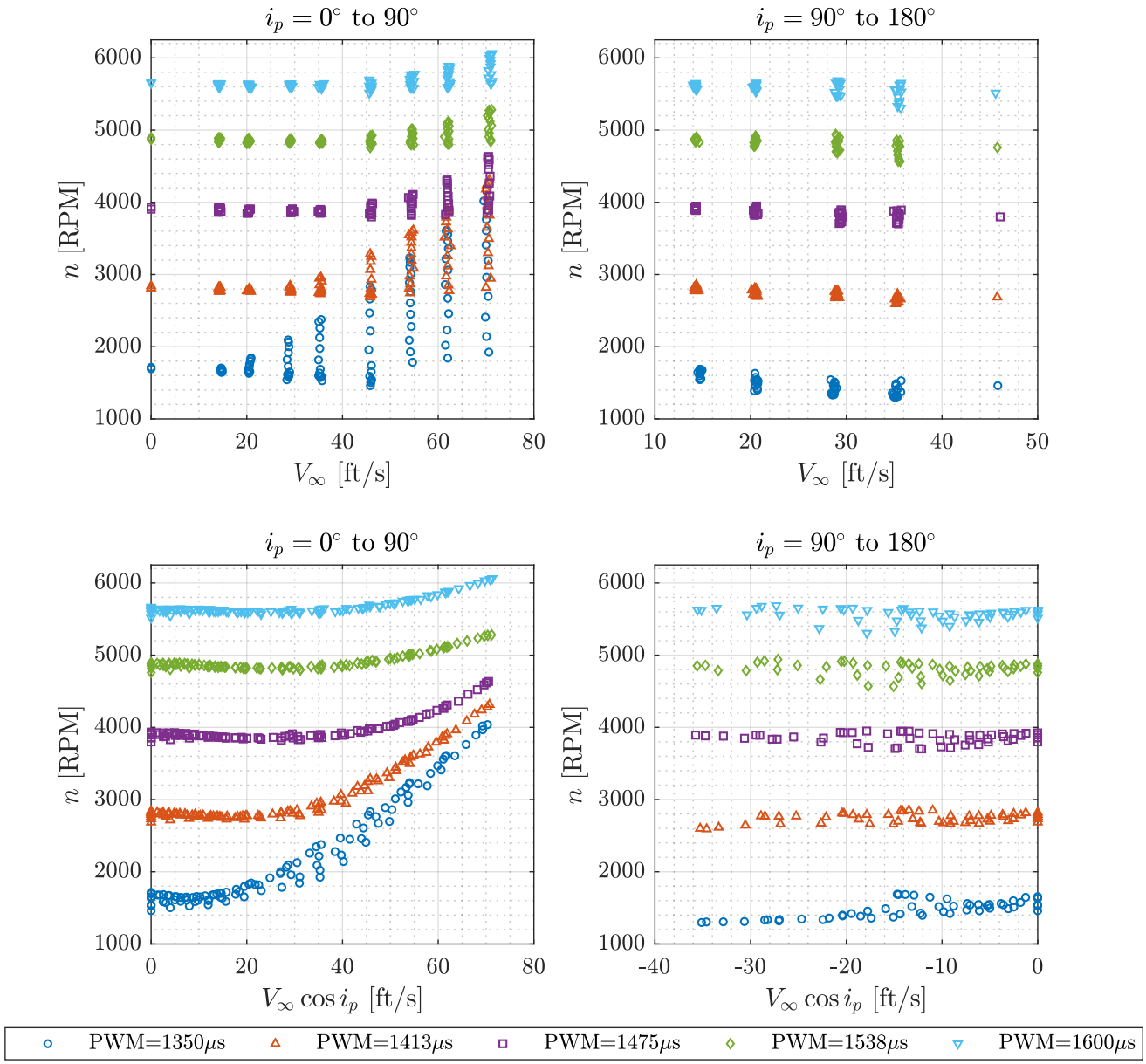

Figure 11. CW propeller rotational speed variation with airspeed V_∞ and the normal component of airspeed $V_\infty \cos i_p$.

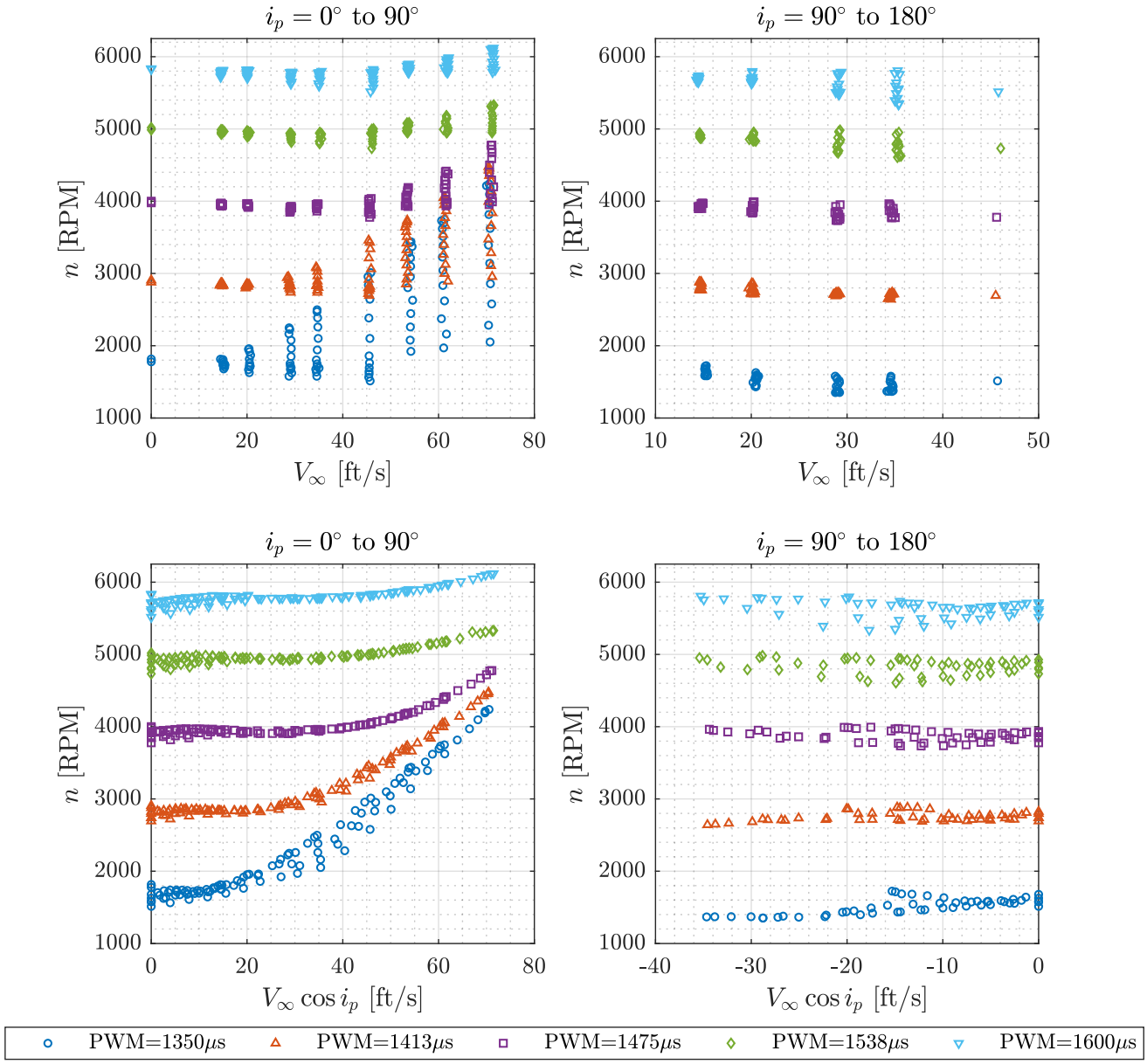

Figure 12. CCW propeller rotational speed variation with airspeed V_∞ and the normal component of airspeed $V_\infty \cos i_p$.

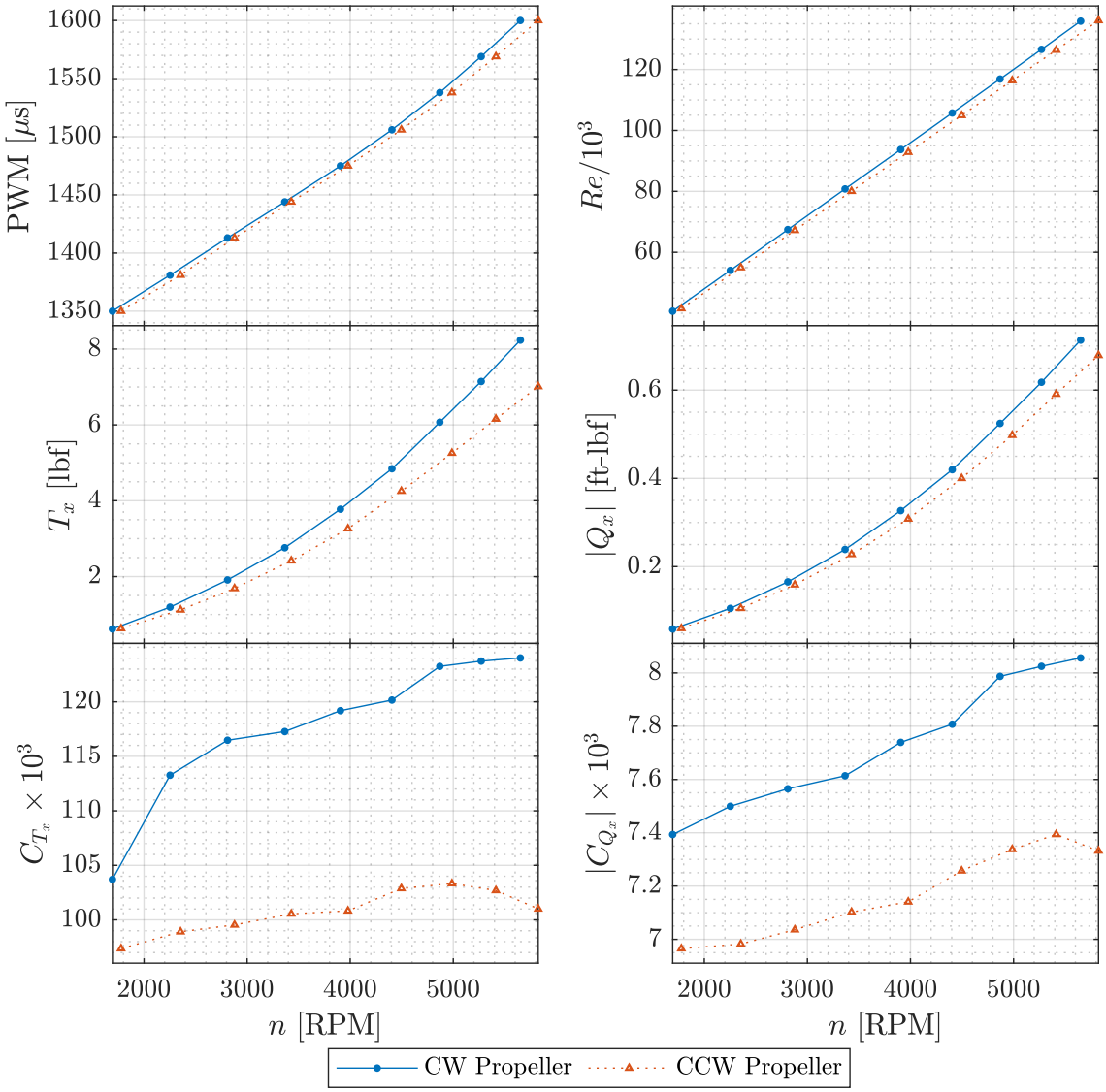

Figure 13. Static CW and CCW propeller data ($\bar{q} = 0$ psf).

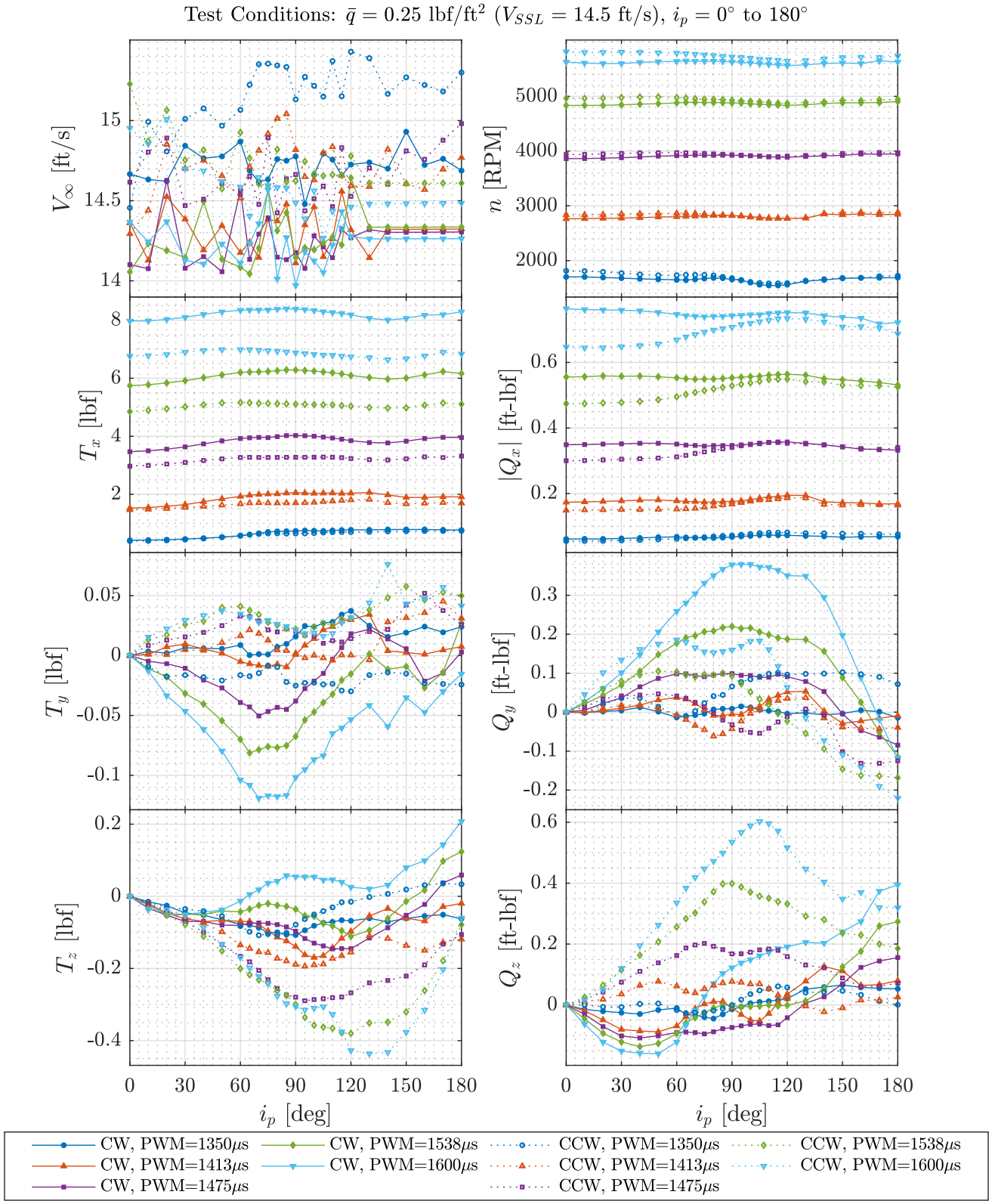

Figure 14. CW and CCW propeller forces and moments variation with i_p at $\bar{q} = 0.25$ psf.

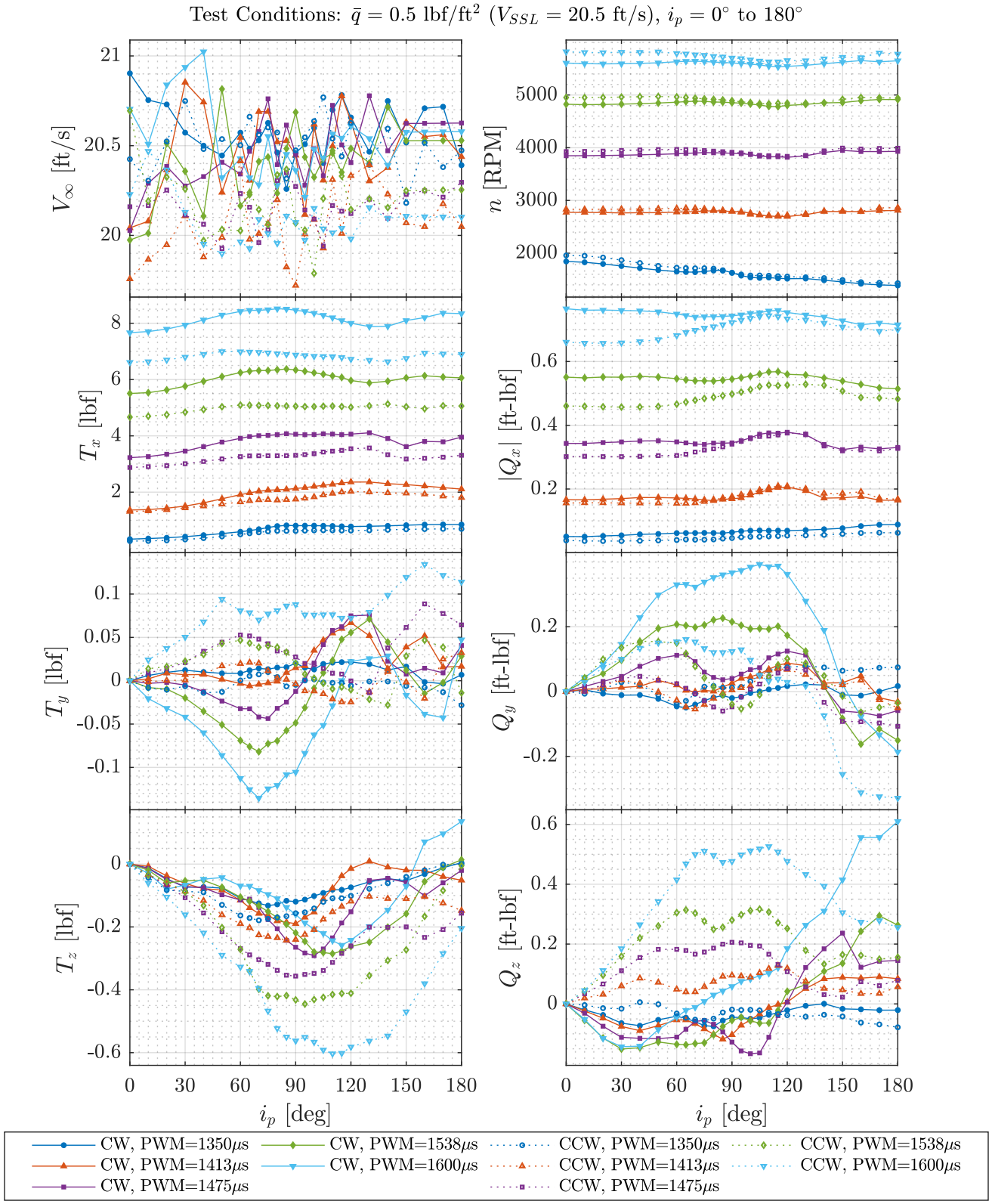

Figure 15. CW and CCW propeller forces and moments variation with i_p at $\bar{q} = 0.5$ psf.

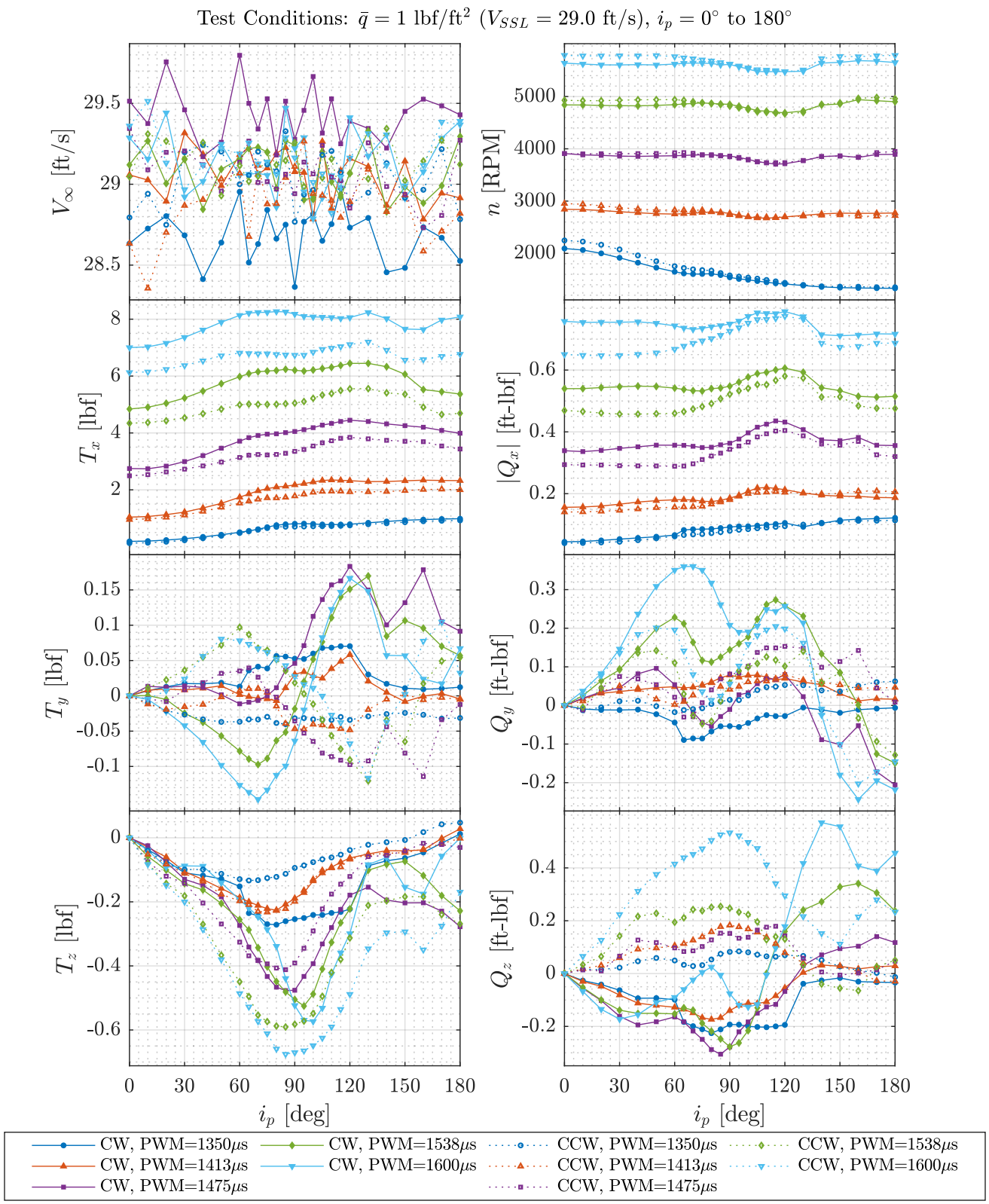

Figure 16. CW and CCW propeller forces and moments variation with i_p at $\bar{q} = 1$ psf.

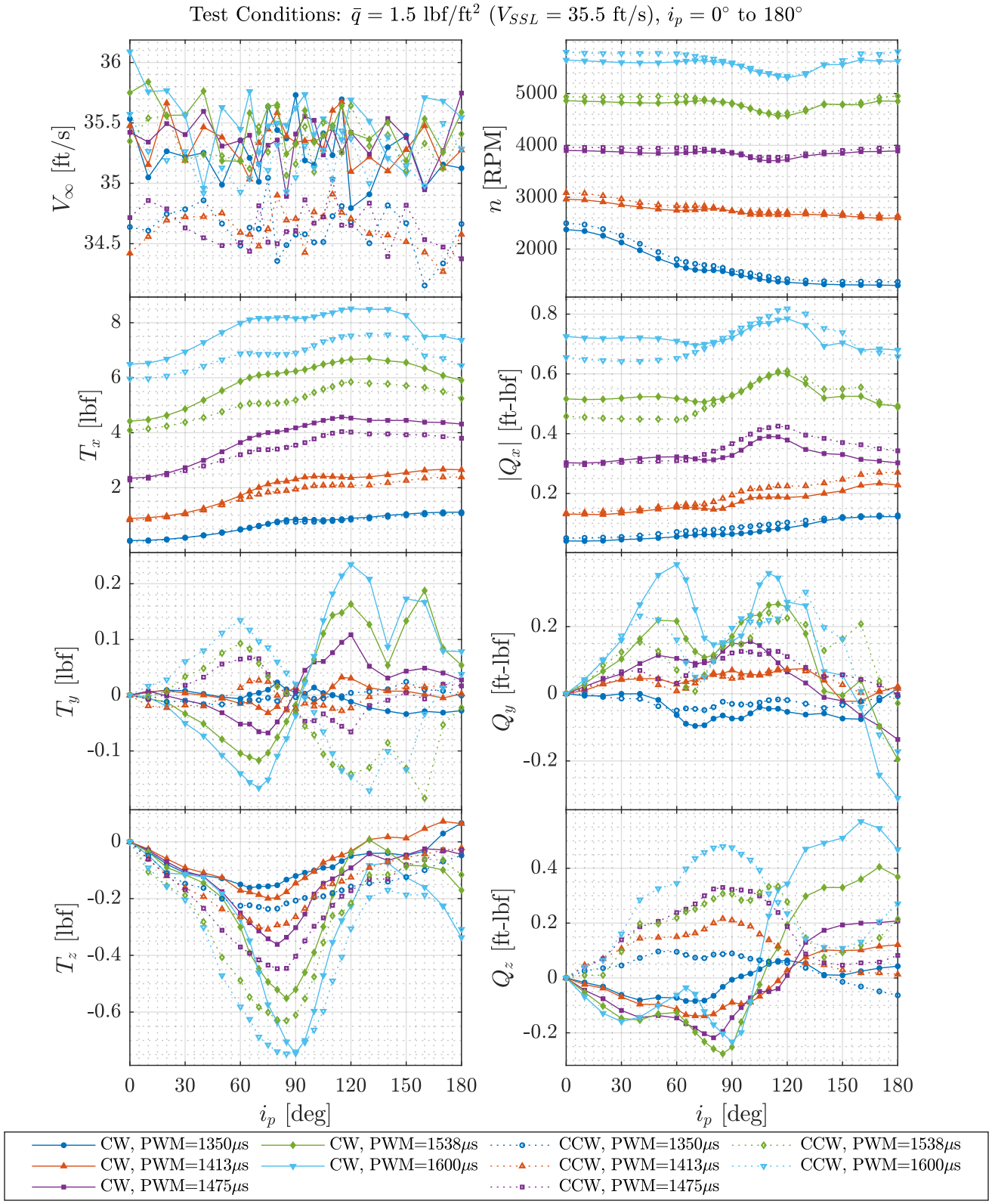

Figure 17. CW and CCW propeller forces and moments variation with i_p at $\bar{q} = 1.5$ psf.

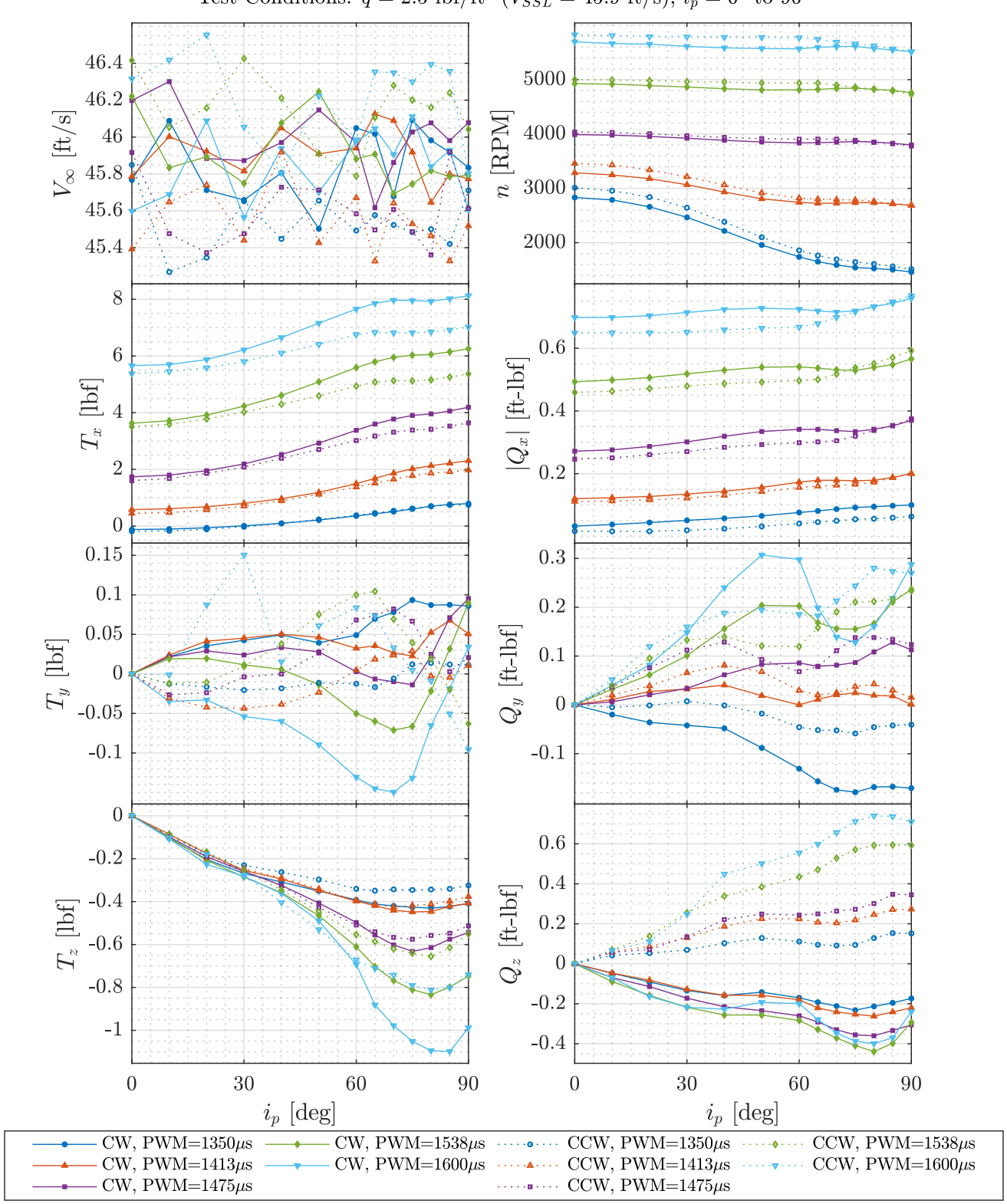

Figure 18. CW and CCW propeller forces and moments variation with i_p at $\bar{q} = 2.5$ psf.

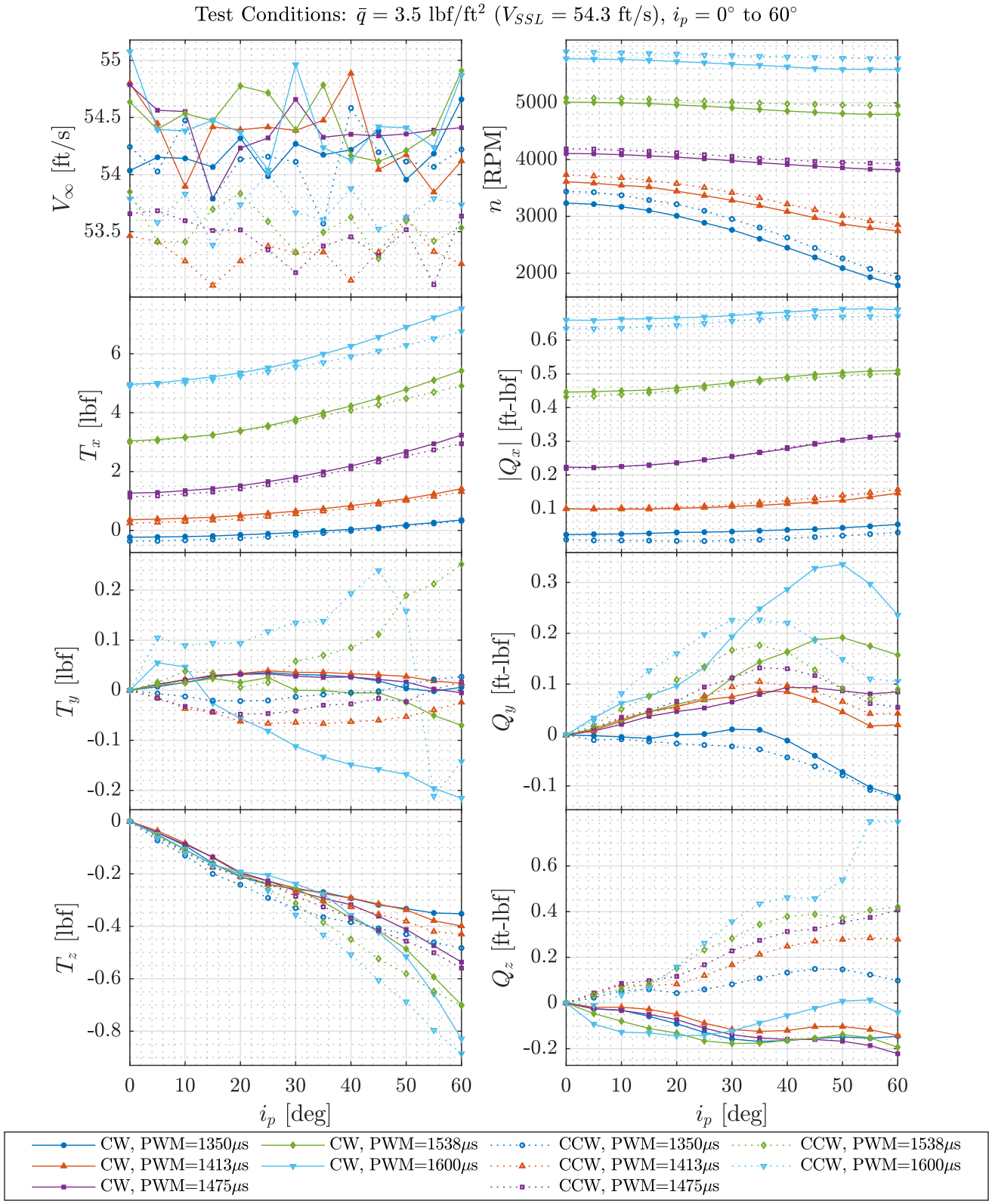

Figure 19. CW and CCW propeller forces and moments variation with i_p at $\bar{q} = 3.5$ psf.

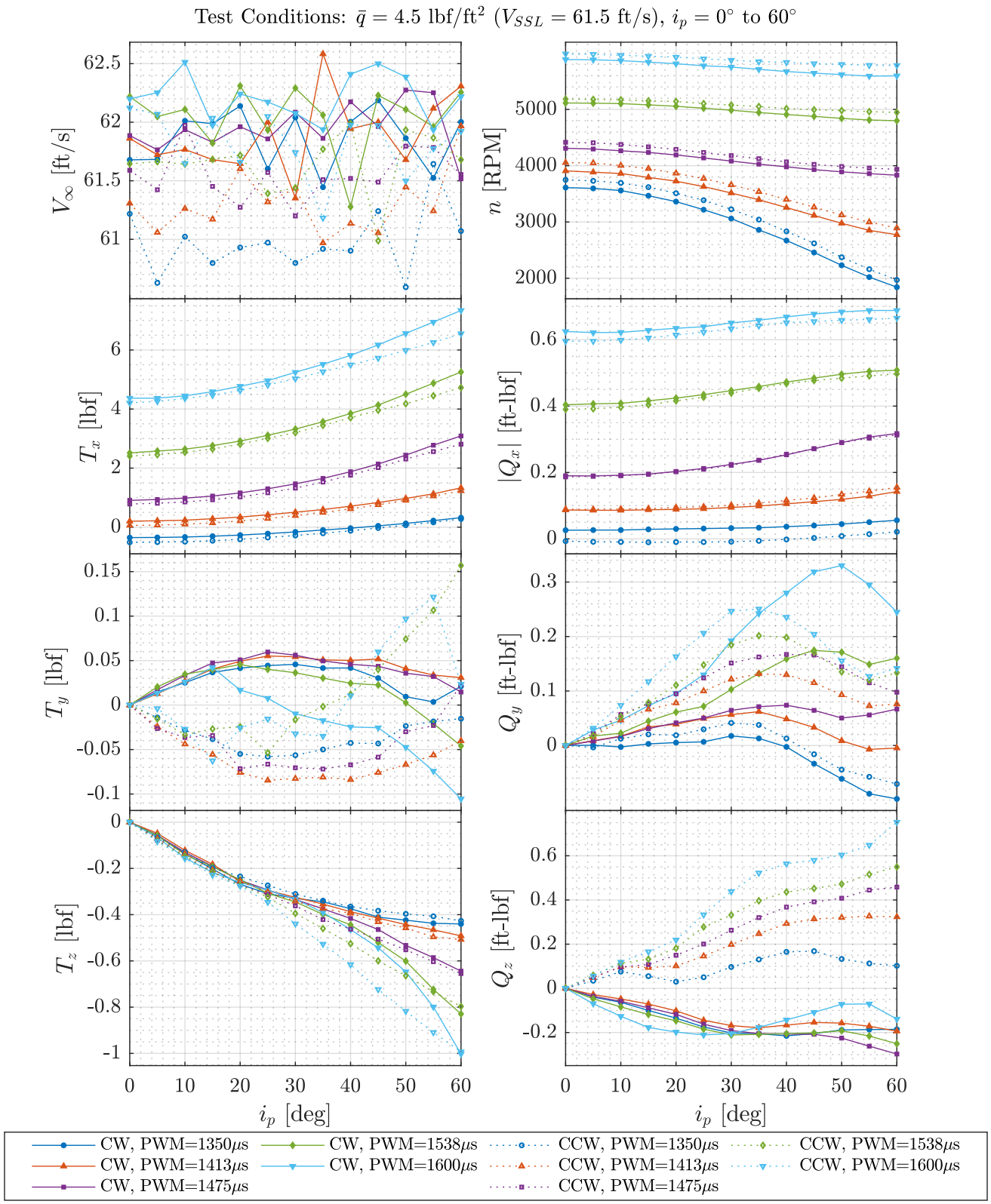

Figure 20. CW and CCW propeller forces and moments variation with i_p at $\bar{q} = 4.5$ psf.

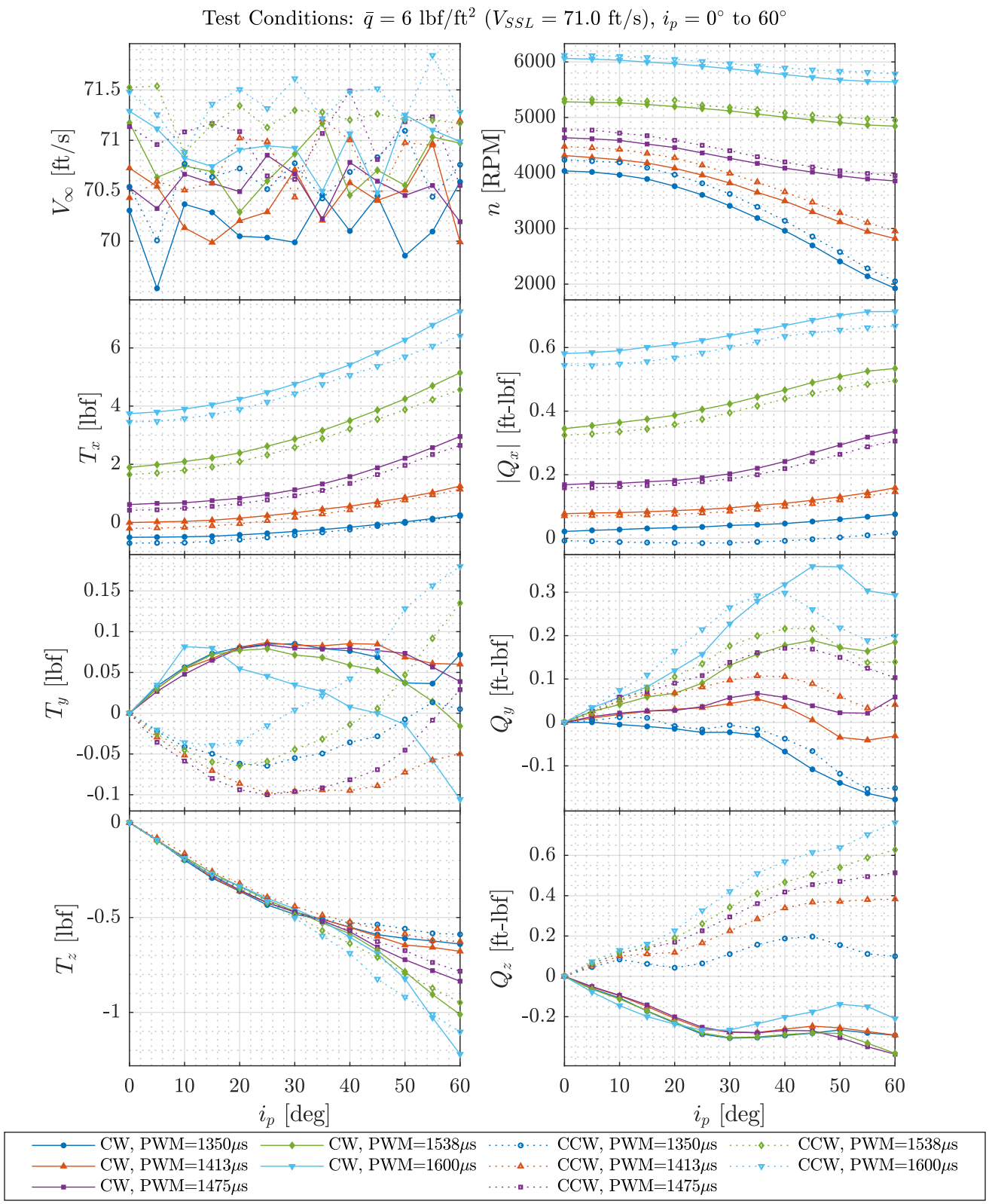

Figure 21. CW and CCW propeller forces and moments variation with i_p at $\bar{q} = 6$ psf.

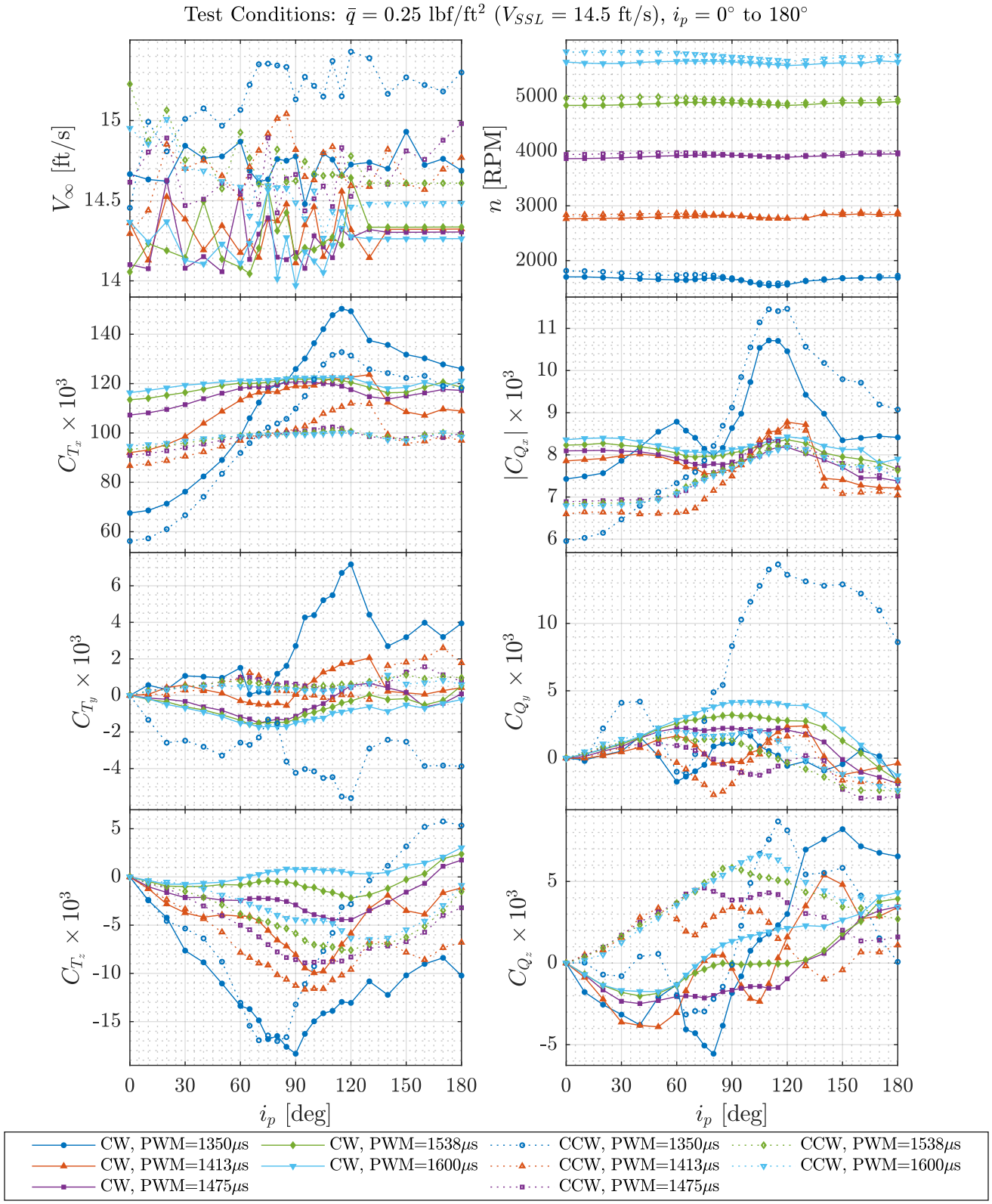

Figure 22. CW and CCW propeller force and moment coefficients variation with i_p at $\bar{q} = 0.25$ psf.

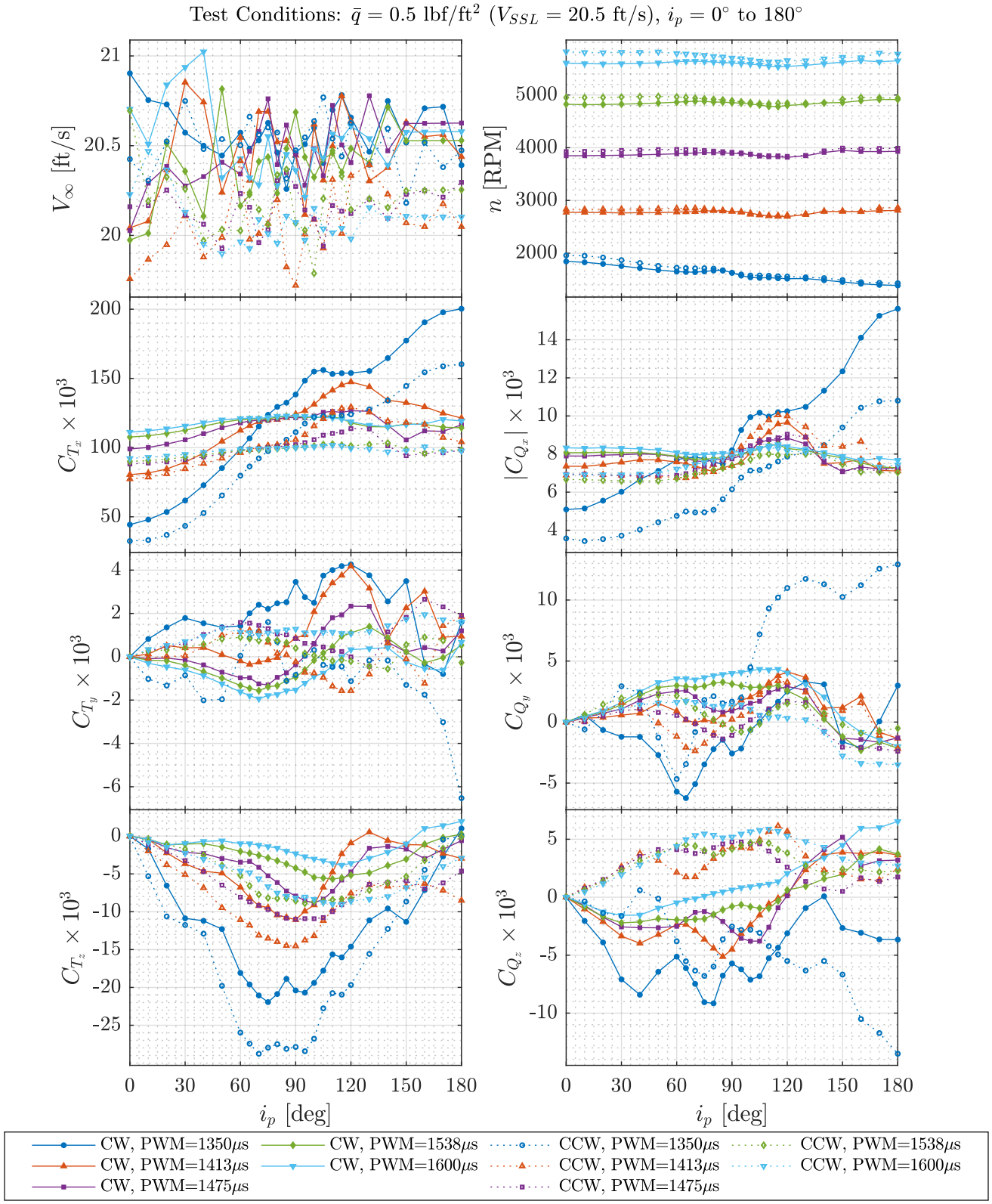

Figure 23. CW and CCW propeller force and moment coefficients variation with i_p at $\bar{q} = 0.5$ psf.

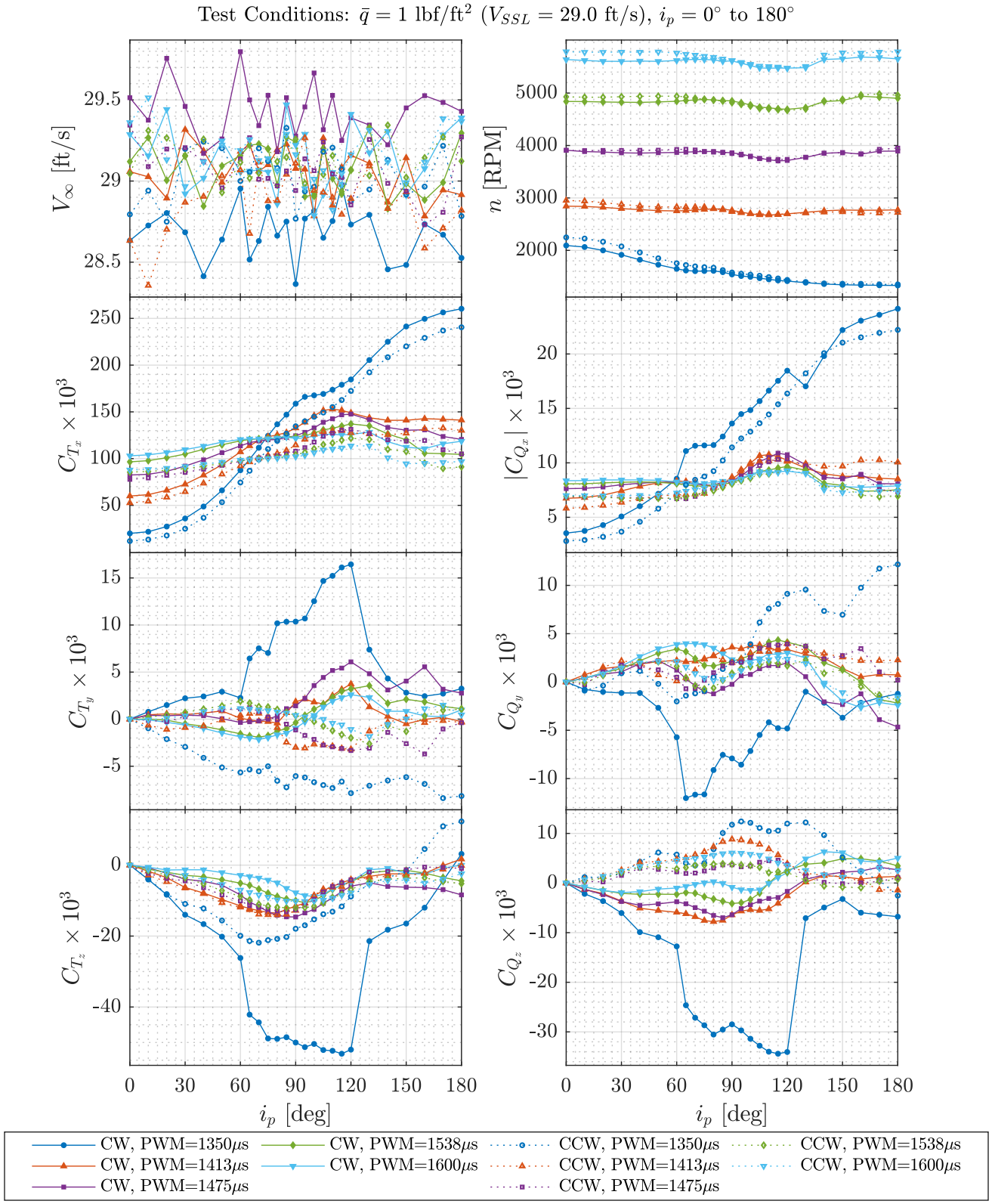

Figure 24. CW and CCW propeller force and moment coefficients variation with i_p at $\bar{q} = 1$ psf.

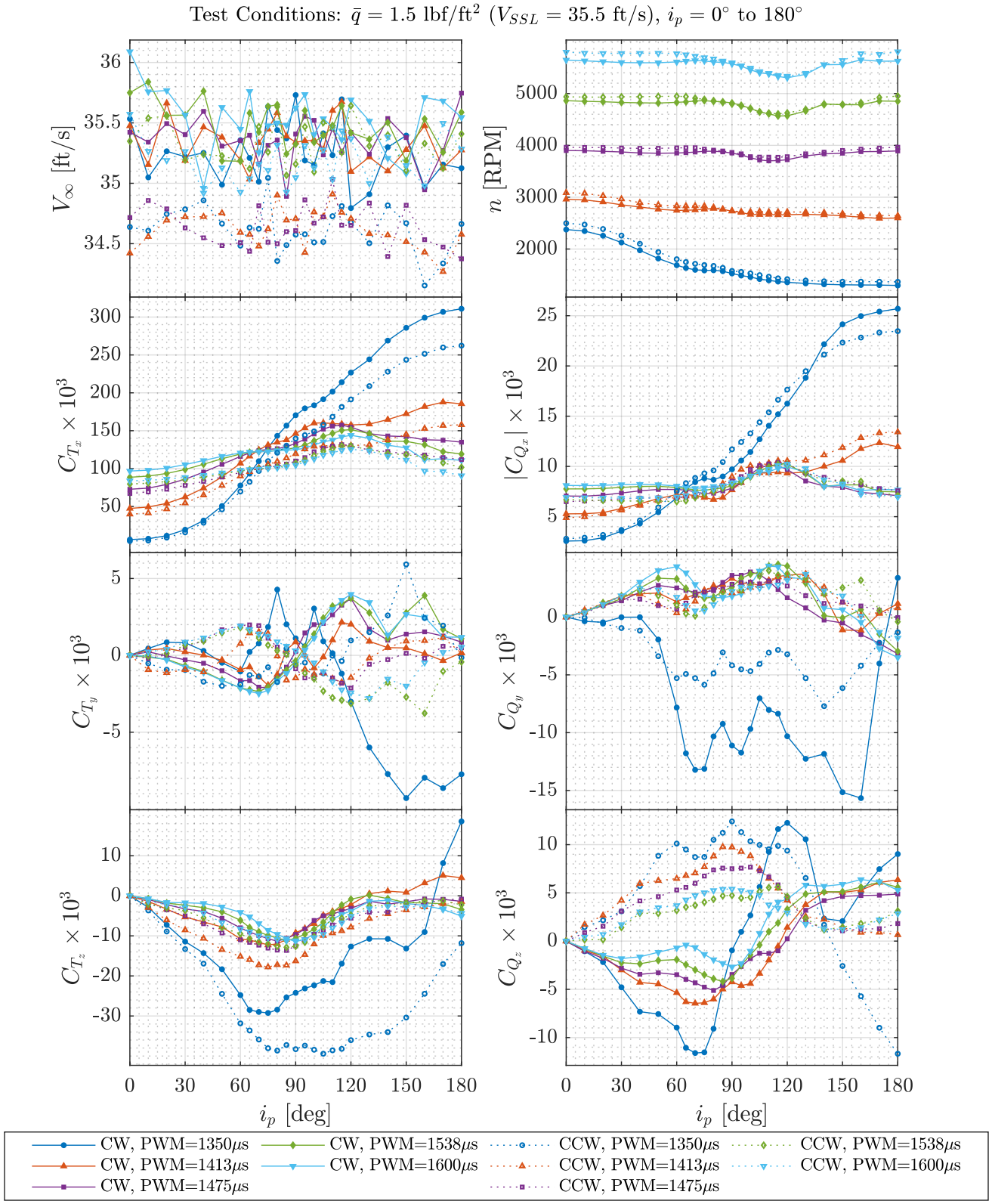

Figure 25. CW and CCW propeller force and moment coefficients variation with i_p at $\bar{q} = 1.5$ psf.

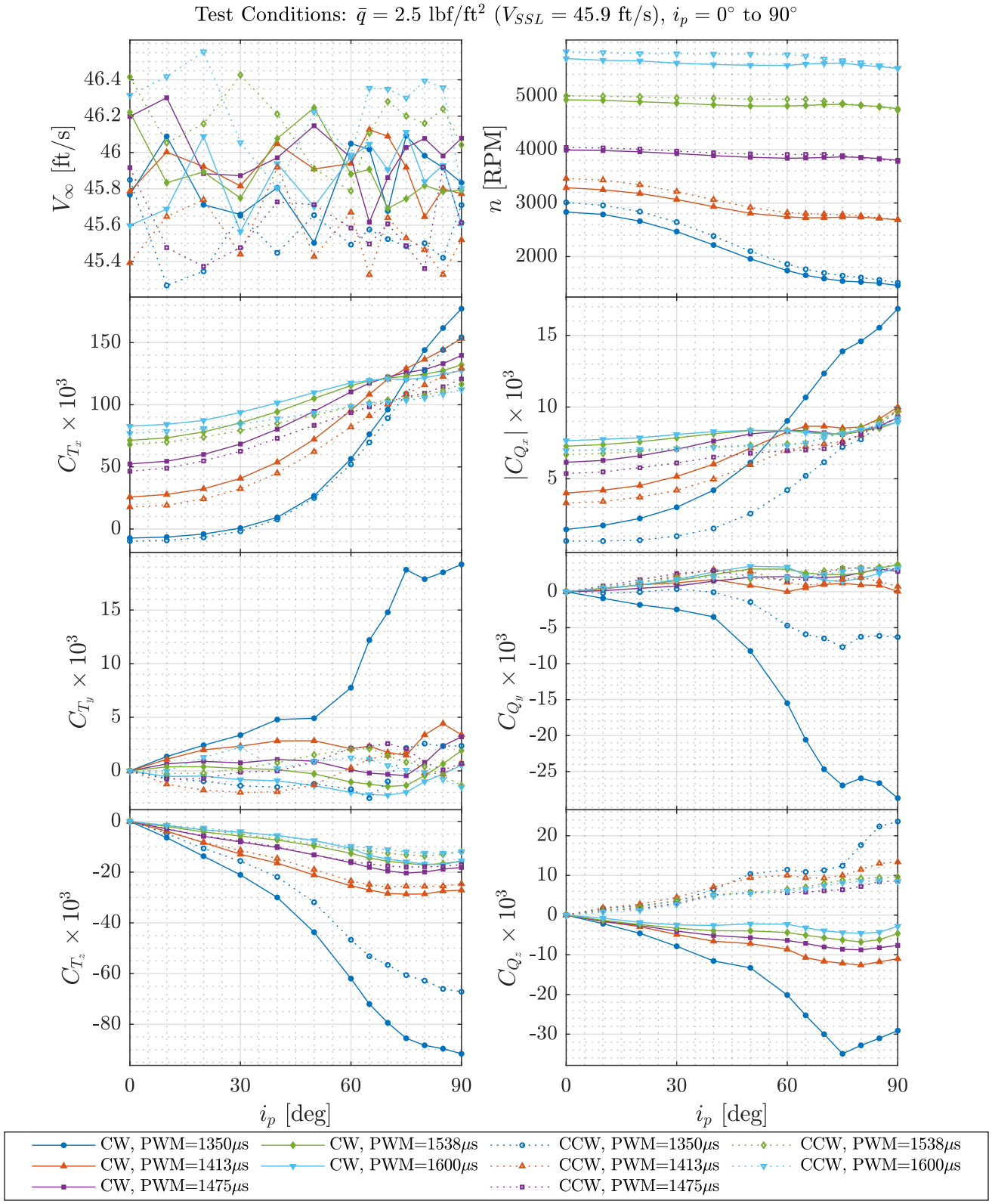

Figure 26. CW and CCW propeller force and moment coefficients variation with i_p at $\bar{q} = 2.5$ psf.

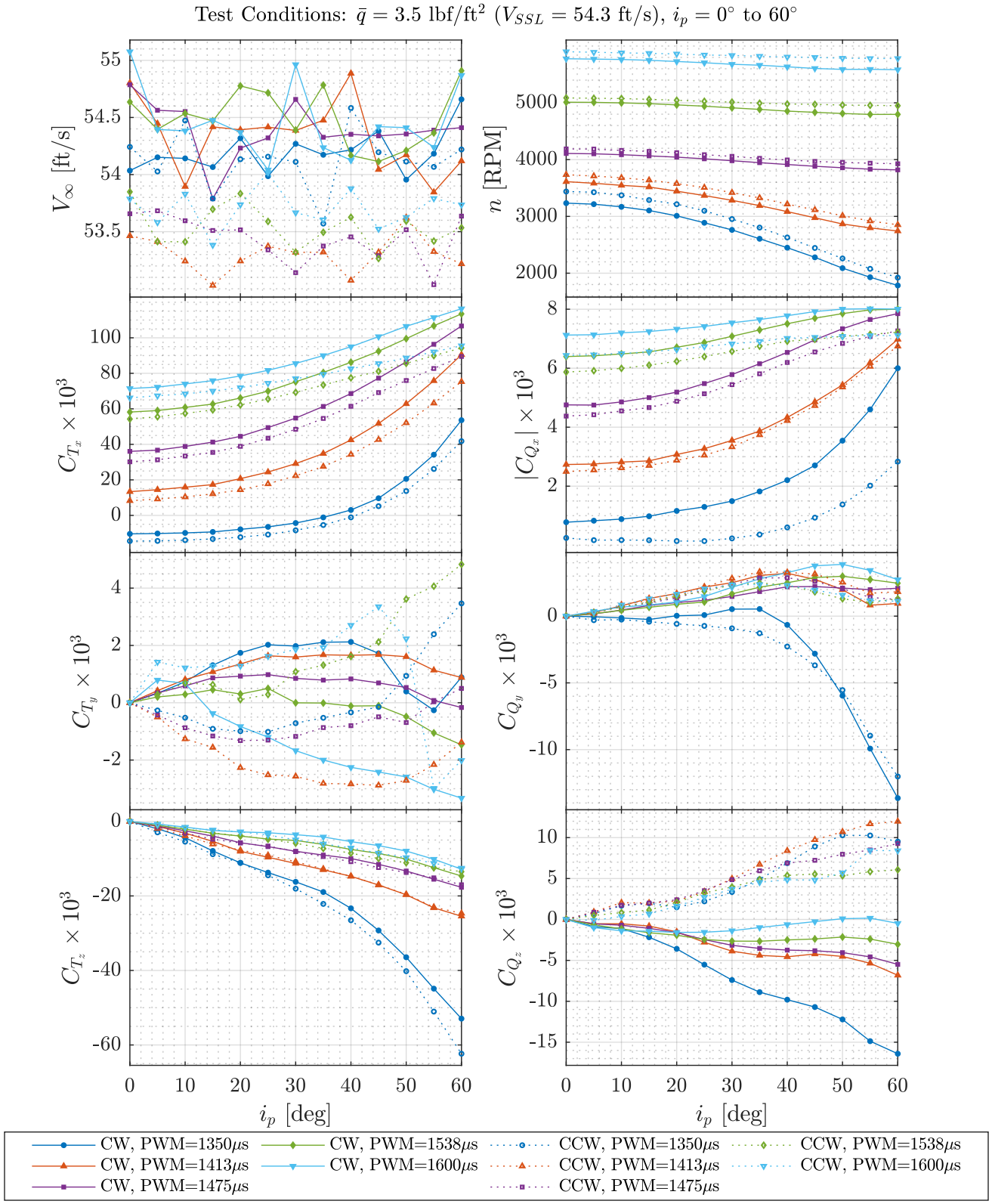

Figure 27. CW and CCW propeller force and moment coefficients variation with i_p at $\bar{q} = 3.5$ psf.

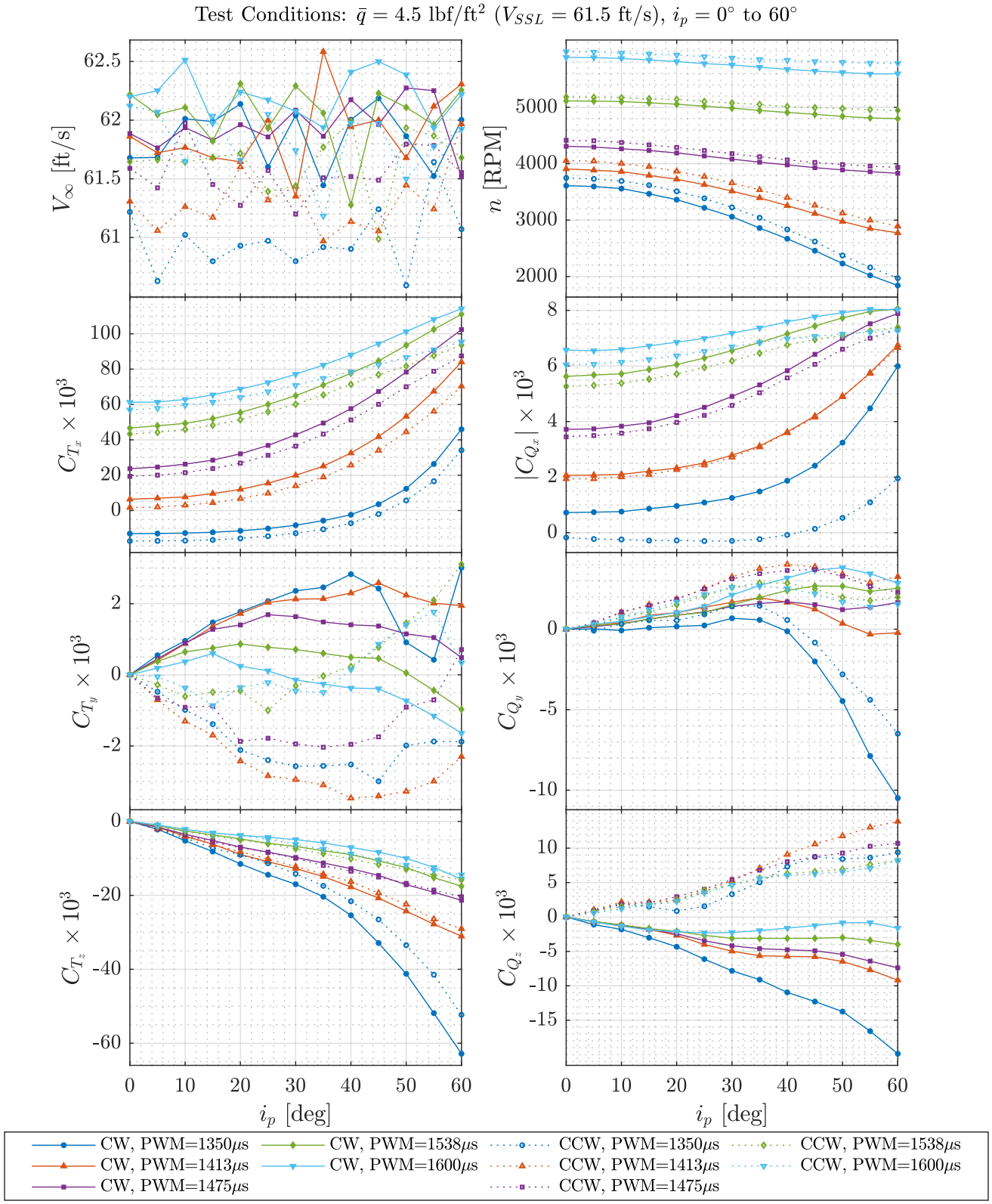

Figure 28. CW and CCW propeller force and moment coefficients variation with i_p at $\bar{q} = 4.5$ psf.

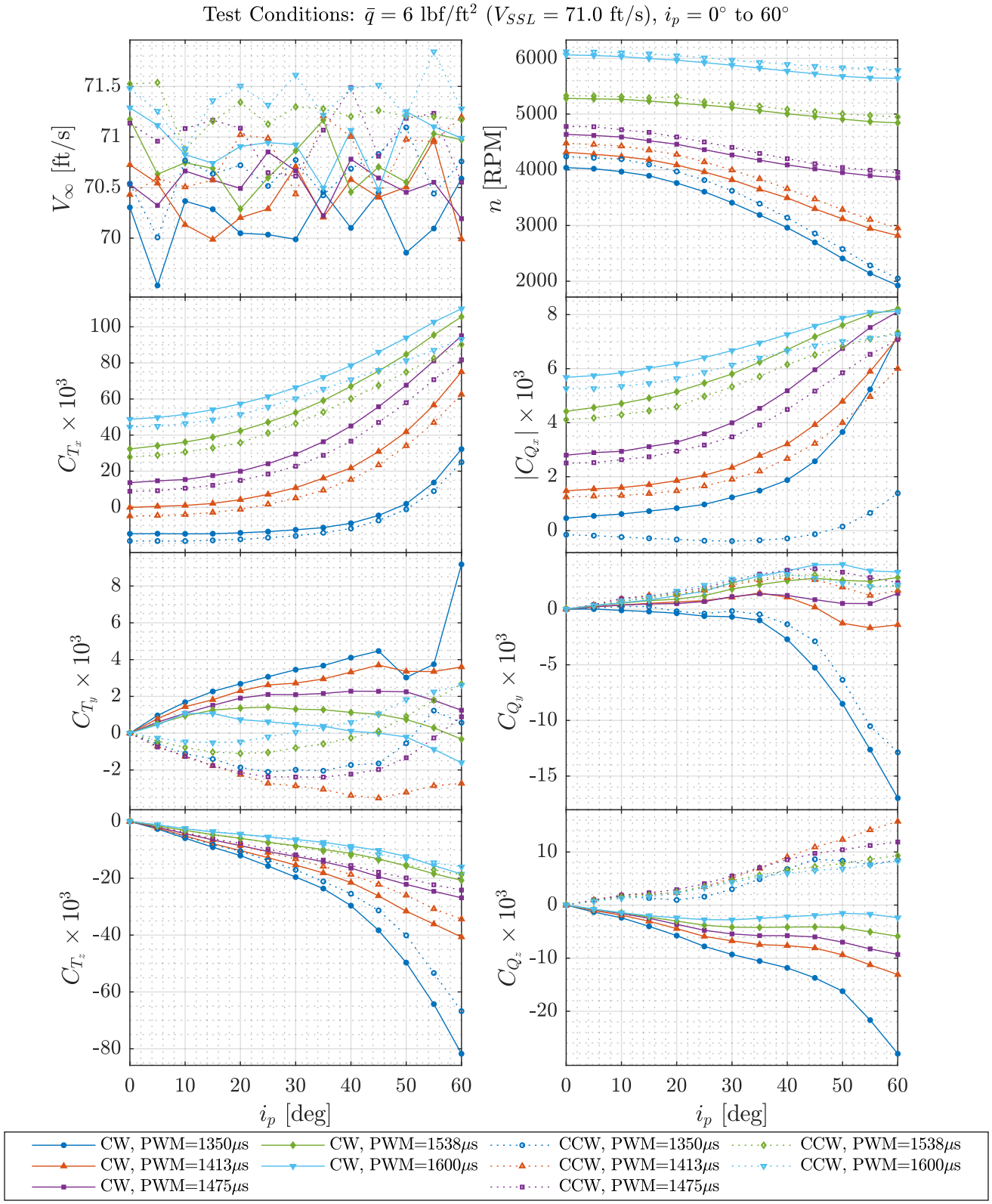

Figure 29. CW and CCW propeller force and moment coefficients variation with i_p at $\bar{q} = 6$ psf.

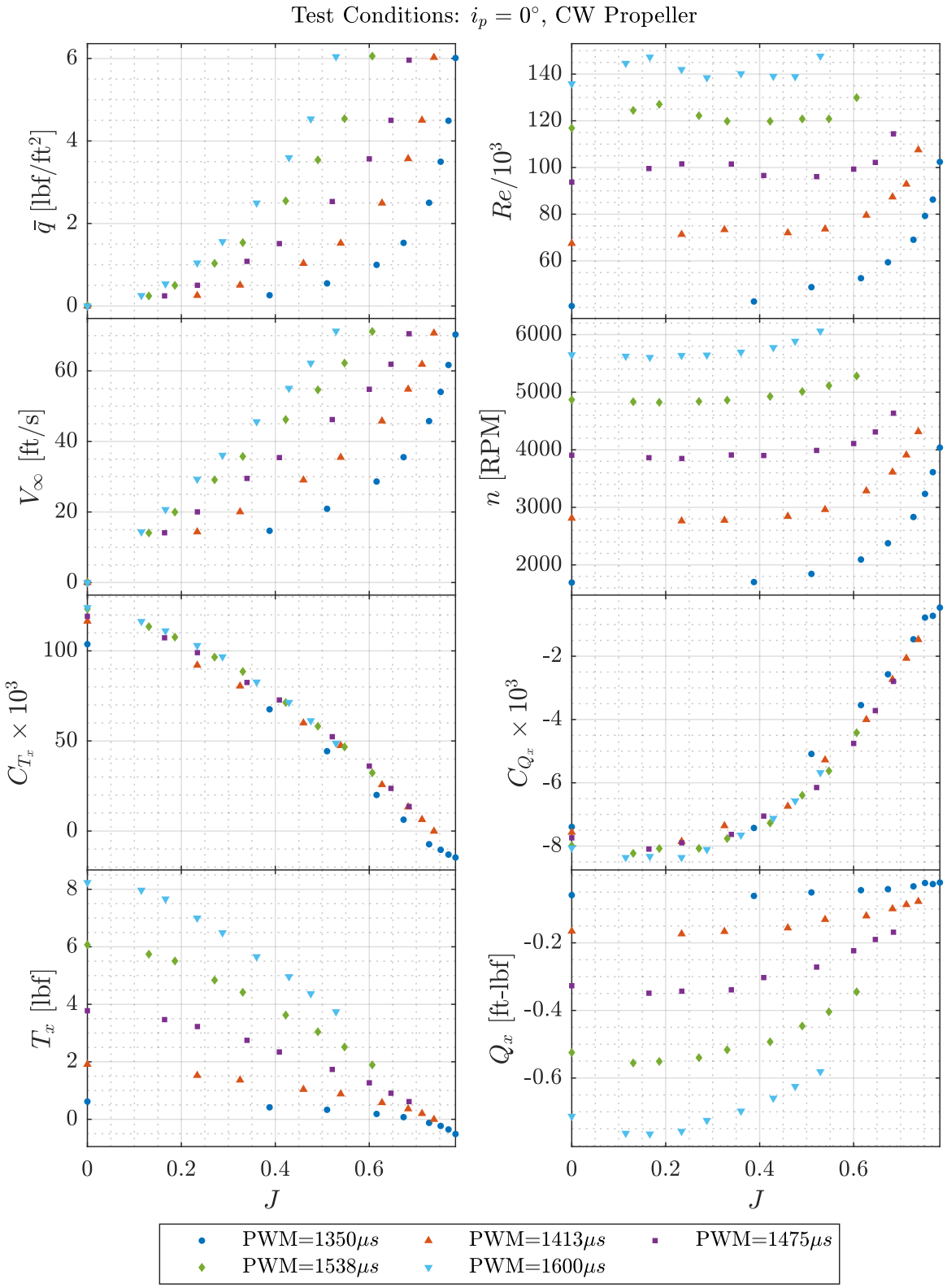

Figure 30. CW propeller thrust, thrust coefficient, torque, and torque coefficient variation with J at $i_p = 0°$.

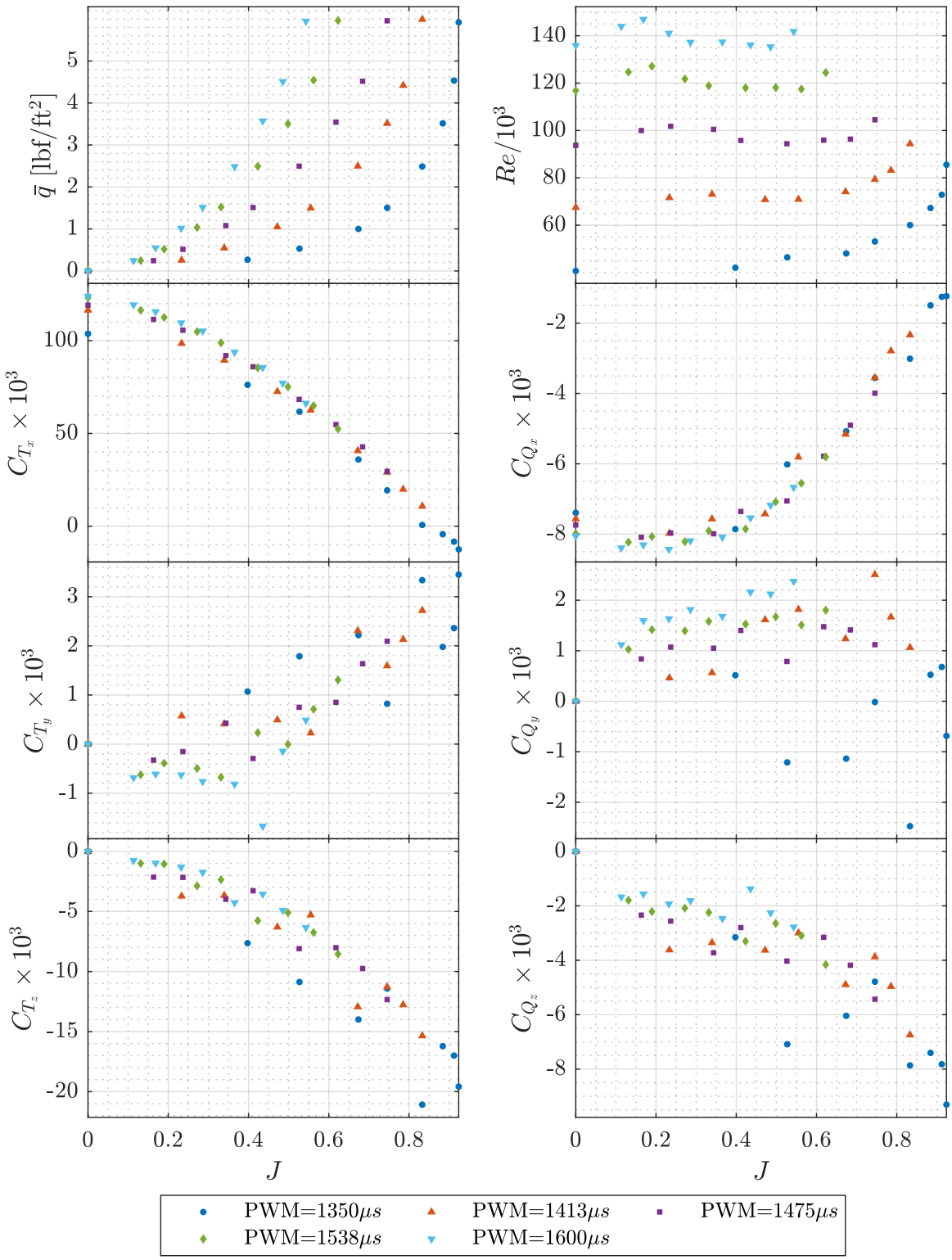

Figure 31. CW propeller force and moment coefficients variation with J at $i_p = 30°$.

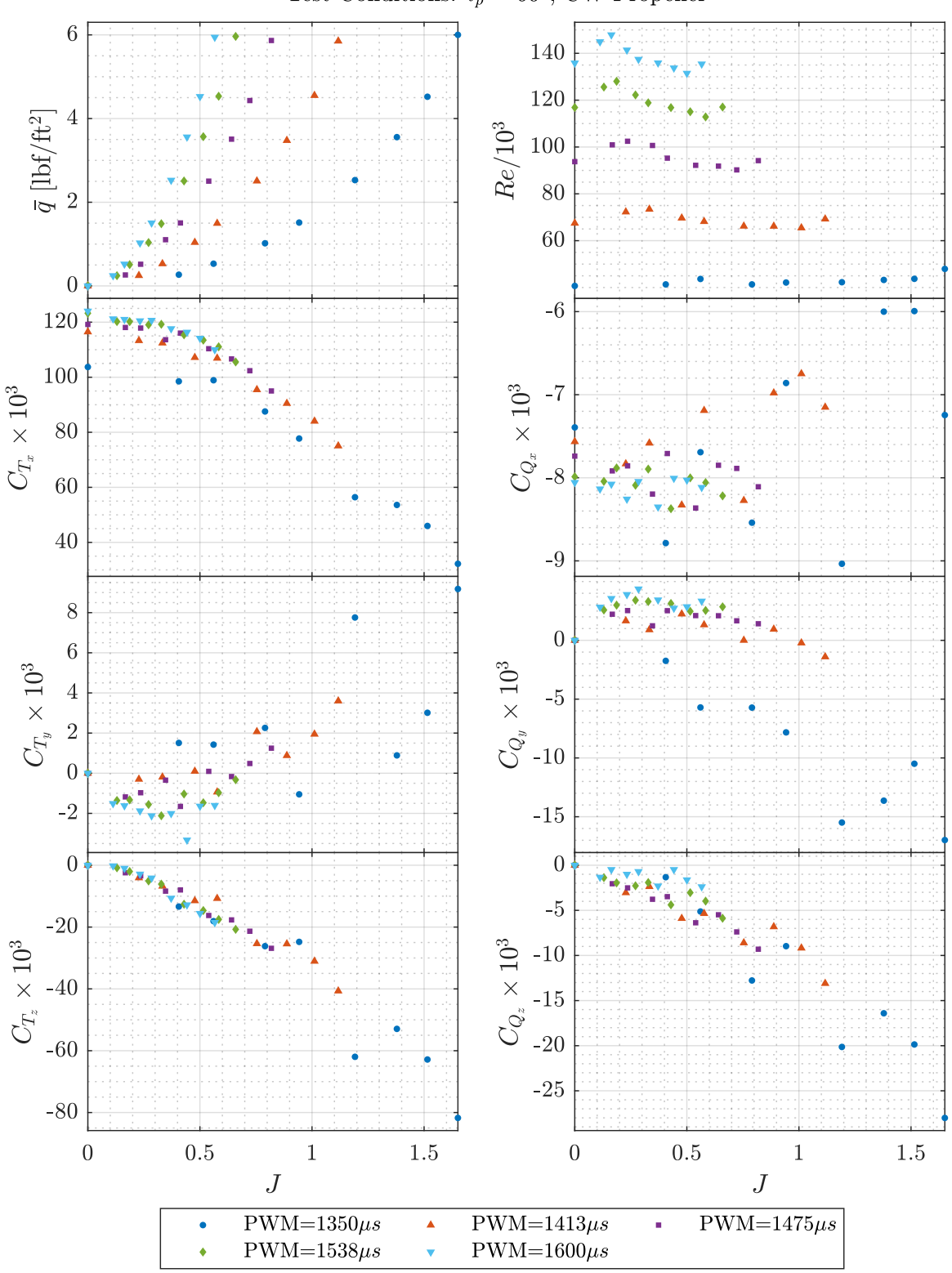

Figure 32. CW propeller force and moment coefficients variation with J at $i_p = 60°$.

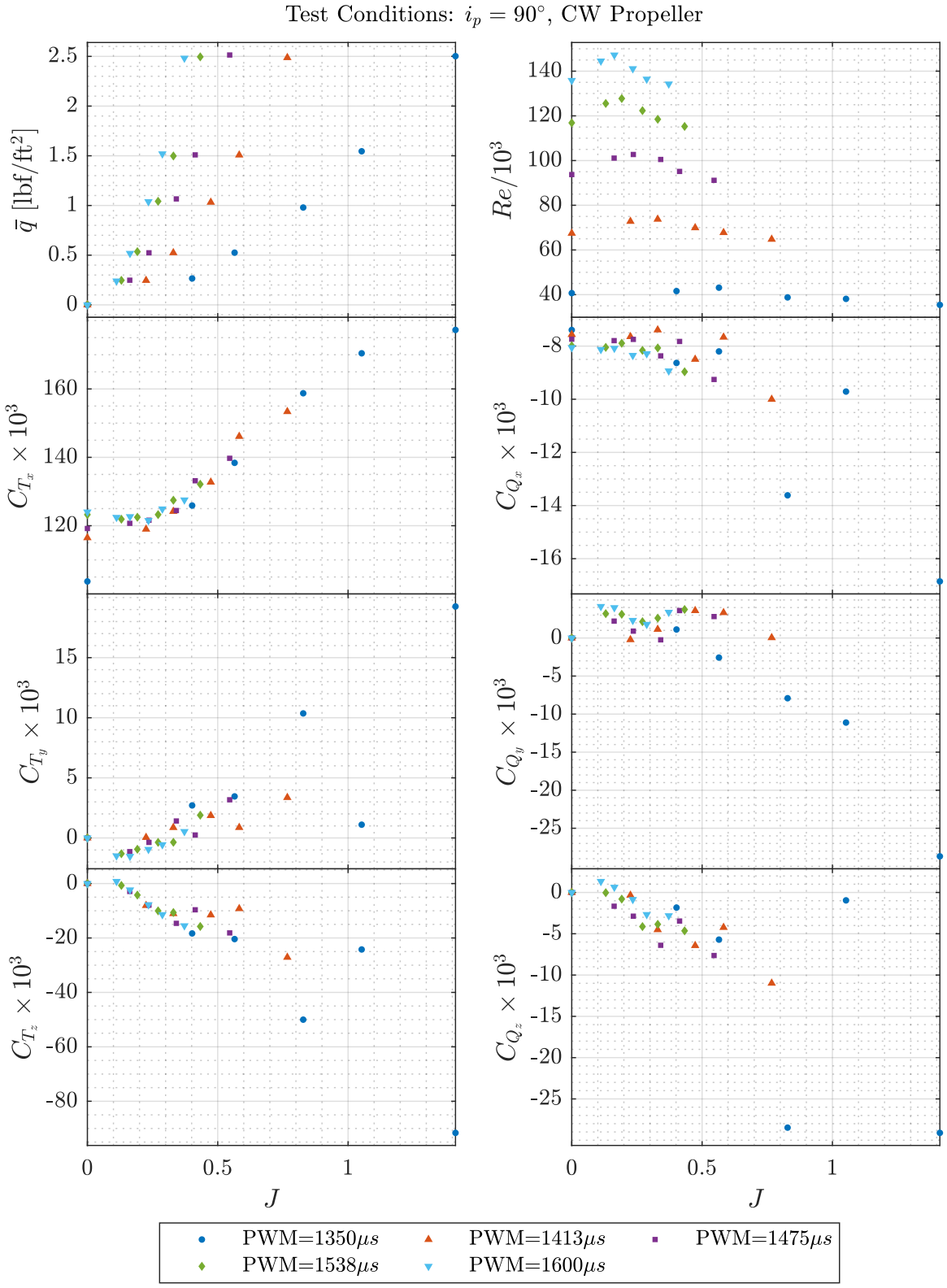

Figure 33. CW propeller force and moment coefficients variation with J at $i_p = 90°$.

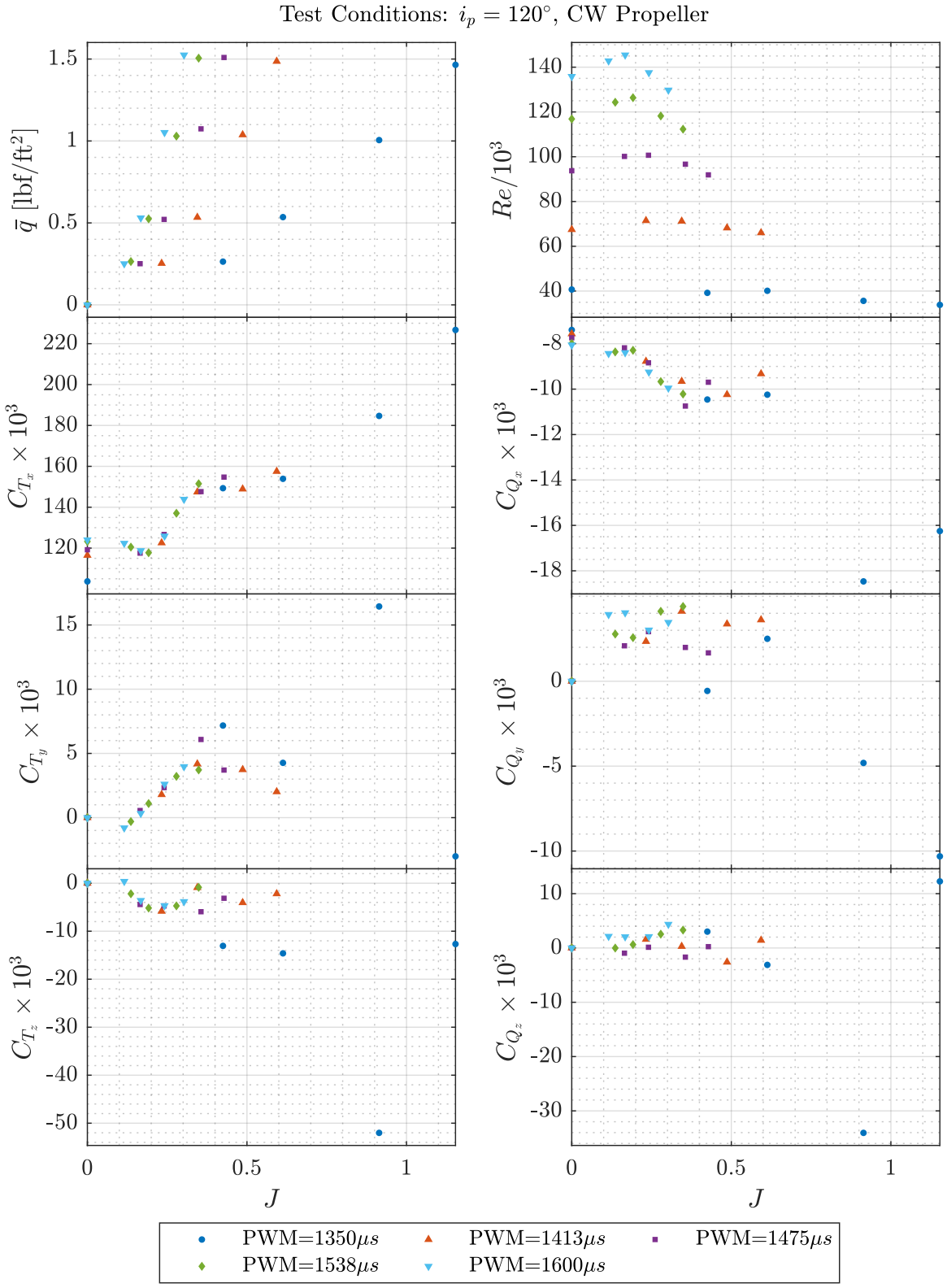

Figure 34. CW propeller force and moment coefficients variation with J at $i_p = 120°$.

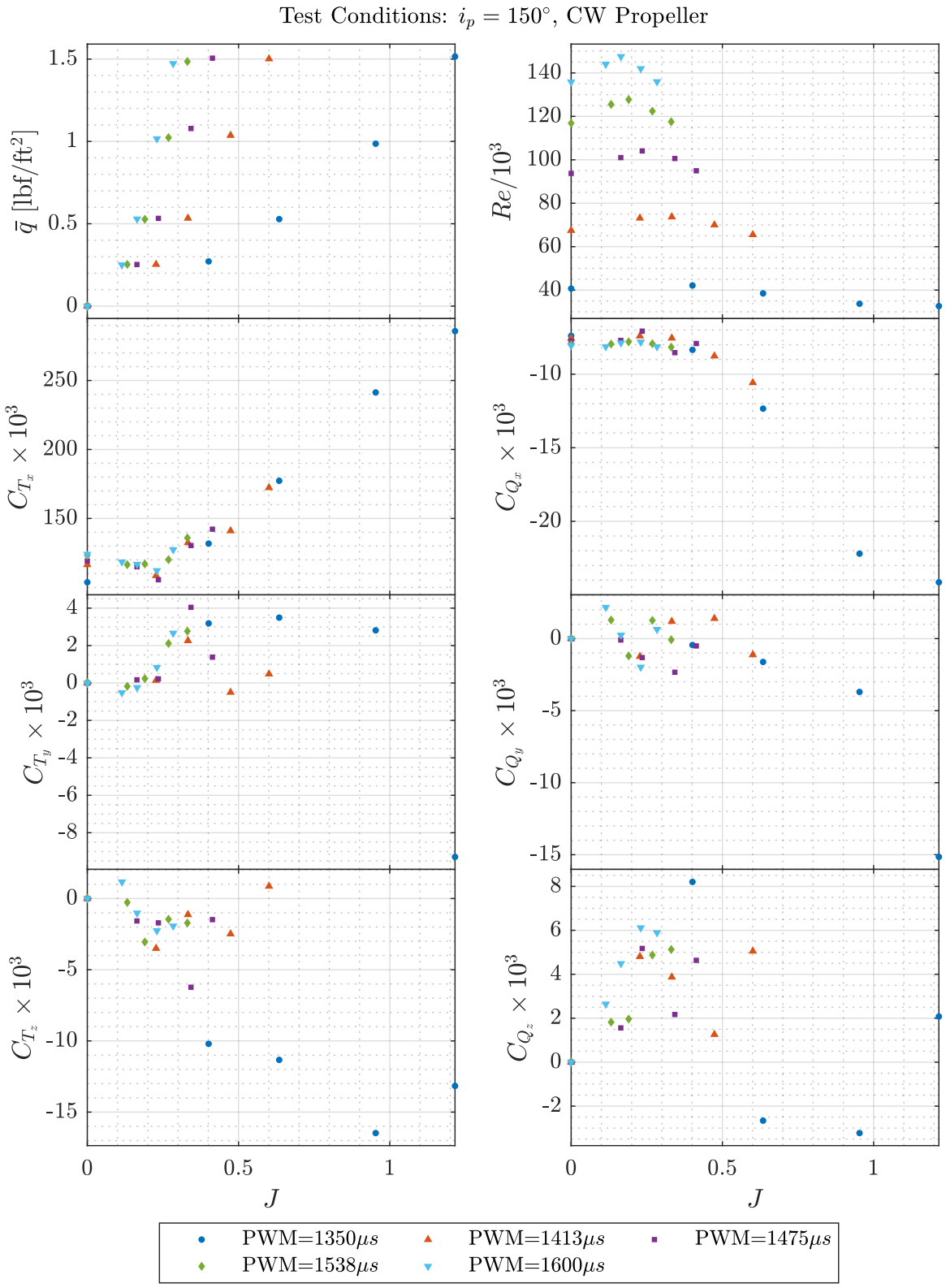

Figure 35. CW propeller force and moment coefficients variation with J at $i_p = 150°$.

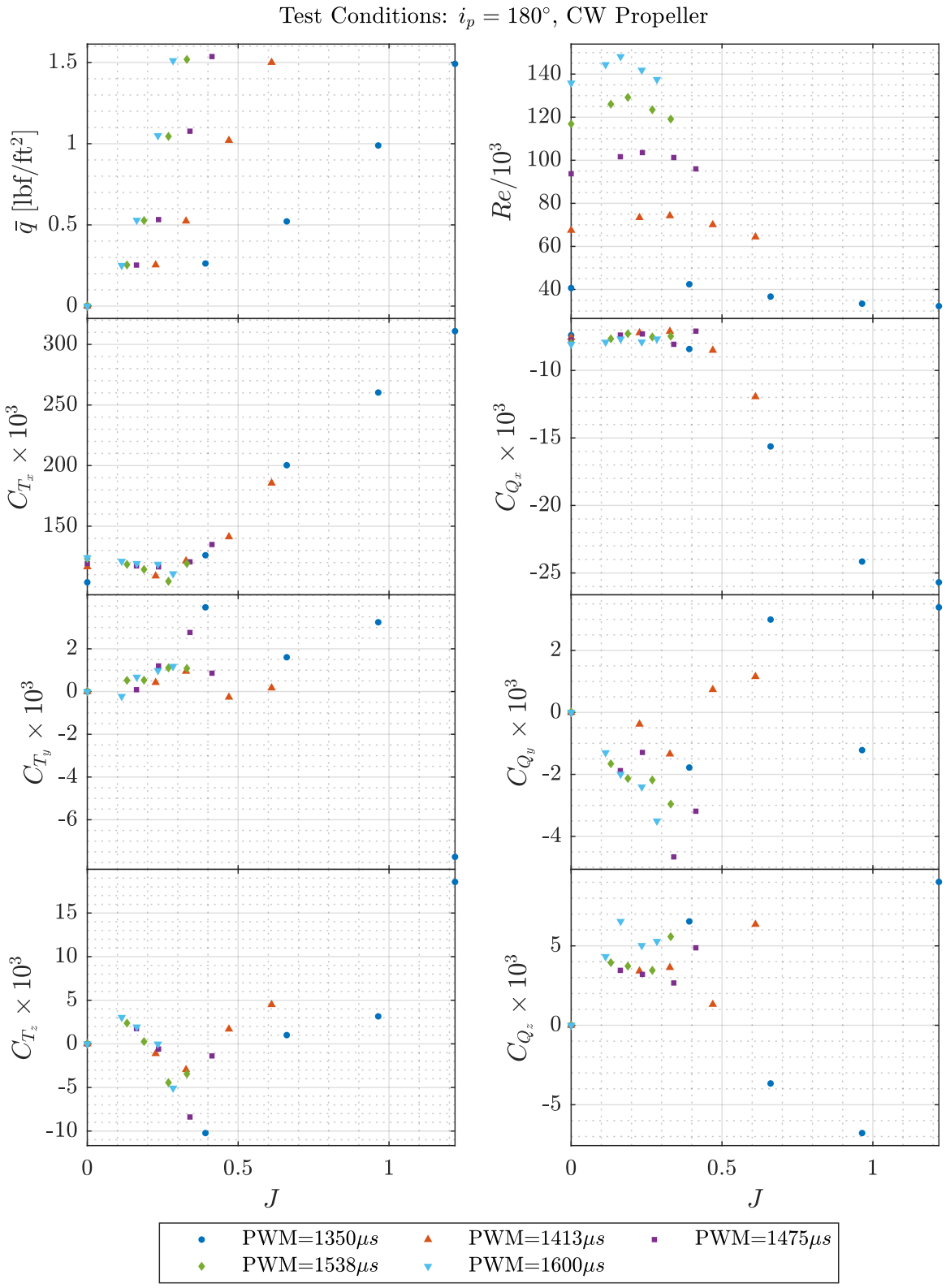

Figure 36. CW propeller force and moment coefficients variation with J at $i_p = 180°$.

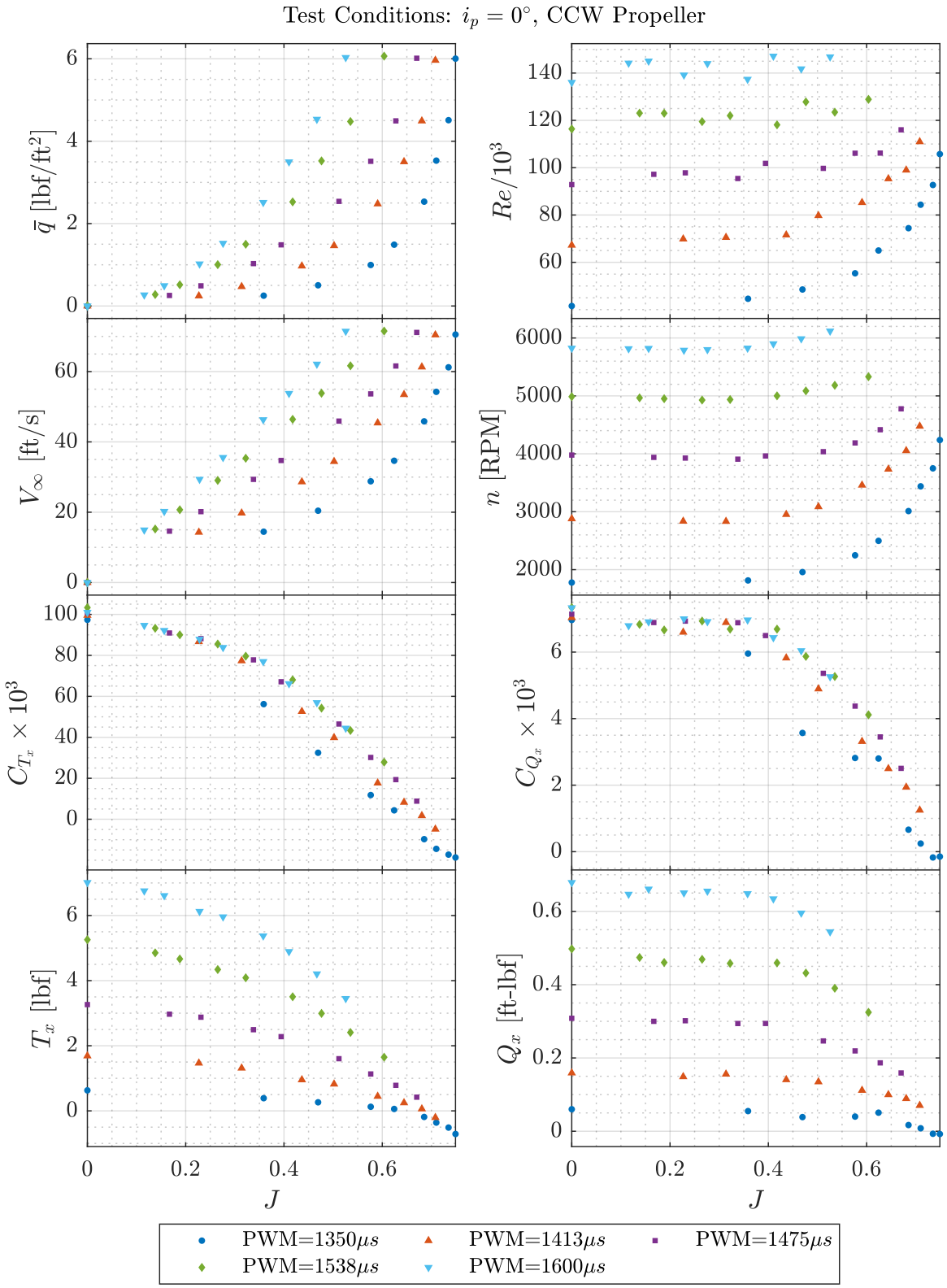

Figure 37. CCW propeller thrust, thrust coefficient, torque, and torque coefficient variation with J at $i_p = 0°$.

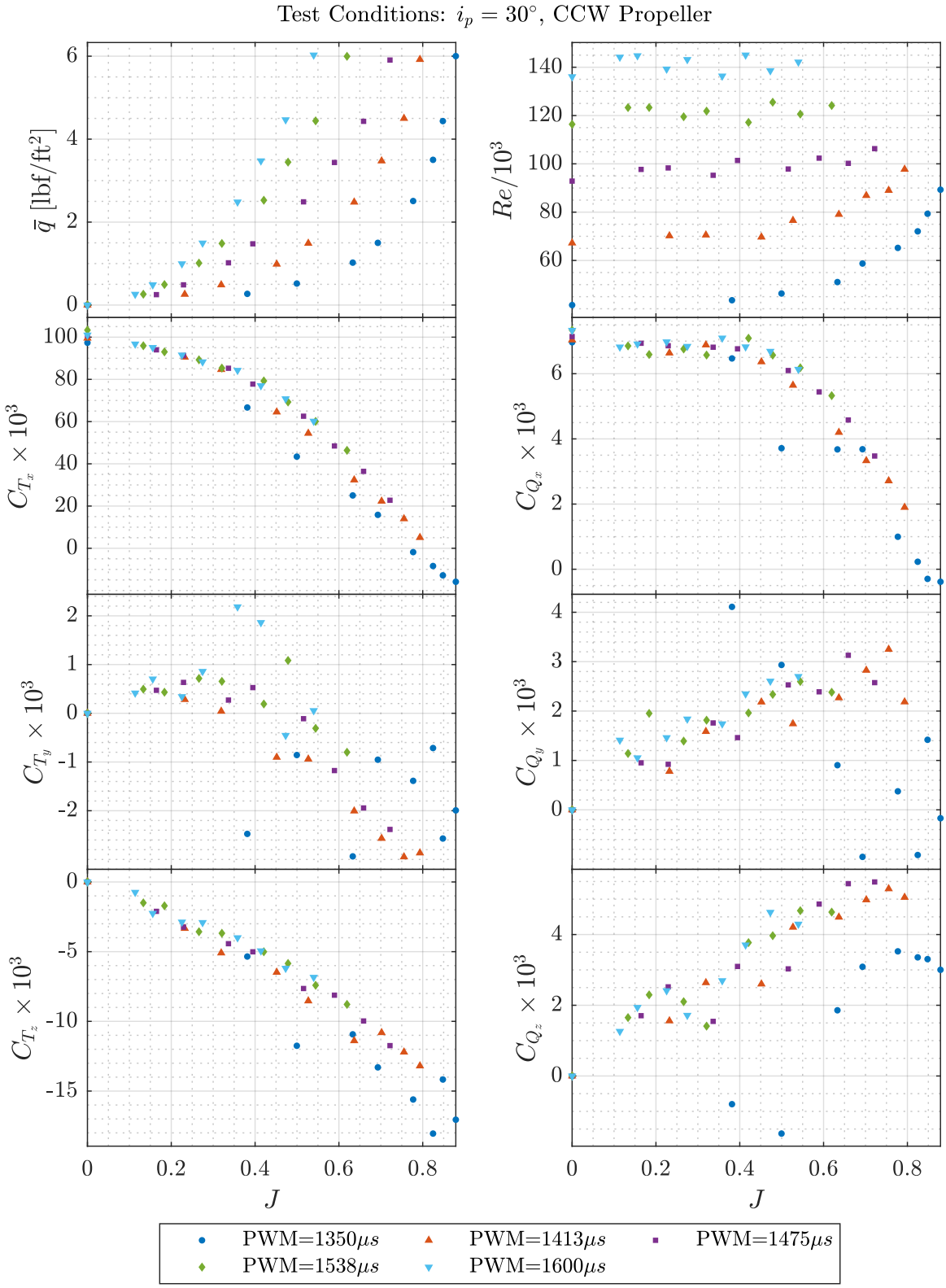

Figure 38. CCW propeller force and moment coefficients variation with J at $i_p = 30°$.

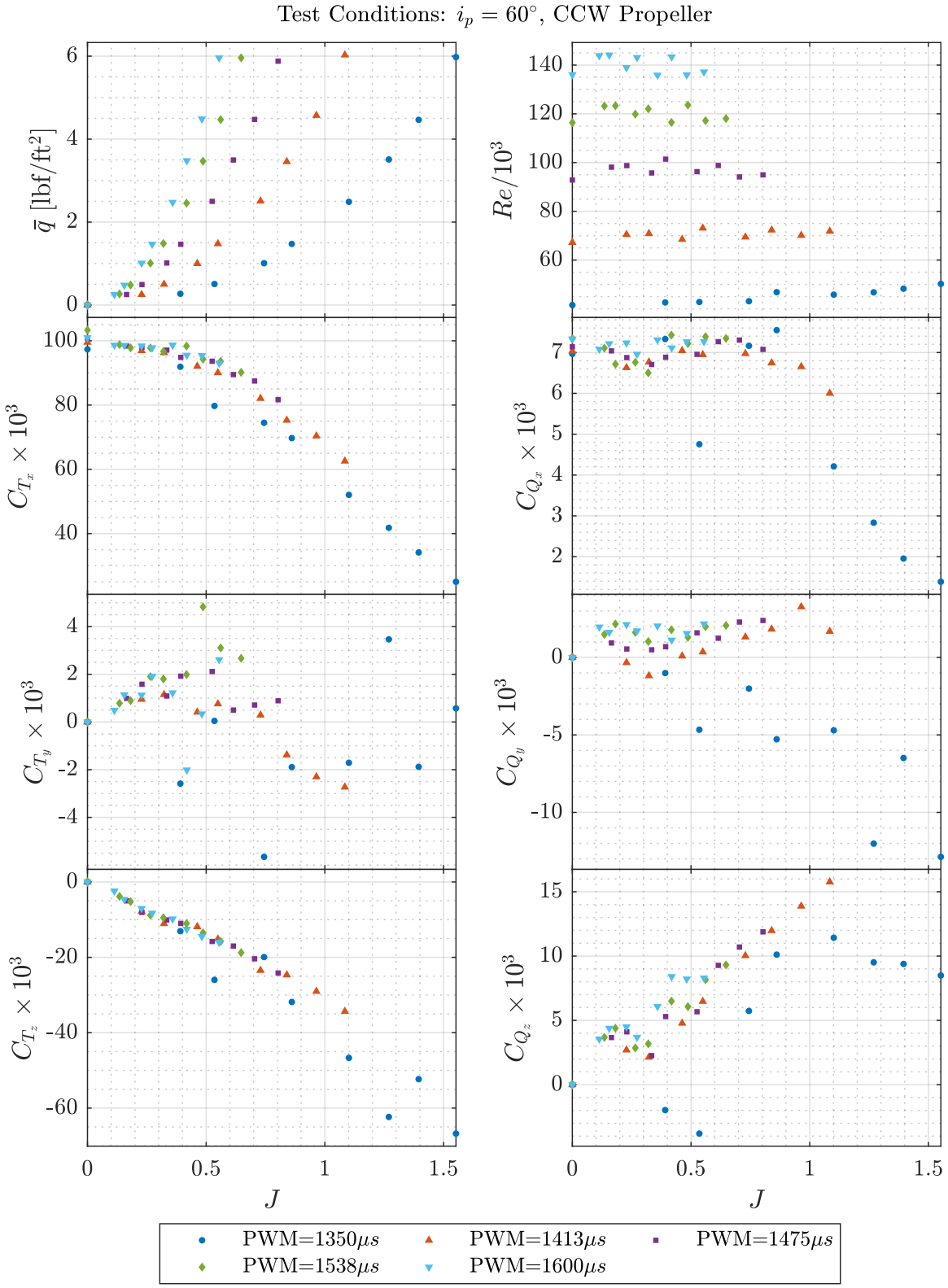

Figure 39. CCW propeller force and moment coefficients variation with J at $i_p = 60°$.

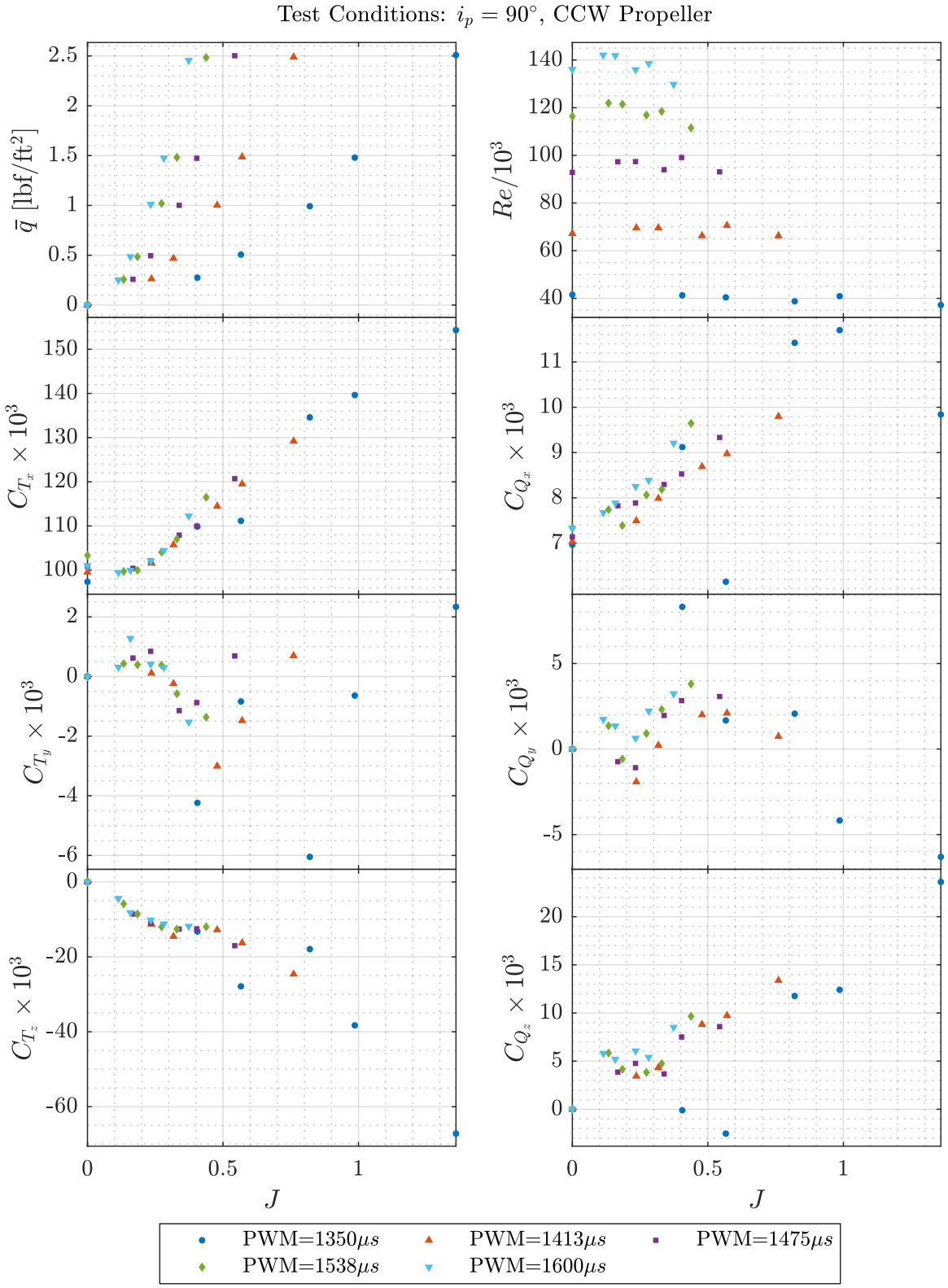

Figure 40. CCW propeller force and moment coefficients variation with J at $i_p = 90°$.

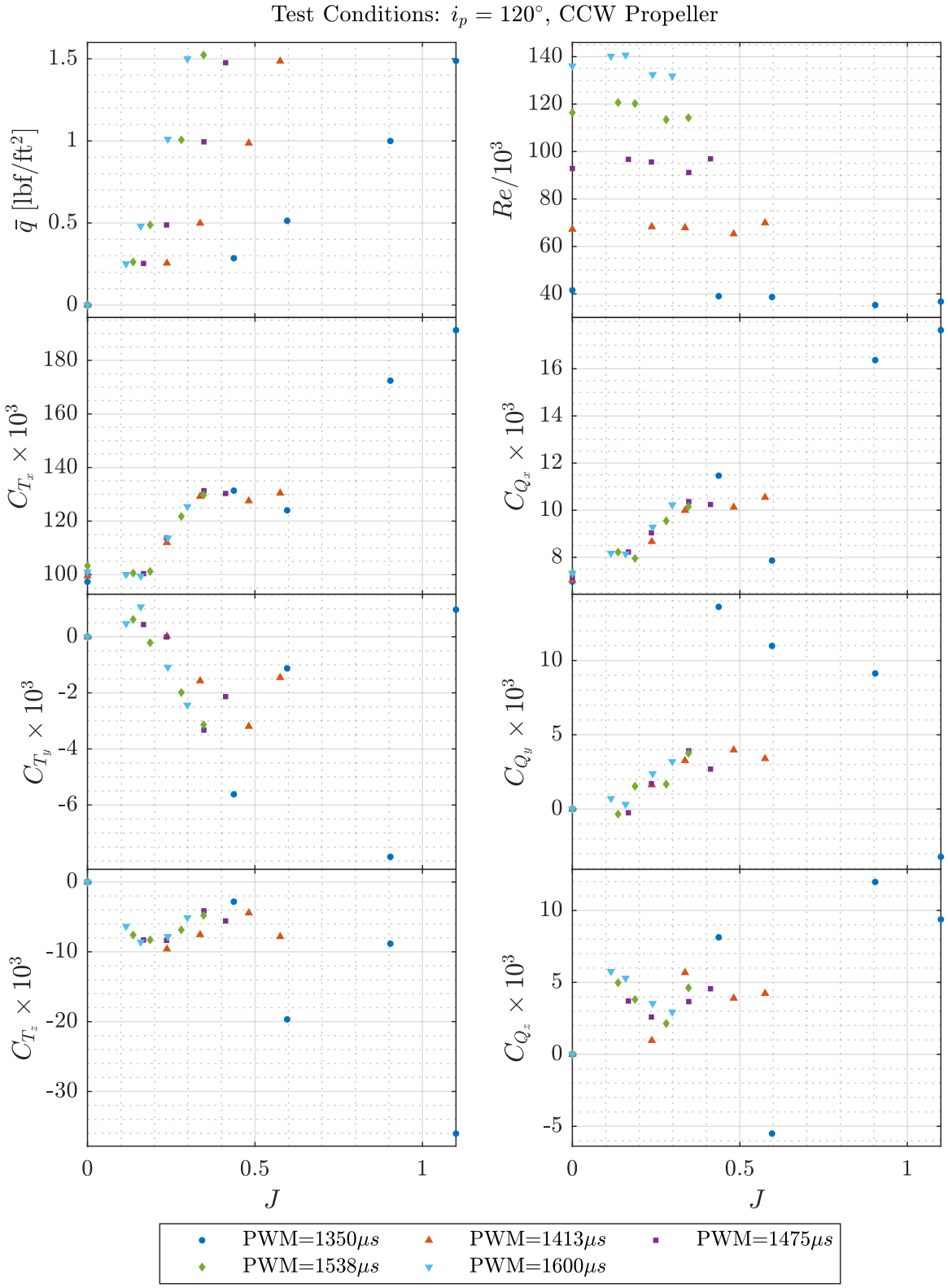

Figure 41. CCW propeller force and moment coefficients variation with J at $i_p = 120°$.

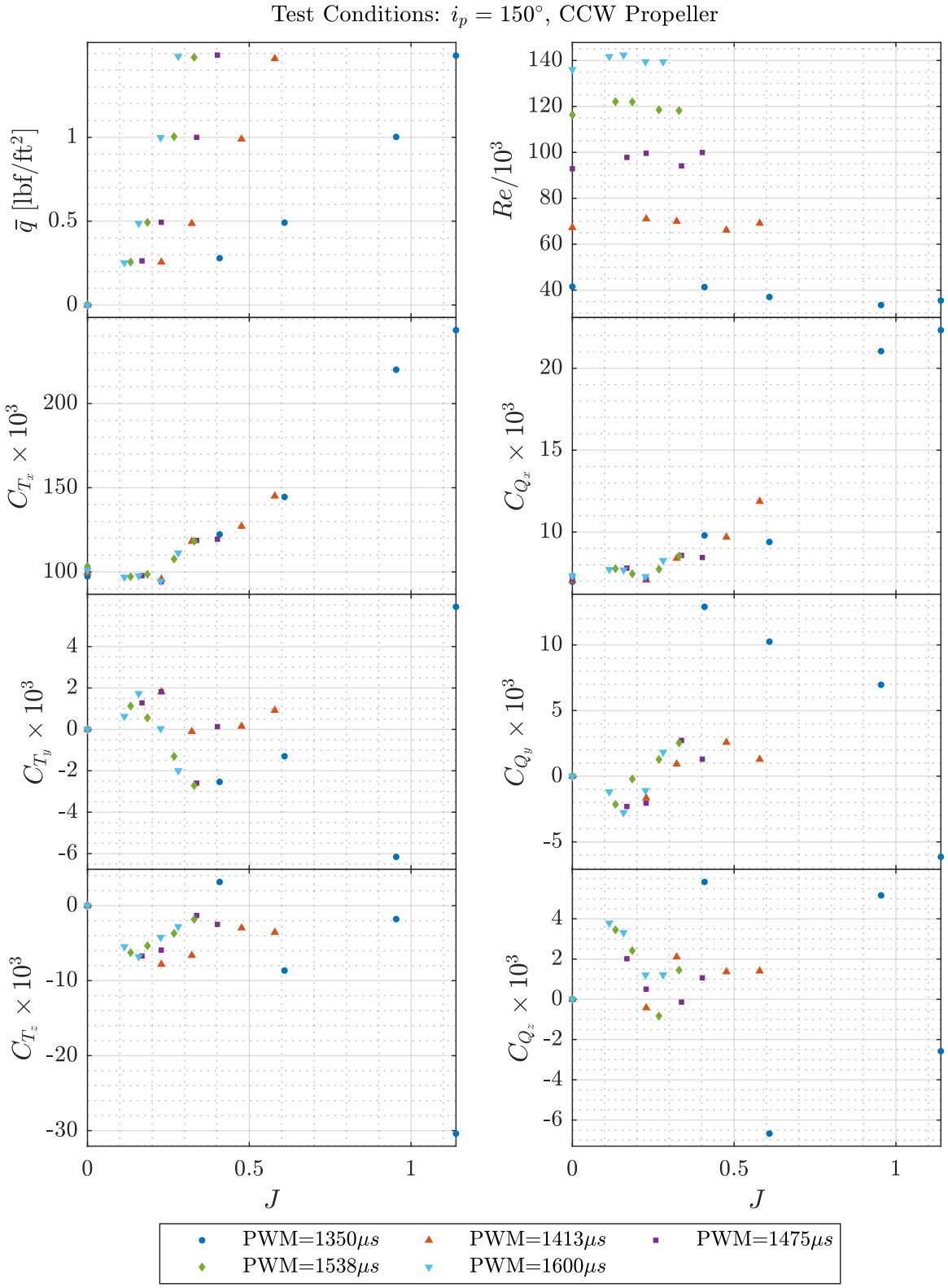

Figure 42. CCW propeller force and moment coefficients variation with J at $i_p = 150°$.

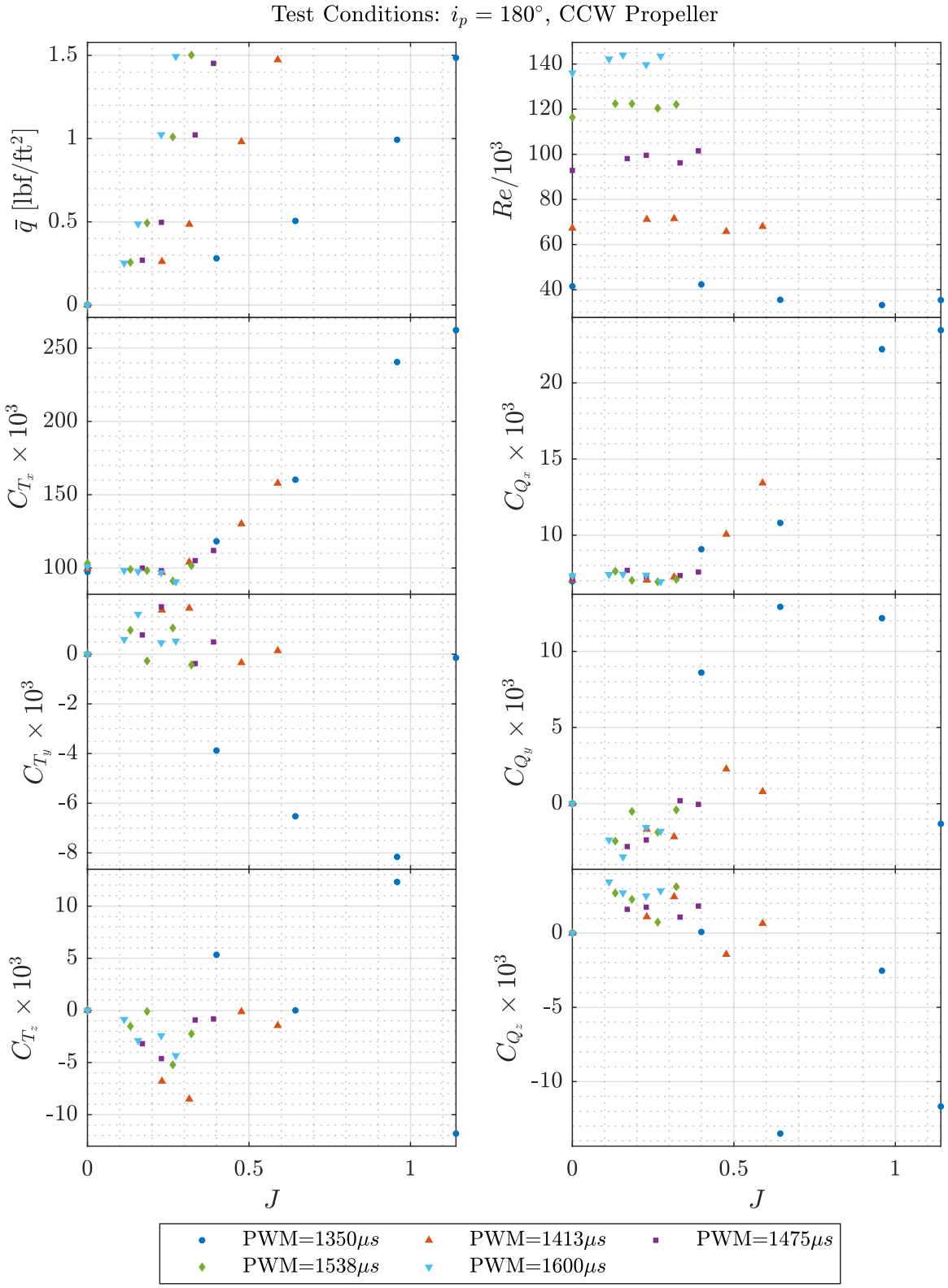

Figure 43. CCW propeller force and moment coefficients variation with J at $i_p = 180°$.

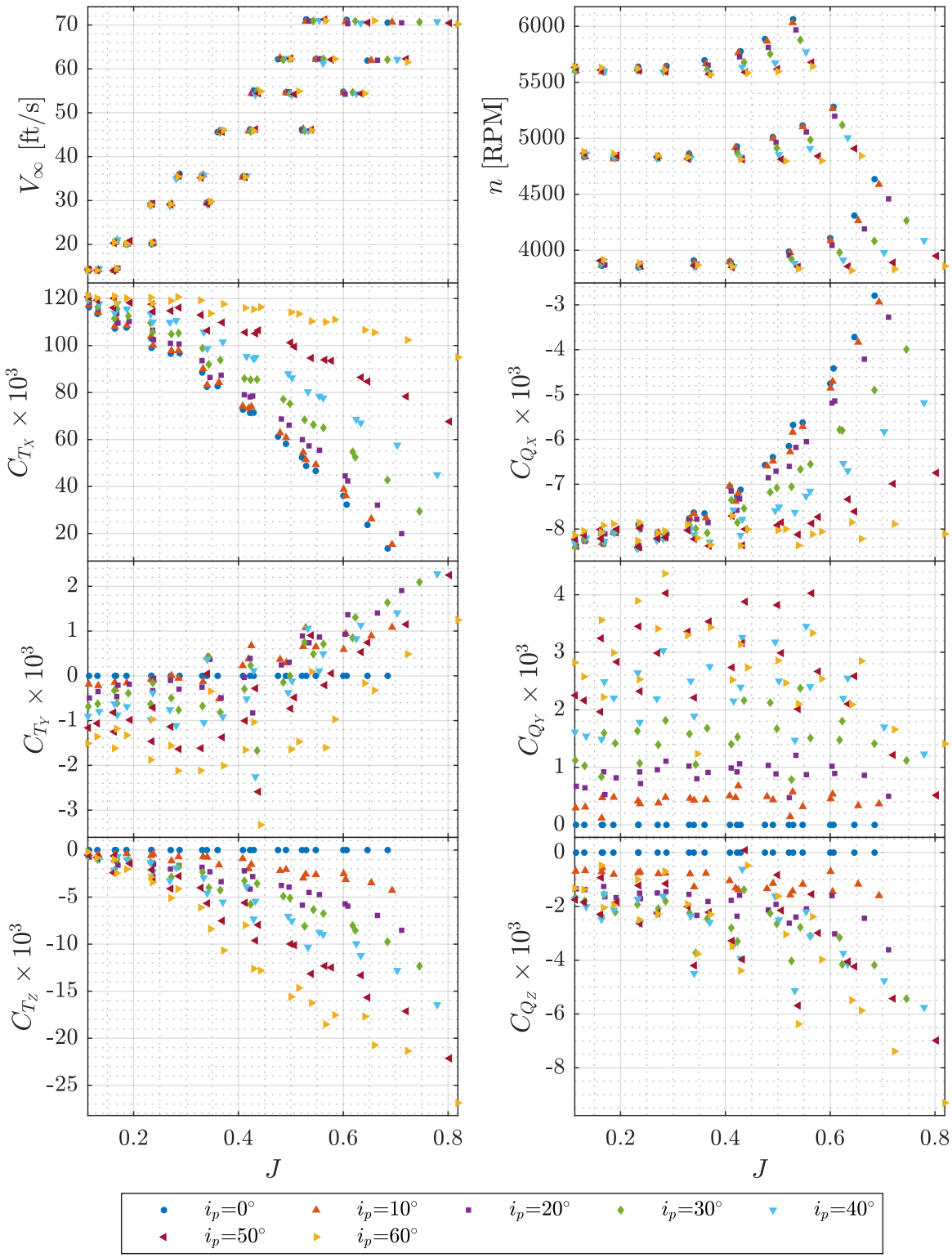

Figure 44. CW propeller force and moment coefficients variation with J for $0^\circ \leq i_p \leq 60^\circ$.

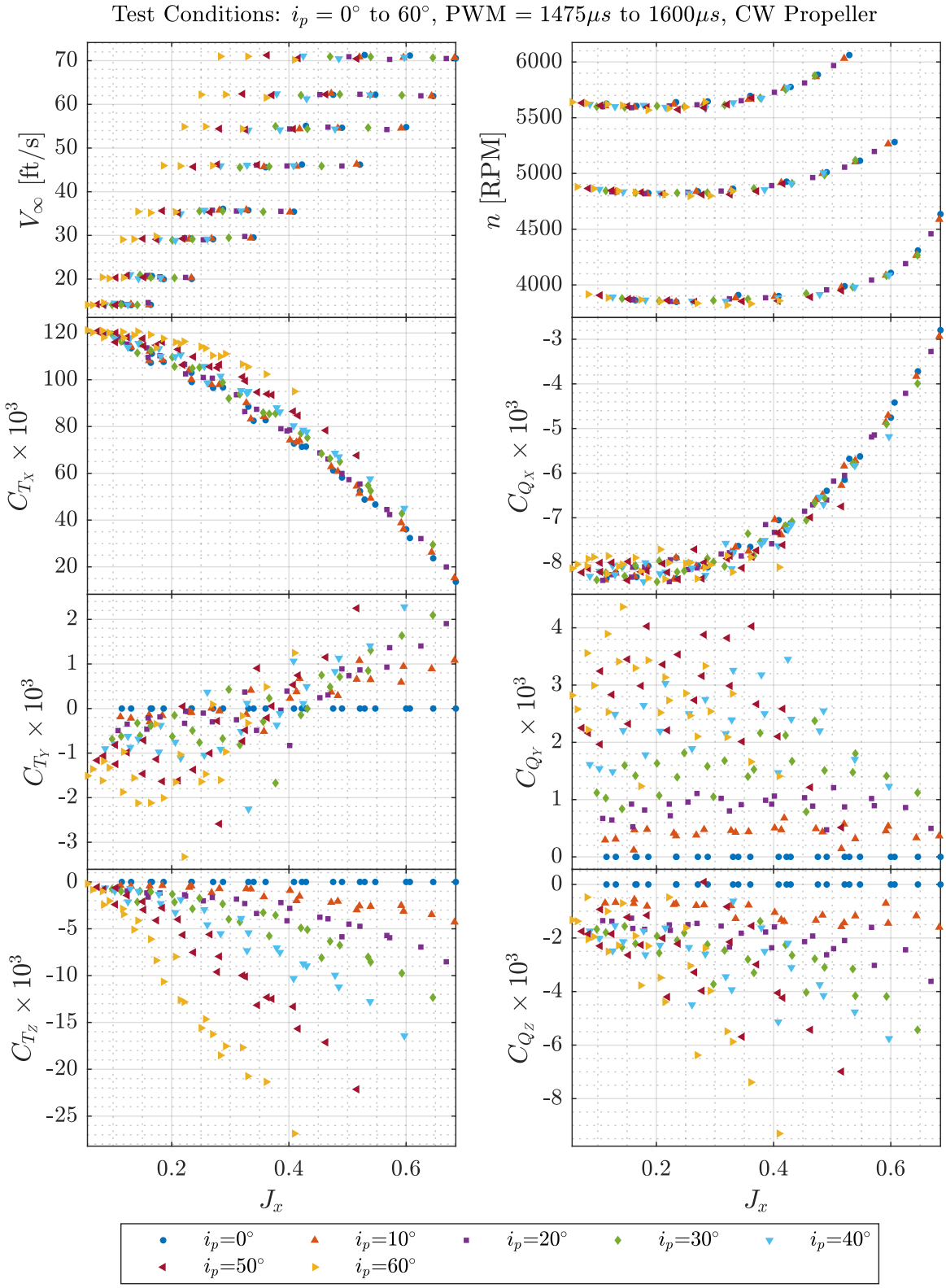

Figure 45. CW propeller force and moment coefficients variation with J_x for $0^\circ \leq i_p \leq 60^\circ$.

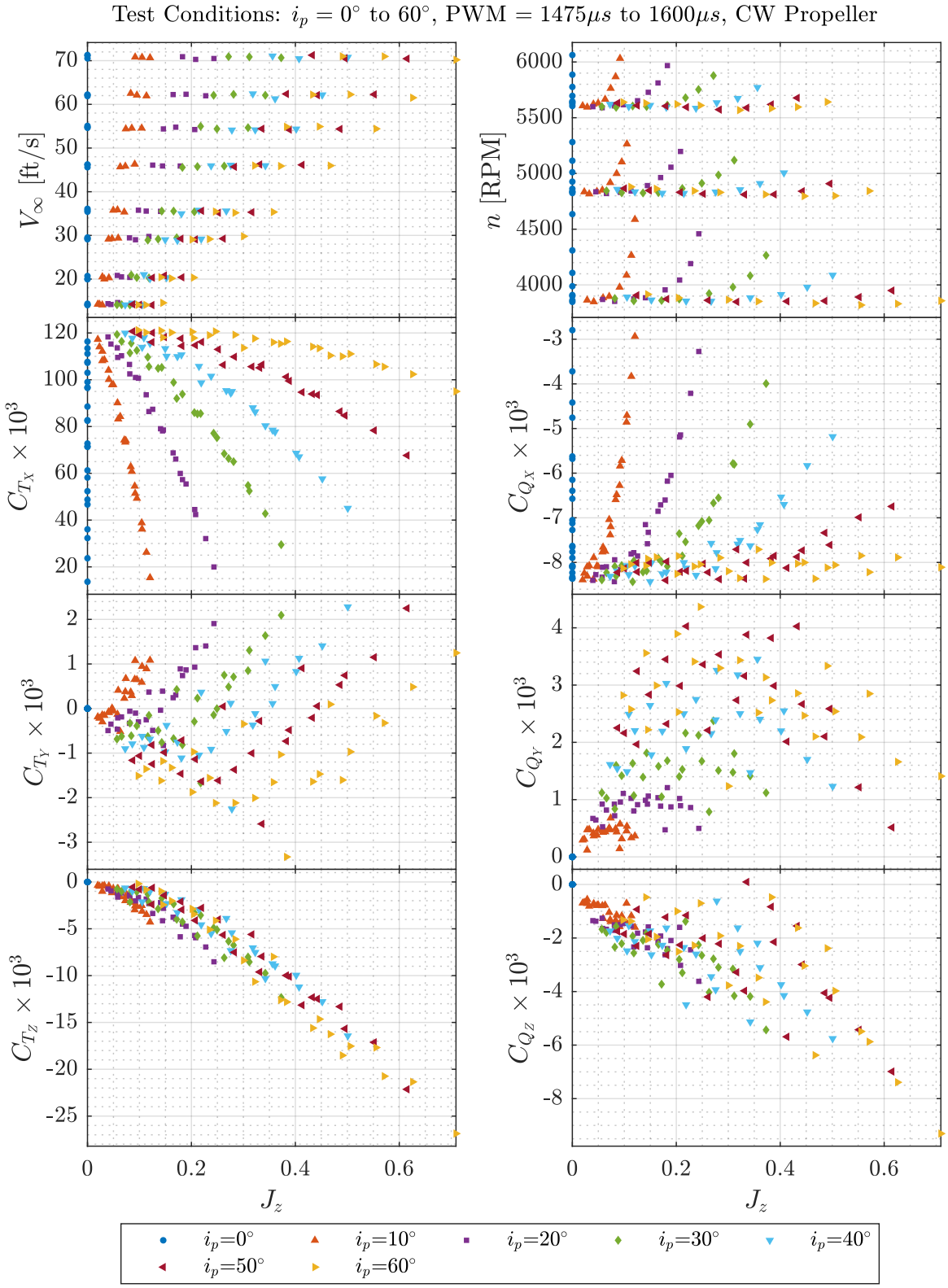

Figure 46. CW propeller force and moment coefficients variation with J_z for $0^\circ \leq i_p \leq 60^\circ$.

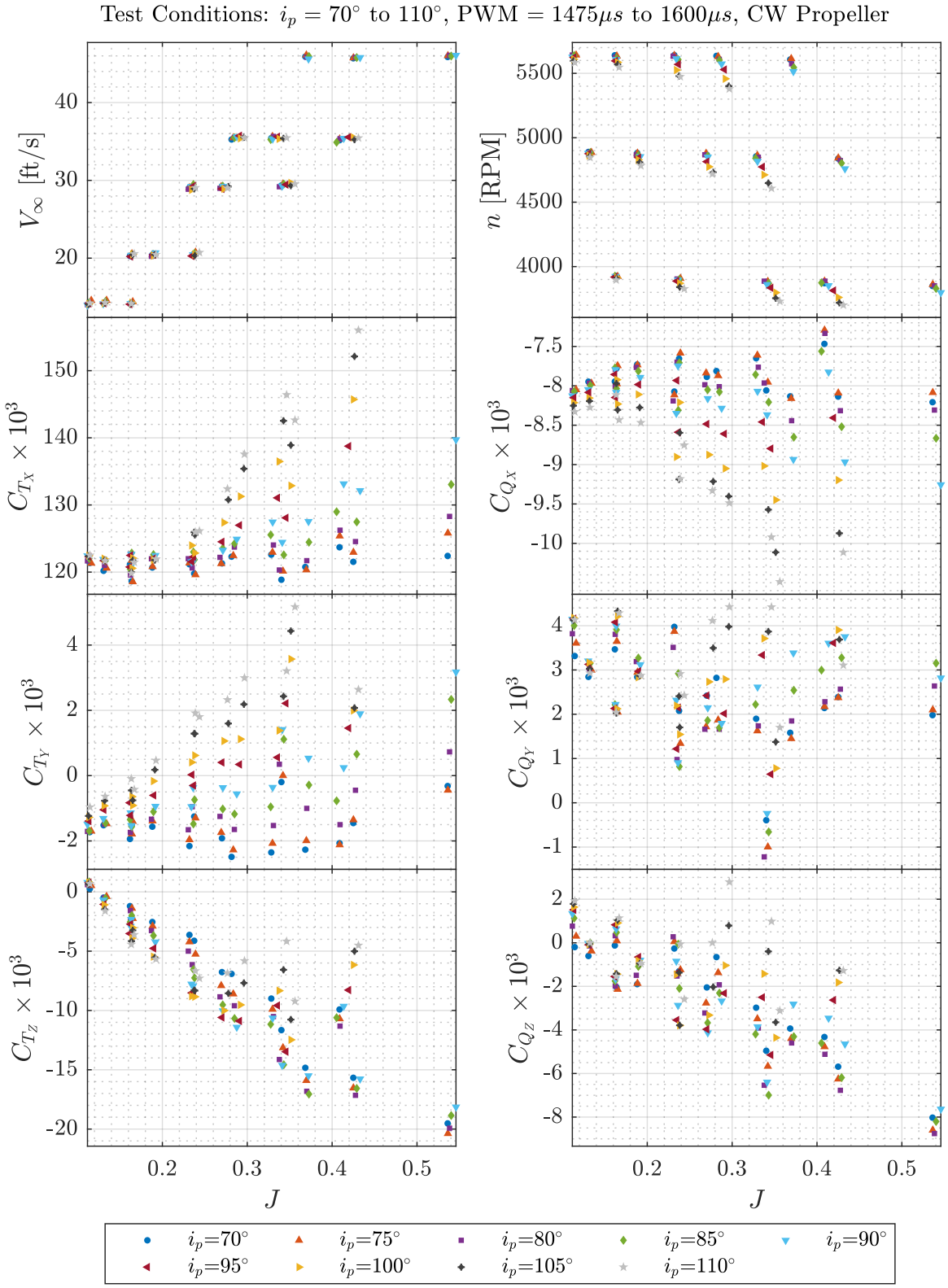

Figure 47. CW propeller force and moment coefficients variation with J for $70^\circ \leq i_p \leq 110^\circ$.

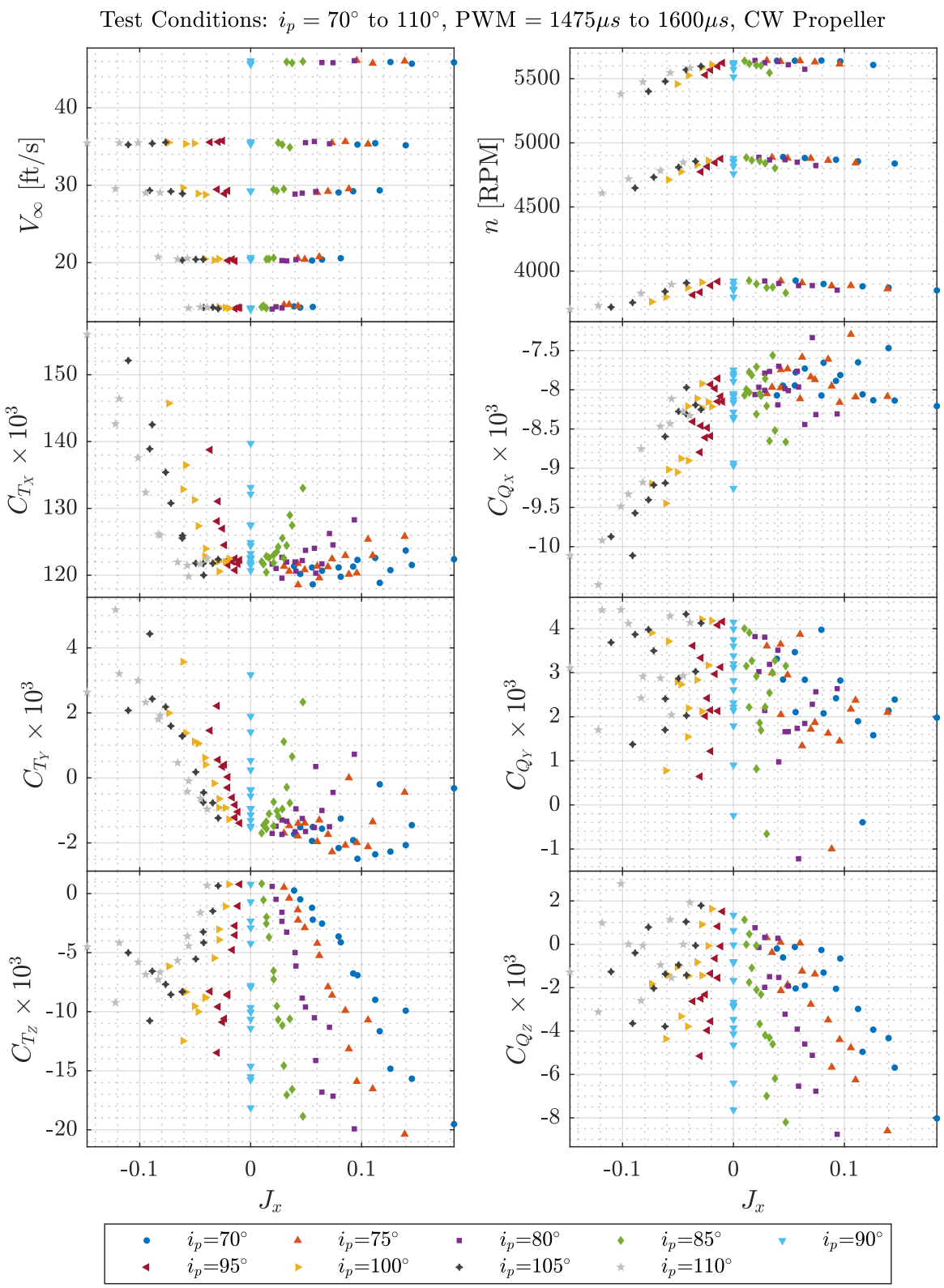

Figure 48. CW propeller force and moment coefficients variation with J_x for $70^\circ \leq i_p \leq 110^\circ$.

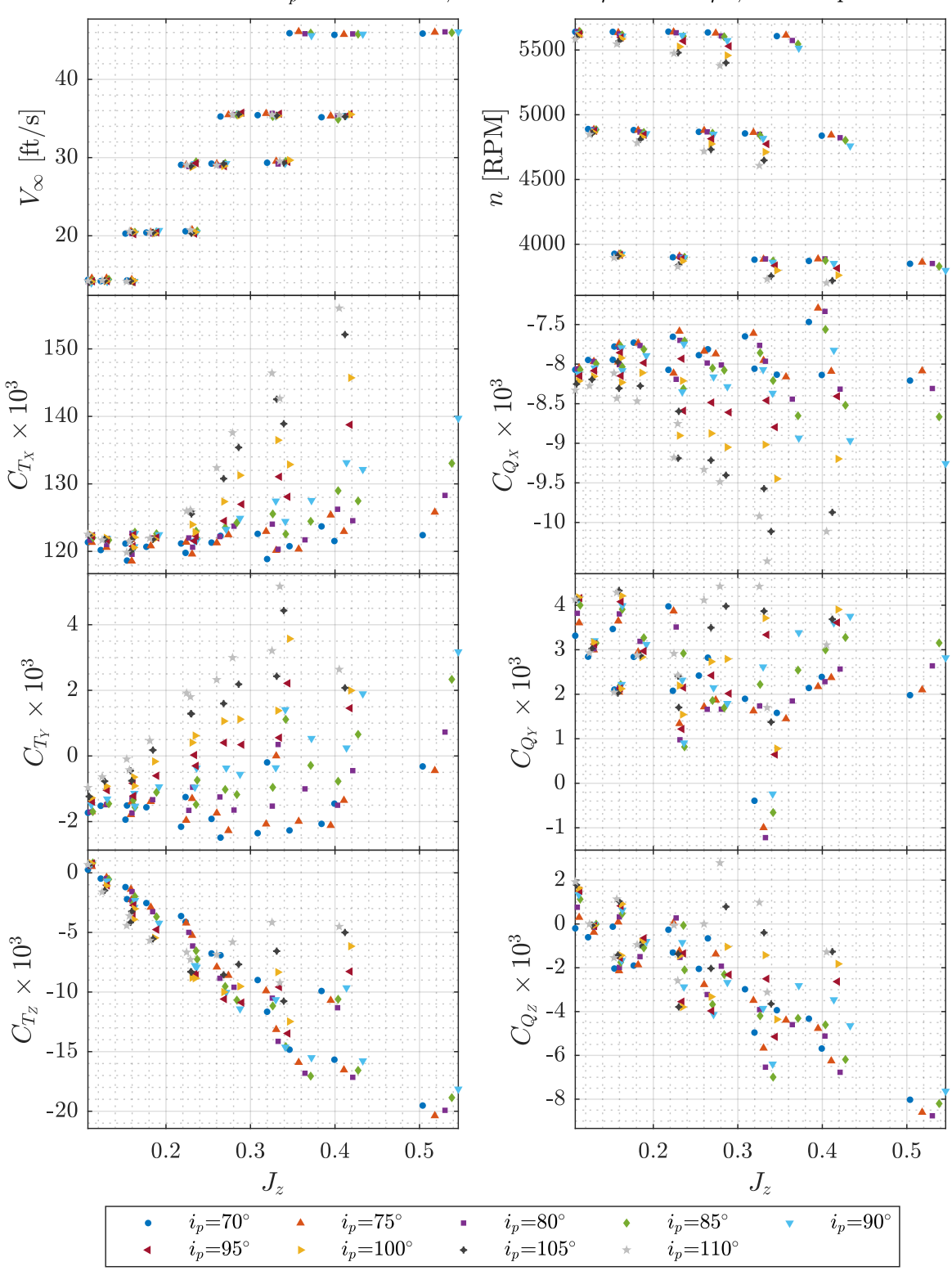

Figure 49. CW propeller force and moment coefficients variation with J_z for $70^\circ \leq i_p \leq 110^\circ$.

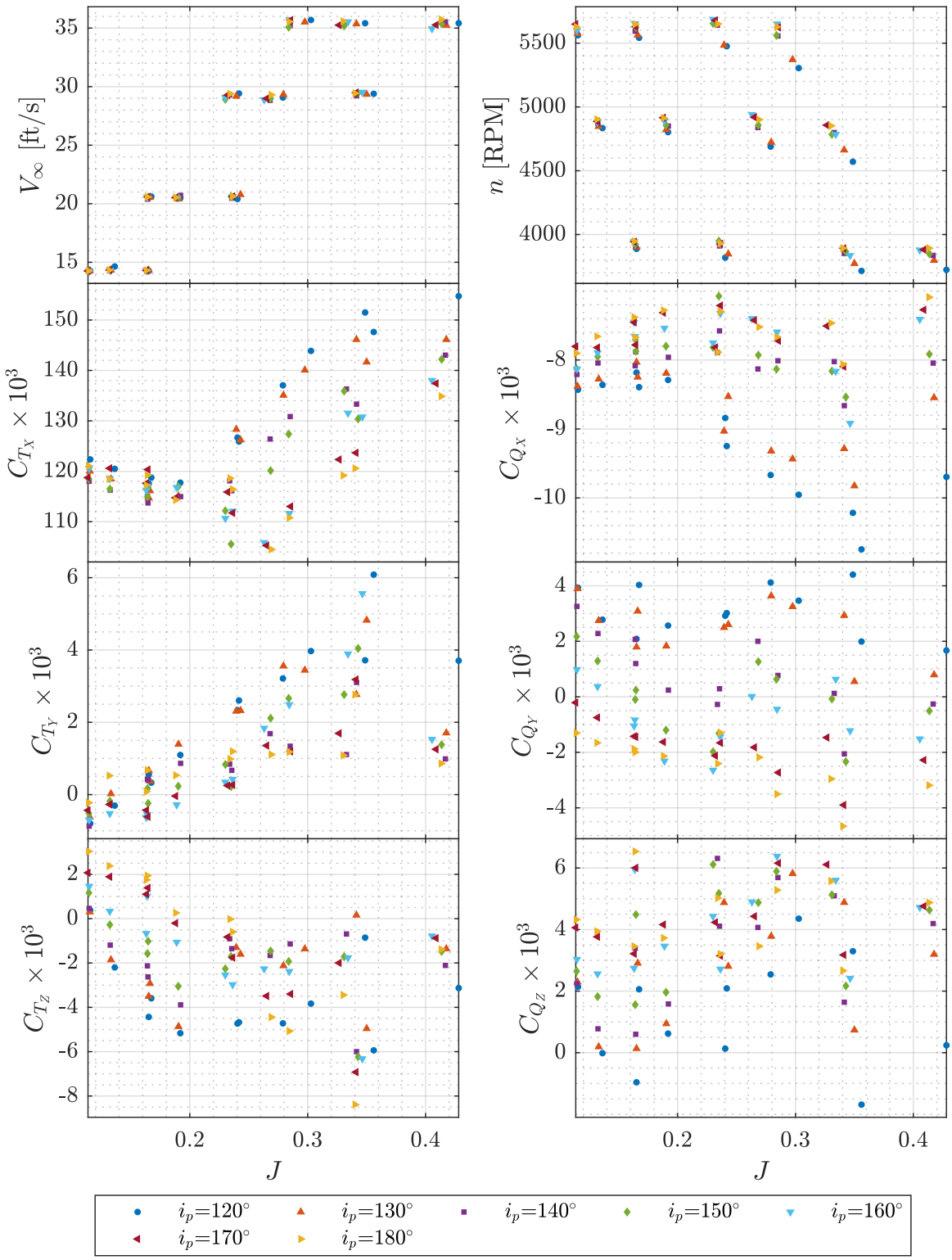

Figure 50. CW propeller force and moment coefficients variation with J for $120^\circ \leq i_p \leq 180^\circ$.

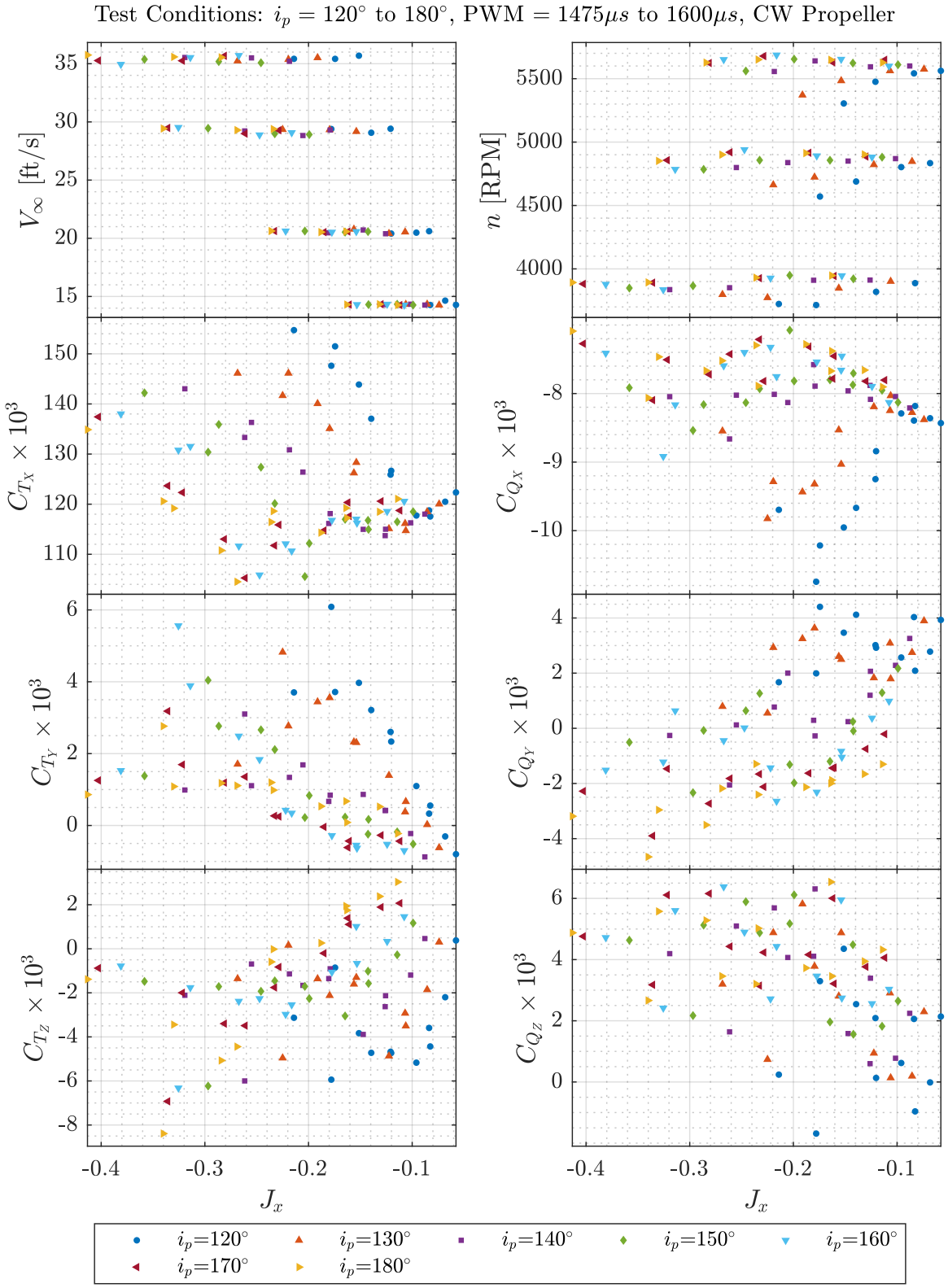

Figure 51. CW propeller force and moment coefficients variation with J_x for $120^\circ \leq i_p \leq 180^\circ$.

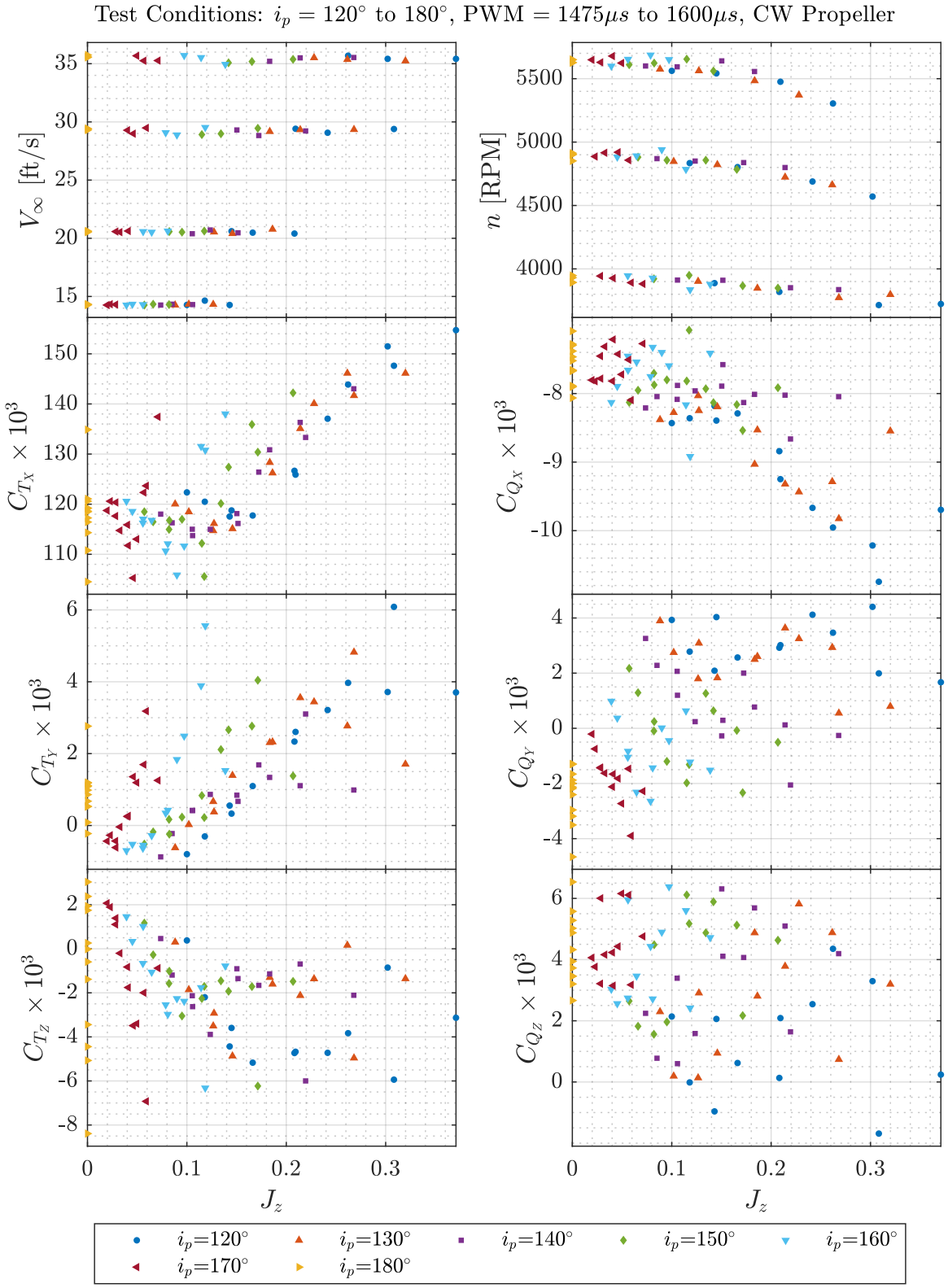

Figure 52. CW propeller force and moment coefficients variation with J_z for $120^\circ \leq i_p \leq 180^\circ$.

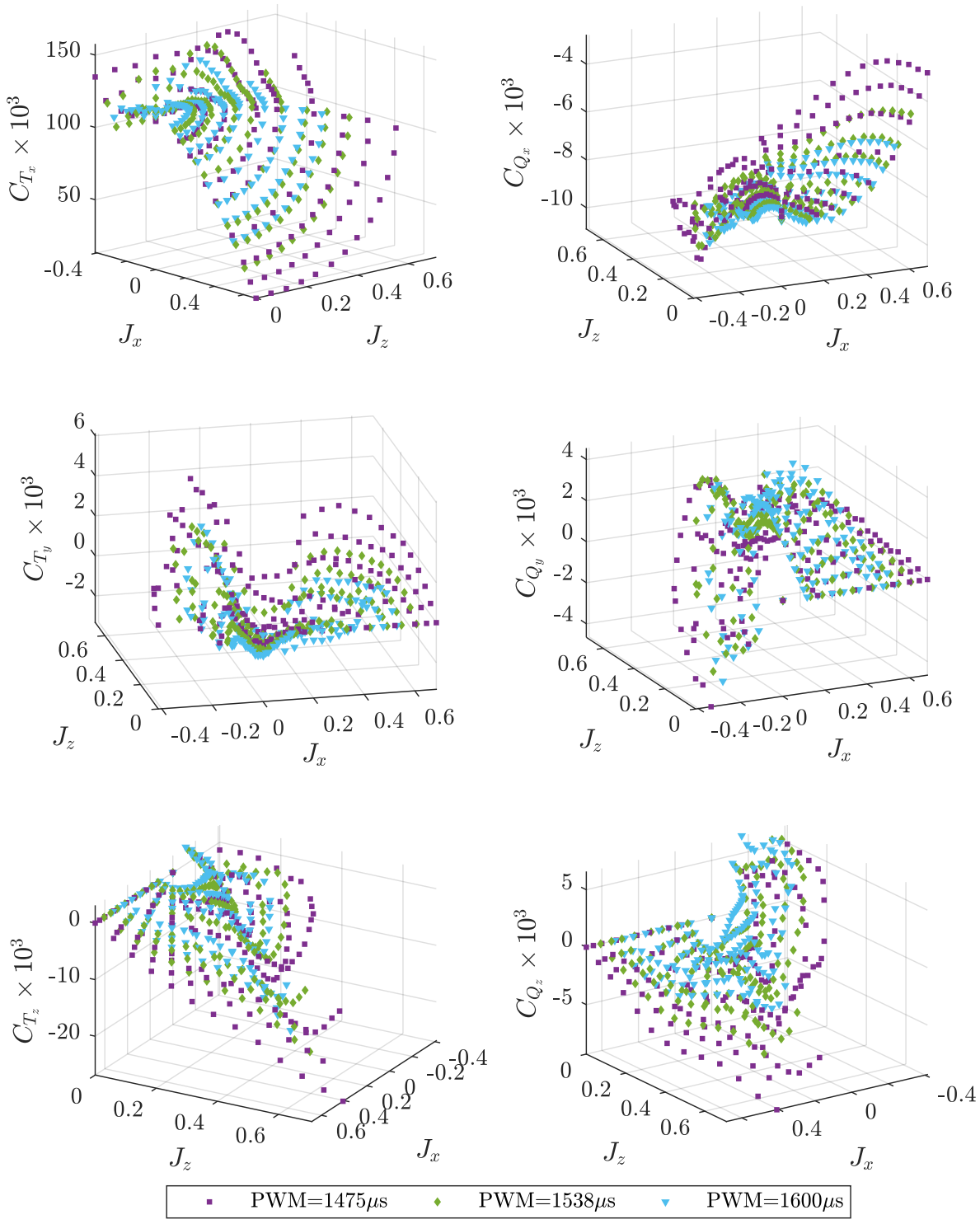

Figure 53. CW propeller force and moment coefficients variation with J_x and J_z.

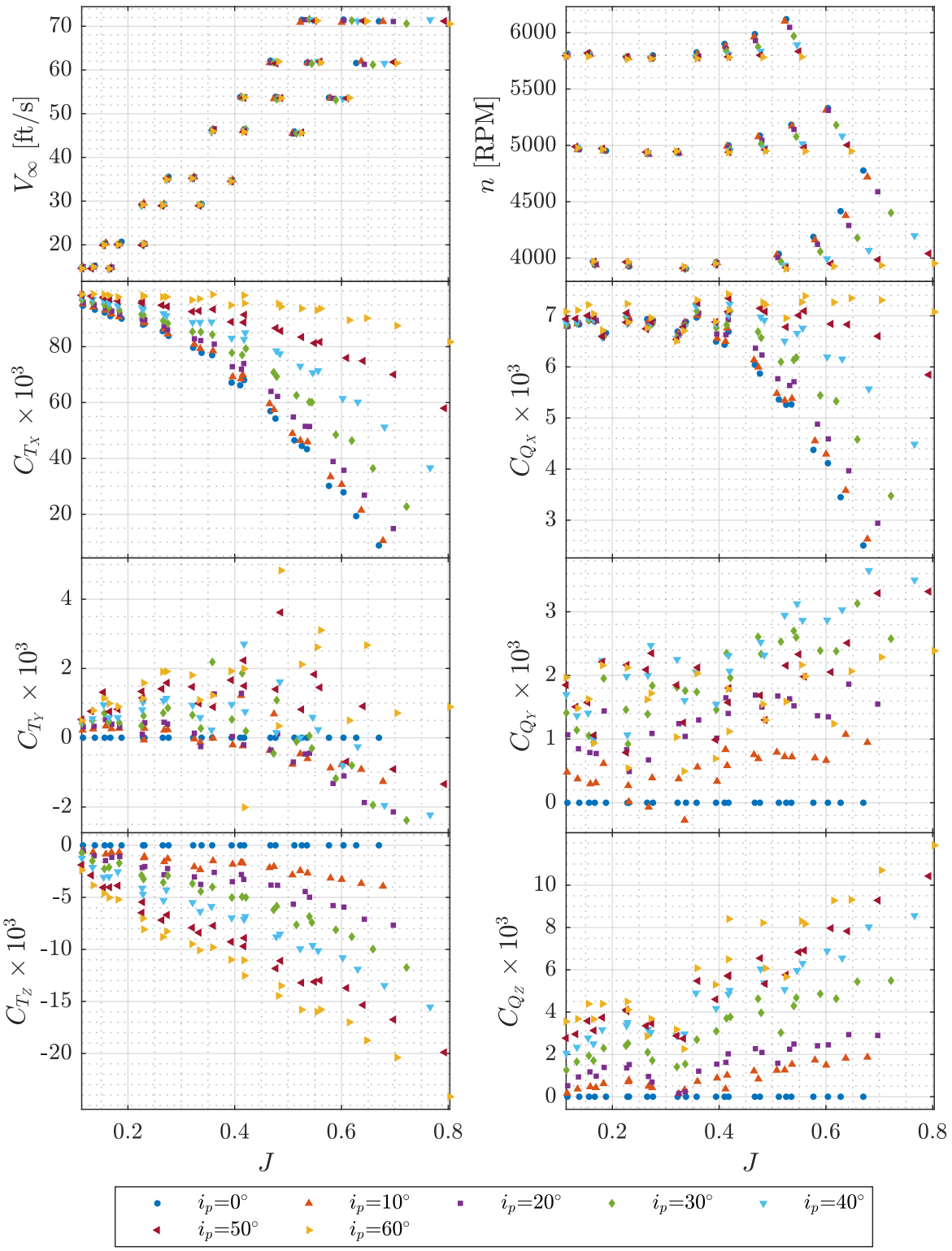

Figure 54. CCW propeller force and moment coefficients variation with J for $0^\circ \leq i_p \leq 60^\circ$.

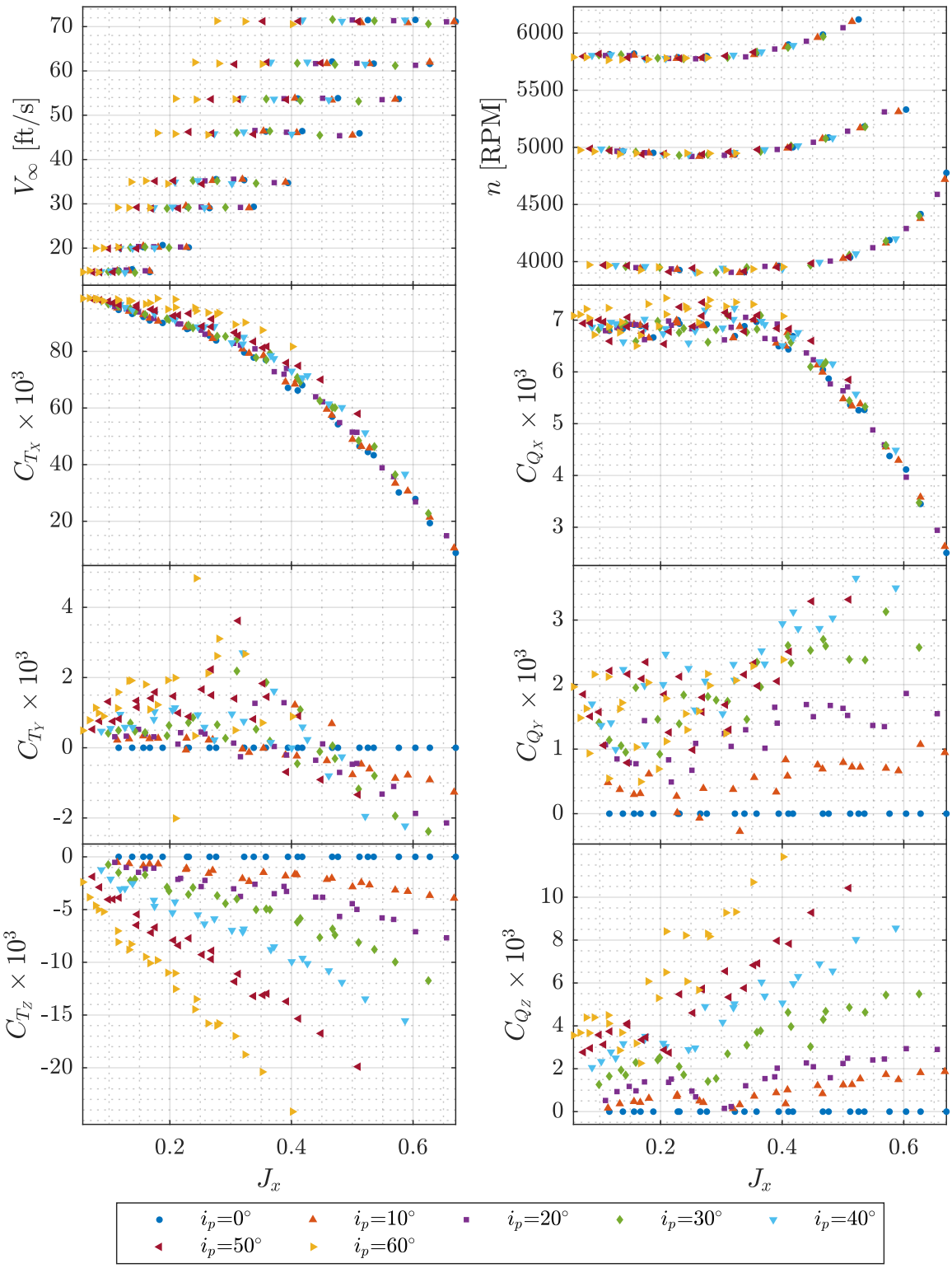

Figure 55. CCW propeller force and moment coefficients variation with J_x for $0^\circ \leq i_p \leq 60^\circ$.

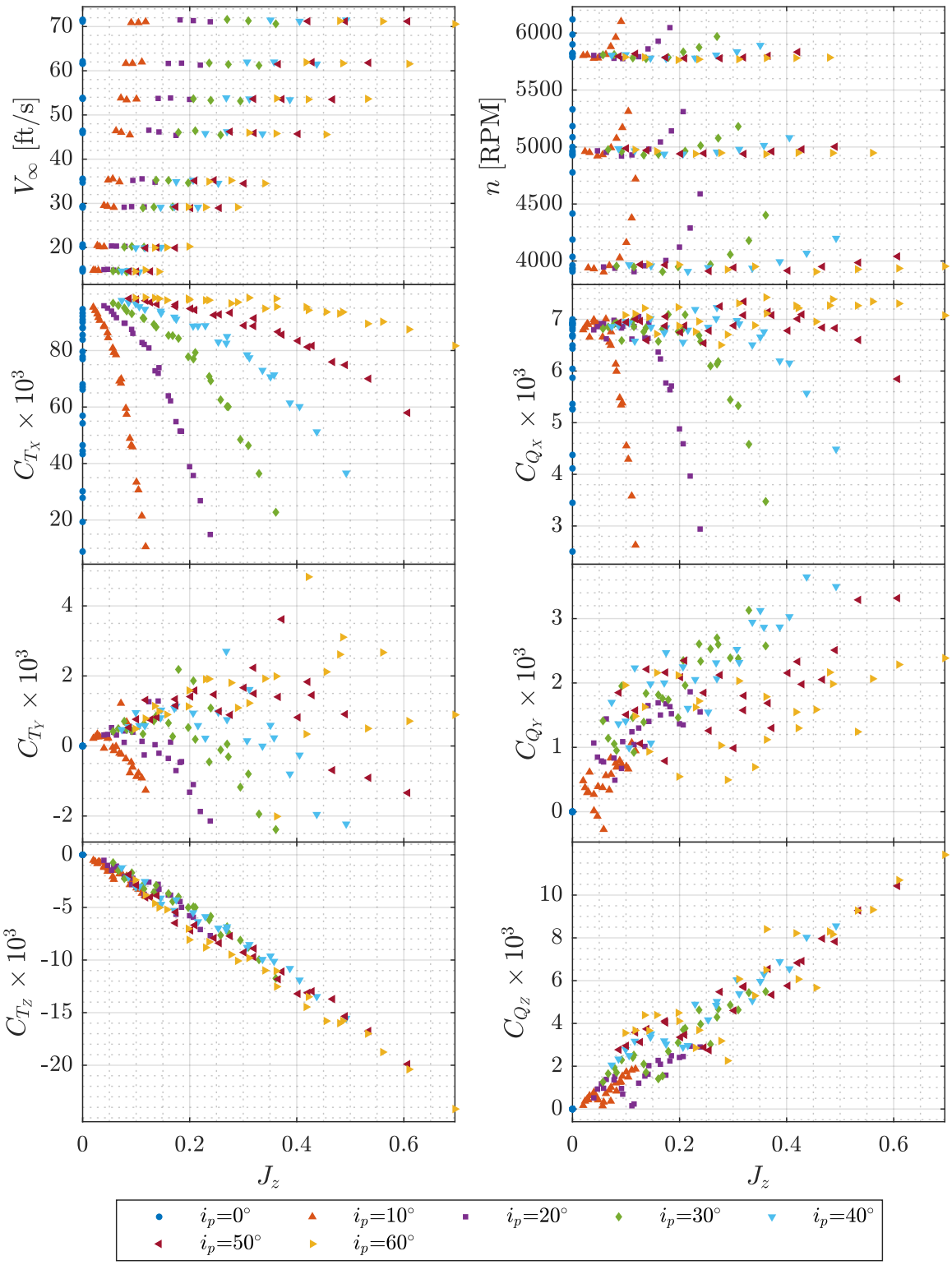

Figure 56. CCW propeller force and moment coefficients variation with J_z for $0^\circ \leq i_p \leq 60^\circ$.

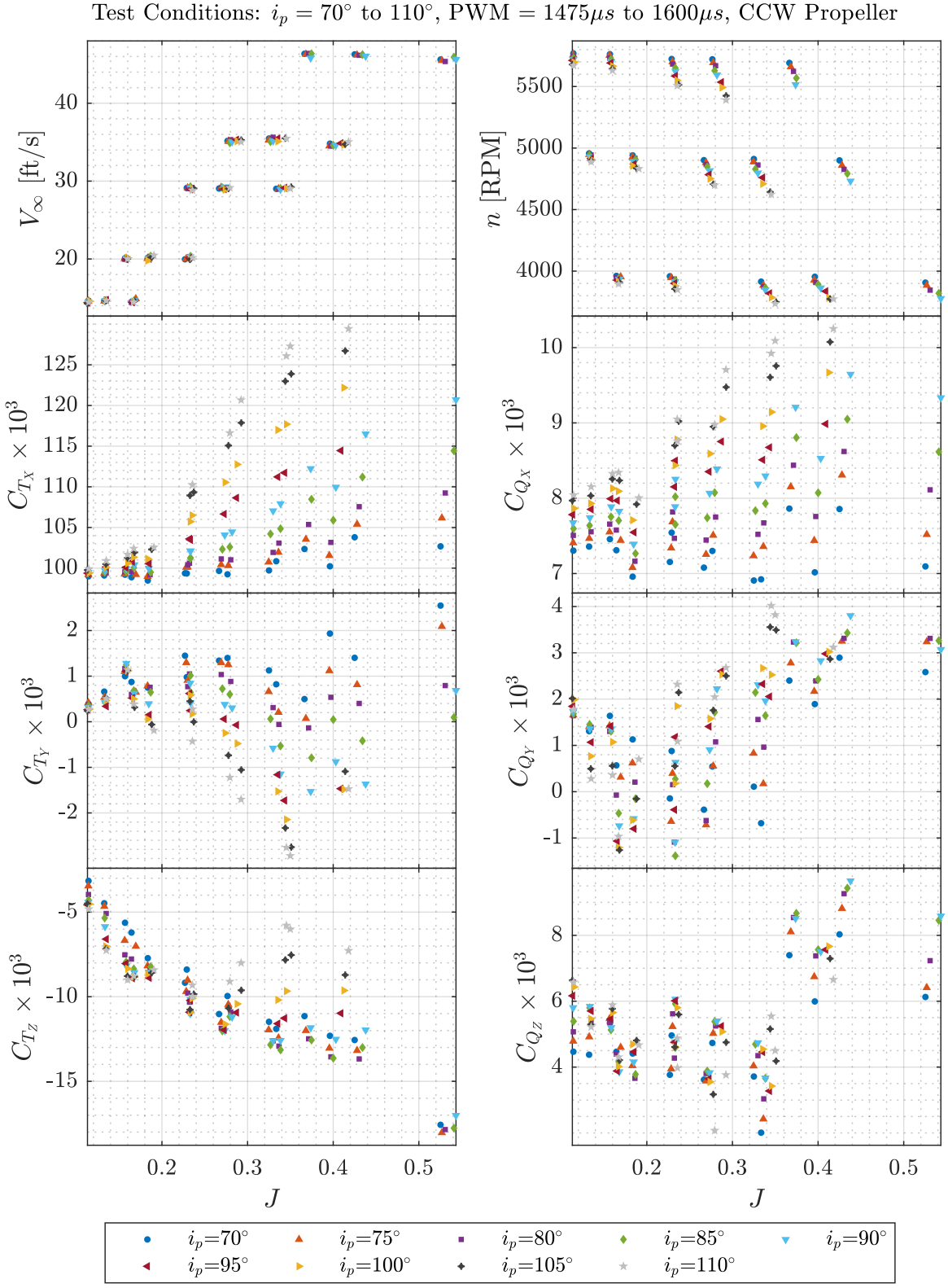

Figure 57. CCW propeller force and moment coefficients variation with J for $70^\circ \leq i_p \leq 110^\circ$.

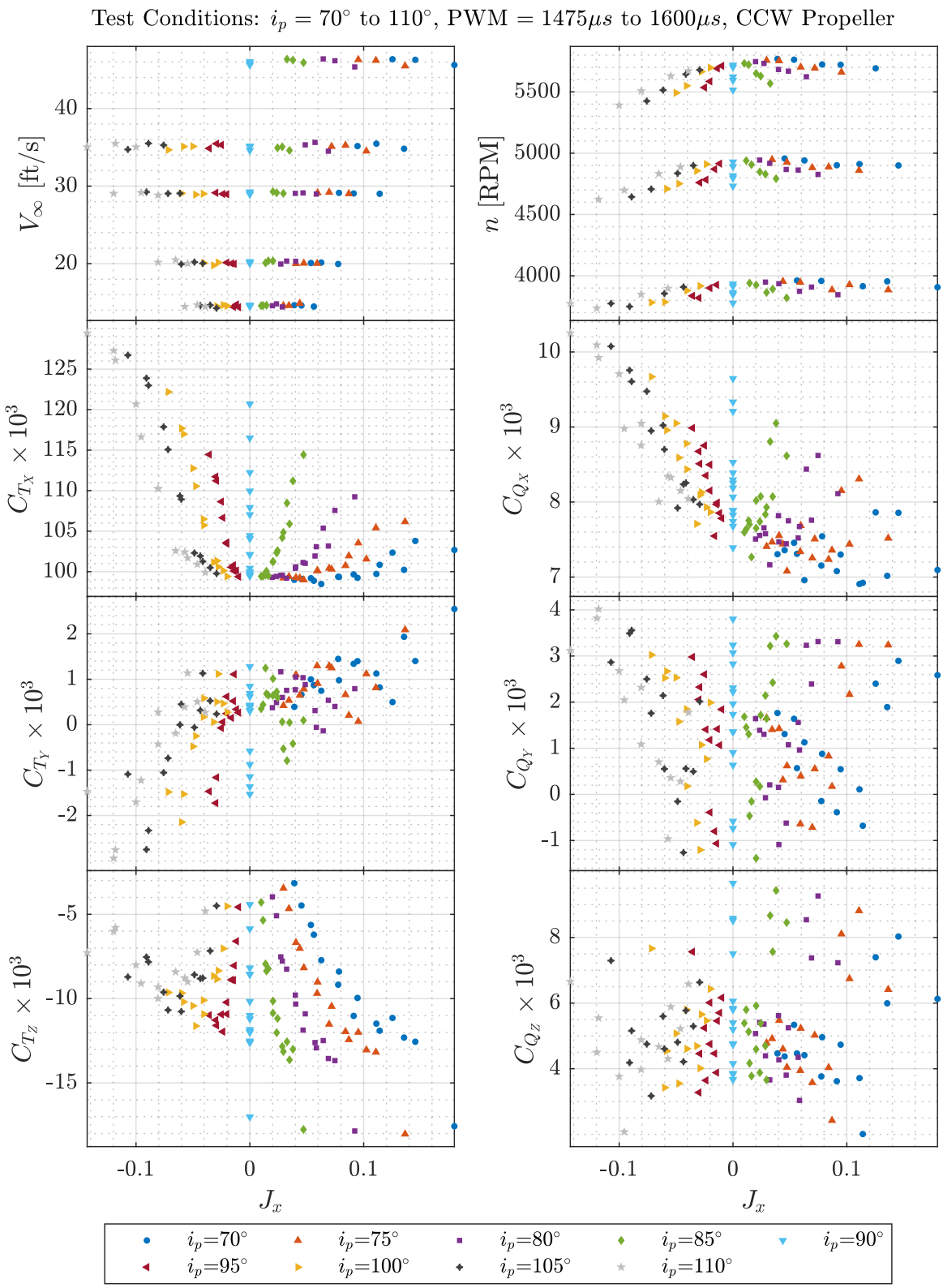

Figure 58. CCW propeller force and moment coefficients variation with J_x for $70^\circ \leq i_p \leq 110^\circ$.

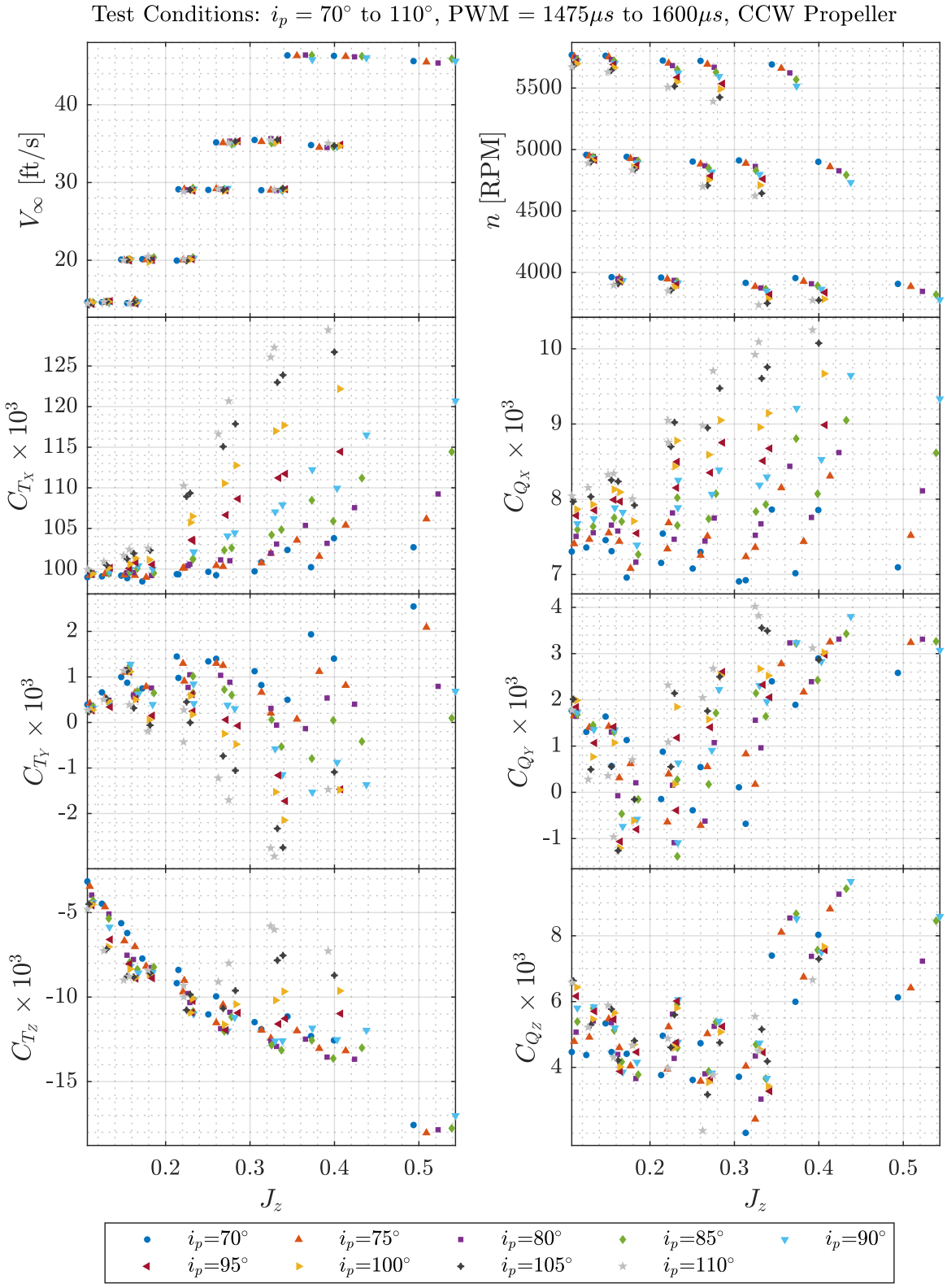

Figure 59. CCW propeller force and moment coefficients variation with J_z for $70^\circ \leq i_p \leq 110^\circ$.

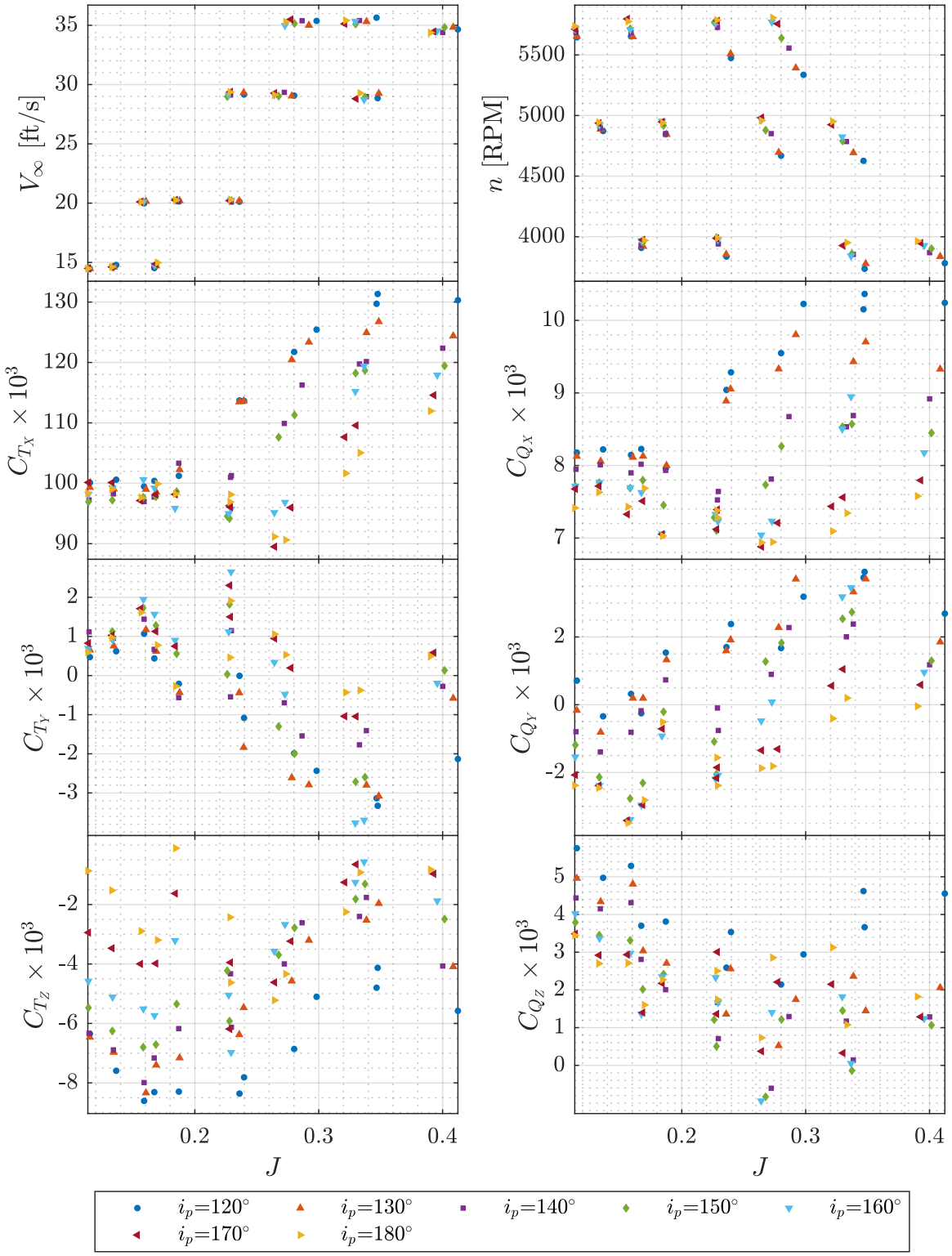

Figure 60. CCW propeller force and moment coefficients variation with J for $120^\circ \leq i_p \leq 180^\circ$.

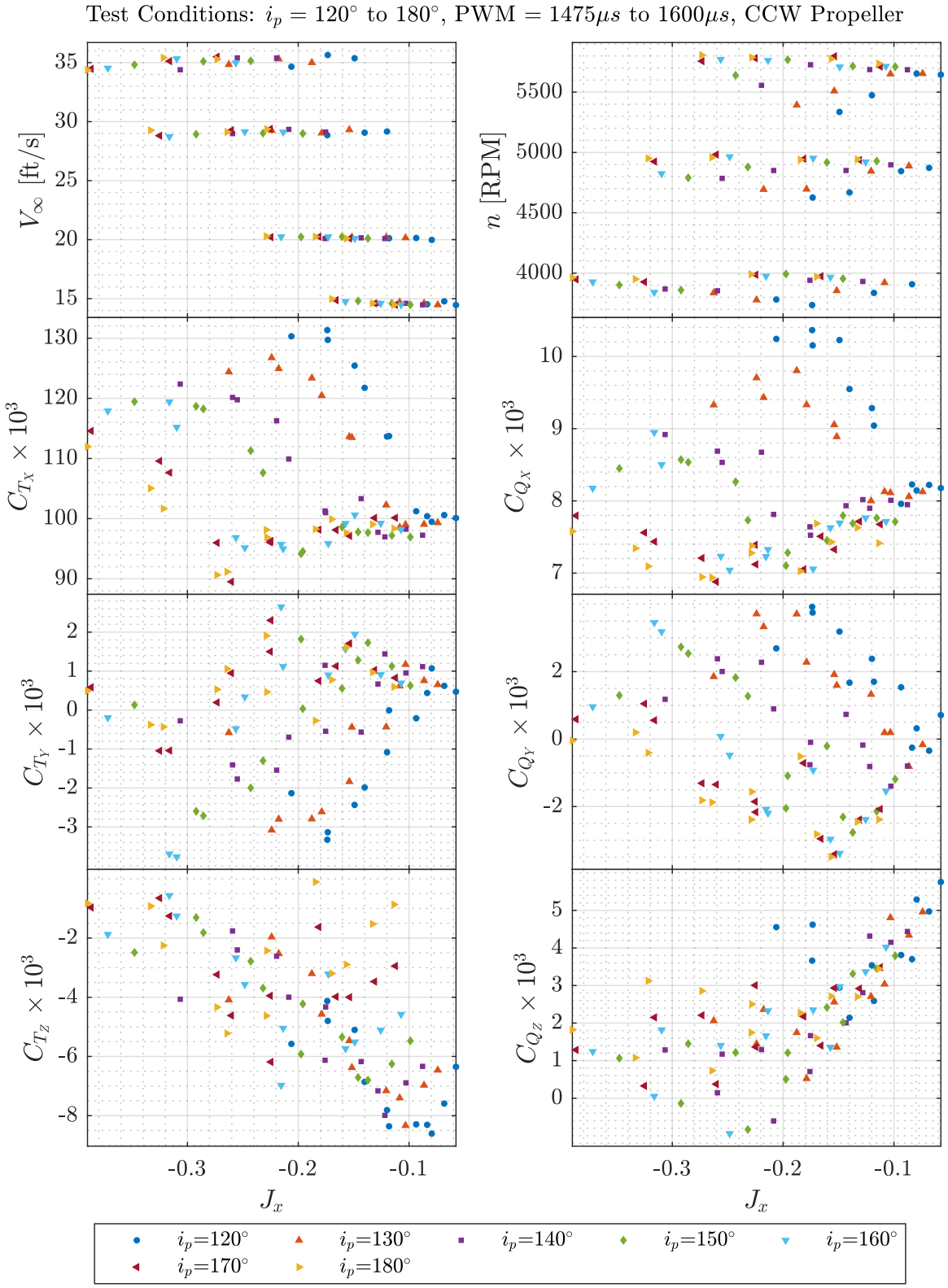

Figure 61. CCW propeller force and moment coefficients variation with J_x for $120^\circ \leq i_p \leq 180^\circ$.

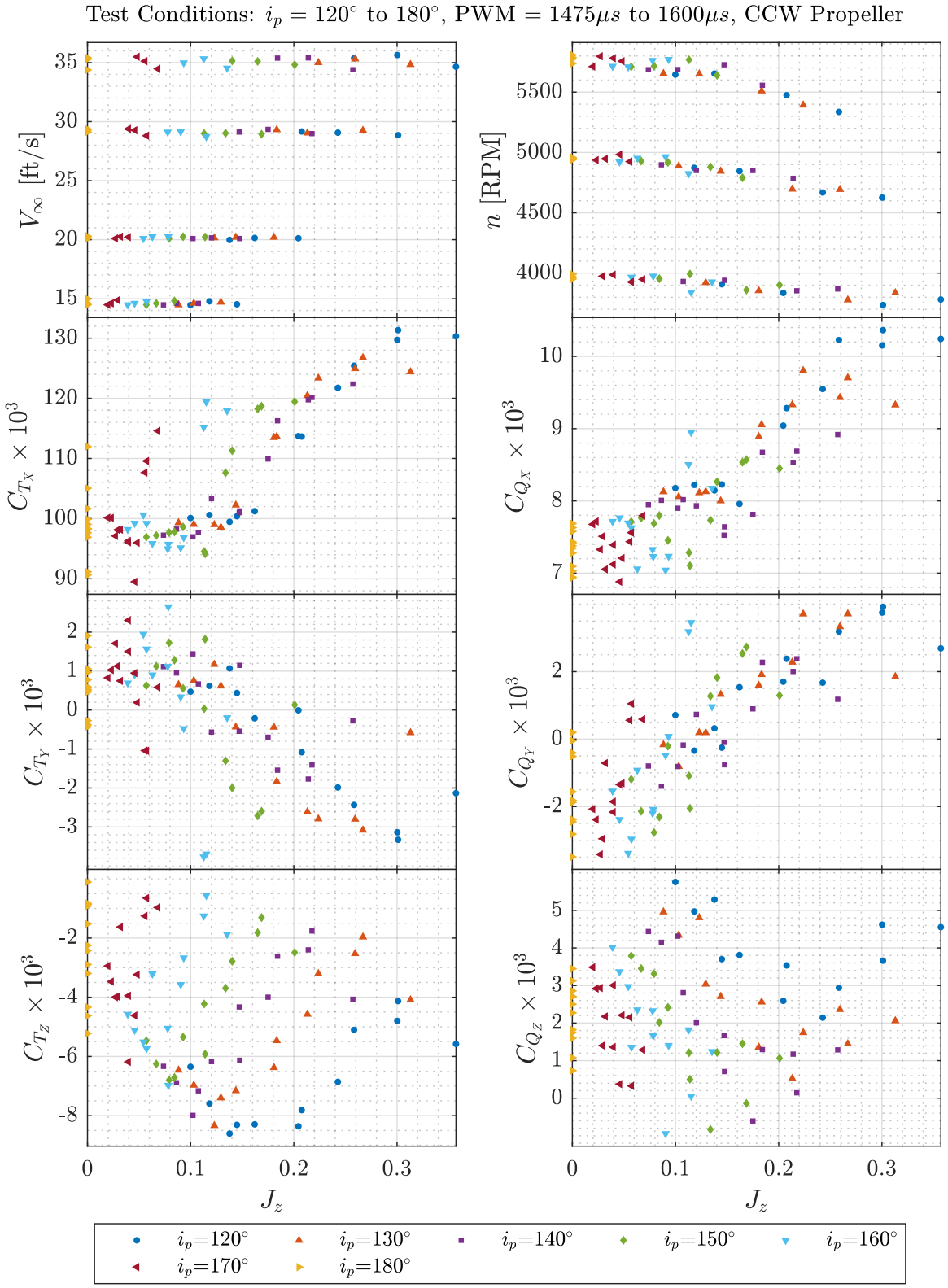

Figure 62. CCW propeller force and moment coefficients variation with J_z for $120^\circ \leq i_p \leq 180^\circ$.

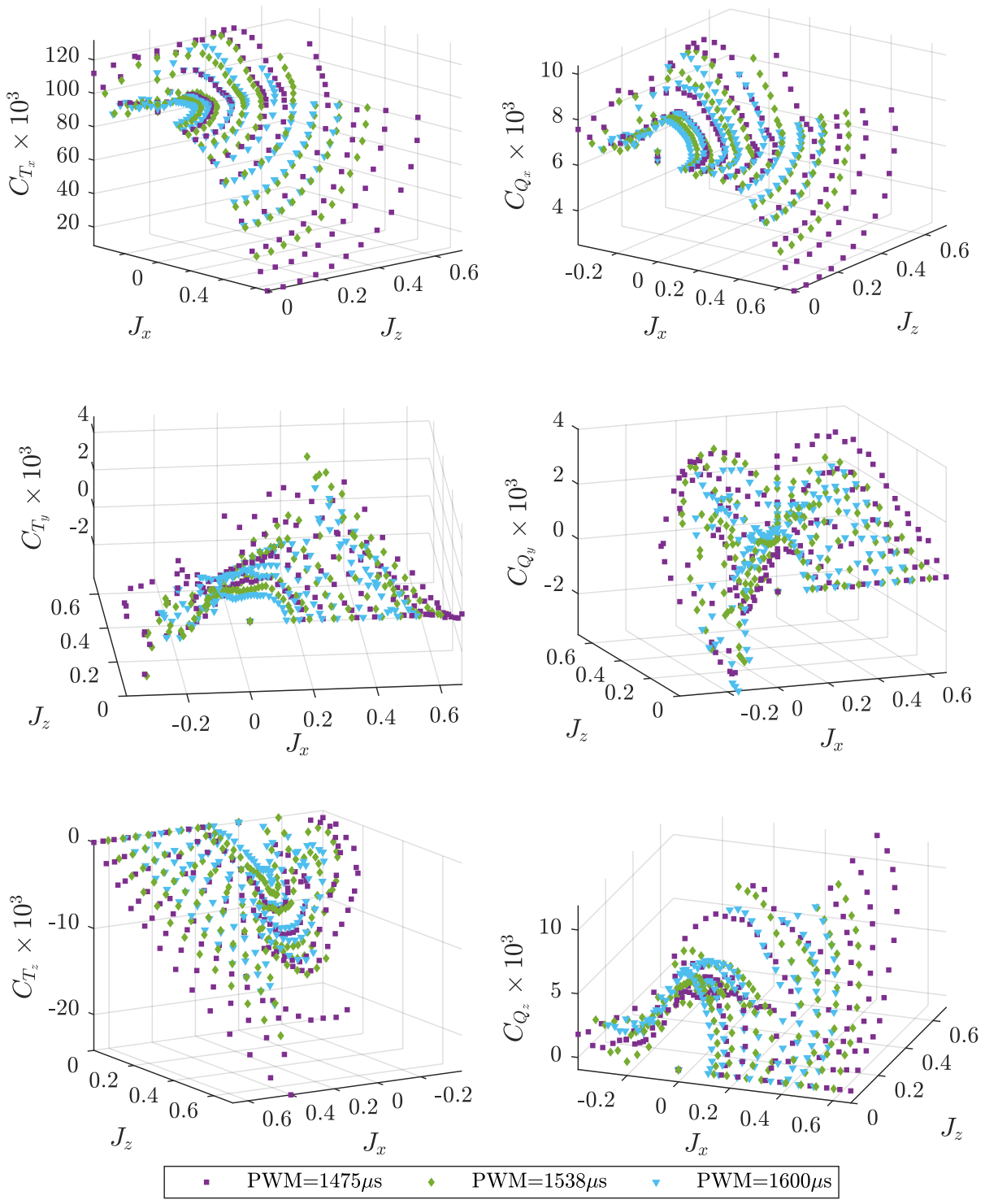

Figure 63. CCW propeller force and moment coefficients variation with J_x and J_z.

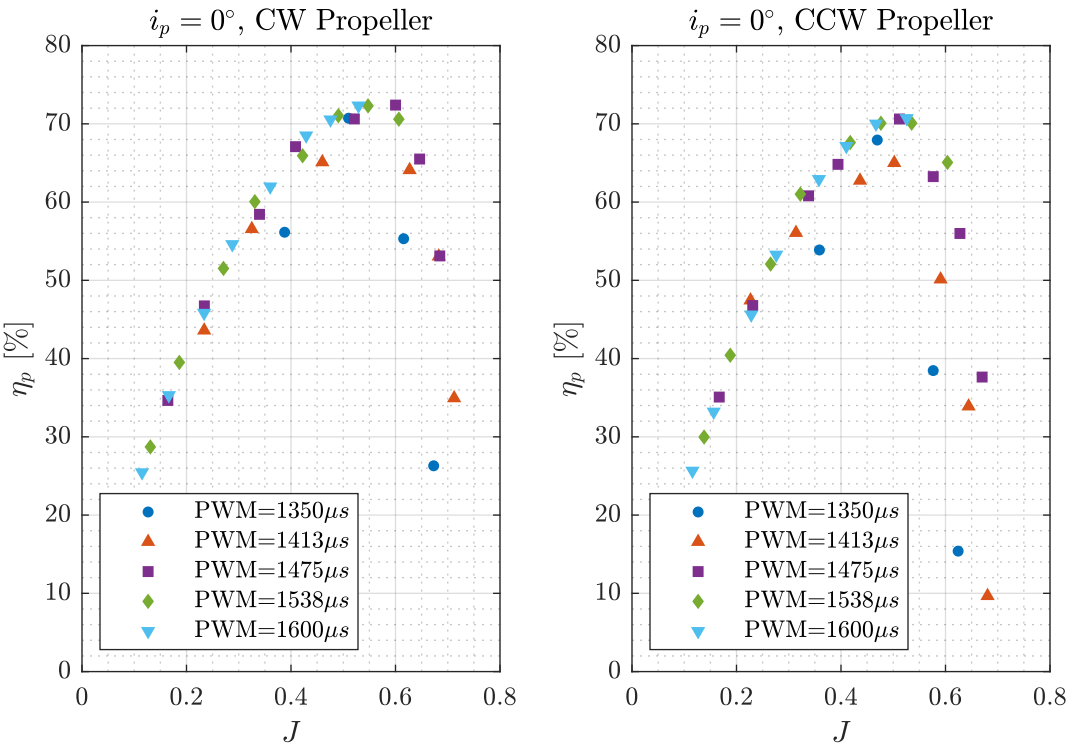

Figure 64. CW and CCW propeller propulsive efficiency η_p variation with advance ratio J at $i_p = 0°$ separated by motor PWM command.

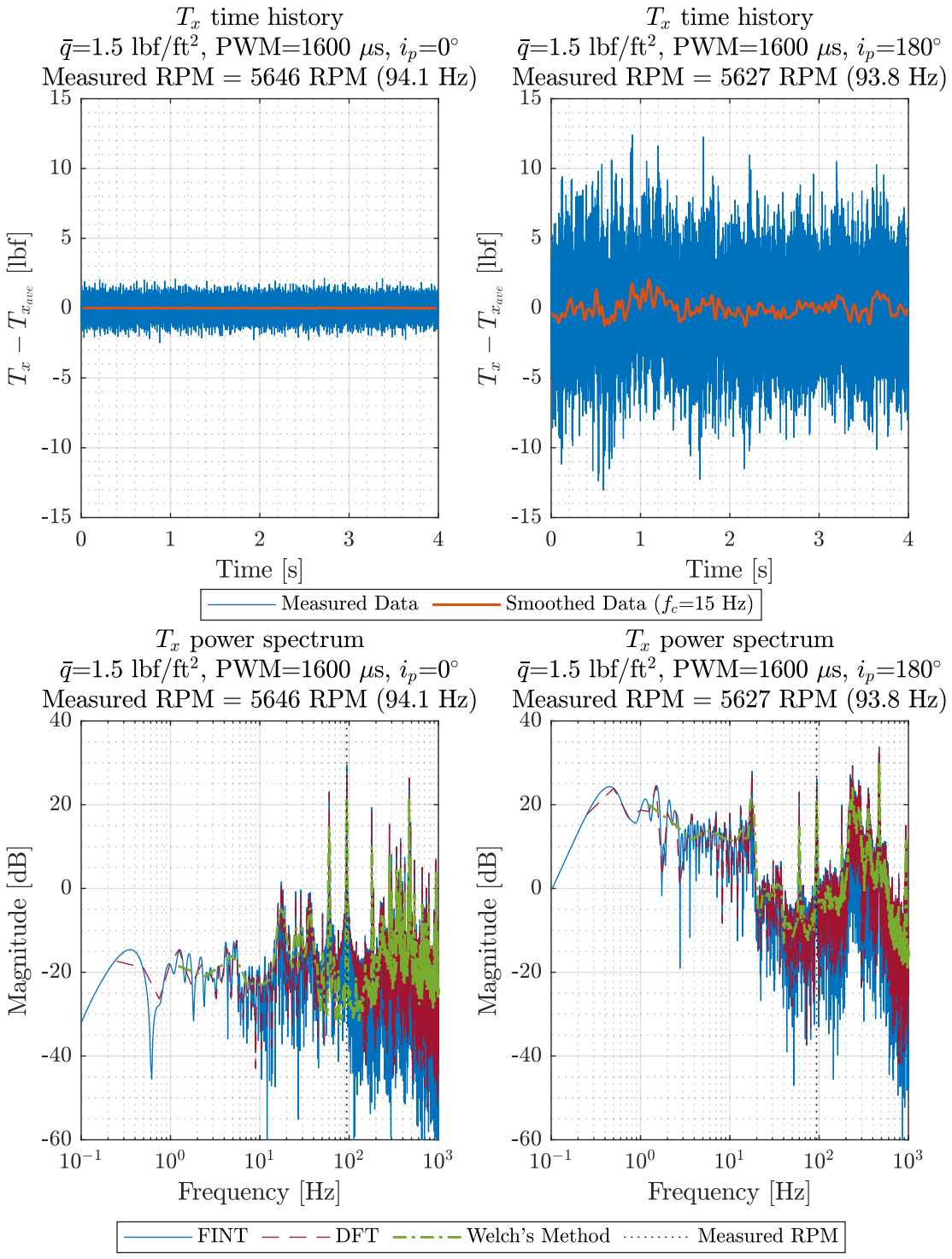

Figure 65. Time history and power spectrum of individual data point measurement histories for the CW propeller in forward flight (leftward plots at $i_p = 0°$) and VRS-like conditions (rightward plots at $i_p = 180°$).

REPORT DOCUMENTATION PAGE	Form Approved OMB No. 0704–0188

1. REPORT DATE *(DD-MM-YYYY)*	2. REPORT TYPE	3. DATES COVERED *(From - To)*
01-05-2021	Technical Memorandum	

4. TITLE AND SUBTITLE
Investigation of High Incidence Angle Propeller Aerodynamics for Subscale eVTOL Aircraft

5a. CONTRACT NUMBER

5b. GRANT NUMBER

5c. PROGRAM ELEMENT NUMBER

6. AUTHOR(S)
Benjamin M. Simmons and David B. Hatke
Langley Research Center, Hampton, Virginia

5d. PROJECT NUMBER

5e. TASK NUMBER

5f. WORK UNIT NUMBER
109492.02.07.07.05

7. PERFORMING ORGANIZATION NAME(S) AND ADDRESS(ES)
NASA Langley Research Center
Hampton, Virginia 23681-2199

8. PERFORMING ORGANIZATION REPORT NUMBER

9. SPONSORING/MONITORING AGENCY NAME(S) AND ADDRESS(ES)
National Aeronautics and Space Administration
Washington, DC 20546-0001

10. SPONSOR/MONITOR'S ACRONYM(S)
NASA

11. SPONSOR/MONITOR'S REPORT NUMBER(S)
NASA/TM–20210014010

12. DISTRIBUTION/AVAILABILITY STATEMENT
Unclassified-Unlimited
Subject Category
Availability: NASA STI Program (757) 864-9658

13. SUPPLEMENTARY NOTES

14. ABSTRACT
Propellers used for electric vertical takeoff and landing (eVTOL) aircraft propulsion systems experience a wide range of aerodynamic conditions, including significant incidence angles relative to oncoming airflow. Propellers in oblique flow exhibit deviations in thrust and torque oriented along their axis of rotation, as well as significant off-axis forces and moments. Although important for understanding eVTOL aircraft aerodynamics, sparse experimental data exist for propellers operating at incidence. This report describes an experimental wind tunnel study of isolated propeller aerodynamics across a wide range of flight conditions expected to be experienced by the LA-8 tandem tilt-wing, eVTOL aircraft. The experimental data obtained from the study are graphically presented and a discussion of observed aerodynamic phenomena is compared to theoretical expectations and past experimental work. The content of this report is intended to provide guidance to future propeller testing efforts and describe pertinent propeller aerodynamic behavior expected to be experienced by eVTOL vehicles.

15. SUBJECT TERMS
propeller aerodynamics, wind tunnel testing, Urban Air Mobility (UAM), vertical takeoff and landing (VTOL), electric propulsion, Langley Aerodrome No. 8 (LA-8)

16. SECURITY CLASSIFICATION OF:			17. LIMITATION OF ABSTRACT	18. NUMBER OF PAGES	19a. NAME OF RESPONSIBLE PERSON
a. REPORT	b. ABSTRACT	c. THIS PAGE			HQ-STI-infodesk@mail.nasa.gov
U	U	U	UU	87	19b. TELEPHONE NUMBER *(Include area code)* (757) 864-9658